Determination of the Number of Light Neutrino Generations

Nicholas Wood

University College London

Submitted to the University of London

for the Degree of

Doctor of Philosophy

1990

ProQuest Number: 10631449

All rights reserved

INFORMATION TO ALL USERS
The quality of this reproduction is dependent upon the quality of the copy submitted.

In the unlikely event that the author did not send a complete manuscript
and there are missing pages, these will be noted. Also, if material had to be removed,
a note will indicate the deletion.

ProQuest 10631449

Published by ProQuest LLC (2017). Copyright of the Dissertation is held by the Author.

All rights reserved.
This work is protected against unauthorized copying under Title 17, United States Code
Microform Edition © ProQuest LLC.

ProQuest LLC.
789 East Eisenhower Parkway
P.O. Box 1346
Ann Arbor, MI 48106 – 1346

Abstract

In 1989, the OPAL detector recorded 1.4 pb^{-1} of data from electron positron collisions in the centre of mass energy range 88< $\sqrt{s}$ <96 GeV, allowing precision measurements of the Z° resonance for first time. This thesis describes the extraction of the number of neutrino generations from this data.

Hadronic decays of the Z° are identified by large energy deposition spread over many clusters in the electromagnetic calorimeters. Tracking information is used to aid rejection of $\tau^+\tau^-$, two photon, cosmic ray, and beam related backgrounds. Hadronic events are selected with a systematic error of 0.8%. The machine luminosity is measured with the forward detectors, using small angle Bhabha scattering as the normalization process. The components of the forward detector used in this analysis are a lead-scintillator sampling elecromagnetic calorimeter and an array of proportional tube chambers. The tube chambers were used to accurately measure the position of electromagnetic showers, by doing so identifying Bhabha events in a well defined fiducial region, and measuring the absolute luminosity to an accuracy of 2.2%. The calorimeter, having a higher statistical precision, was used to determine a luminosity for each energy point with a systematic point to point error of less than 1.0%.

By combining the hadronic events selected with the luminosity measurement, hadronic cross sections were determined at each energy. The hadronic cross sections were fitted in two ways to the Z° lineshape, the difference between the two methods being the parameters left free in the fit. With a model independent fit, the values of the mass, M_z, width, Γ_z, and peak cross section σ_{had}^{pole} were found to be:-

$$M_z = 91.145 \pm 0.022 \text{ (exp)} \pm 0.030 \text{ (LEP) GeV}$$
$$\Gamma_z = 2.526 \pm 0.047 \text{ GeV}$$
$$\sigma_{had}^{pole} = 41.2 \pm 1.1 \text{ nb}$$

and from the width, the number of light neutrinos N_ν was found to be

$$N_\nu = 3.26 \pm 0.28 \text{ (exp.)}^{-0.28}_{+0.13} \text{ (theor.)}.$$

A fit to the standard model with the number of neutrino generations as a free parameter gave:-

$$N_\nu = 3.09 \pm 0.19(\text{exp})^{+0.06}_{-0.12}(\text{theor.}).$$

From the second measurement, a fourth generation of standard model light neutrinos is excluded with greater than 99% confidence.

Acknowledgements

The list of people "without whom..." would read like, well, a high energy physics paper I suppose, and only a few can be listed here. So, in no particular order thanks are (over?)due to:

My parents, sister and other members of the family for getting me this far in life, and encouraging me through the last three years...

My supervisor, David Miller, for much helpful advice and encouragement, and other members of the UCL/Brunel/Birbeck OPAL group, namely Chris (the flower child), Peter, Peter and Peter, Bruce, Jim, Mark, Brian, Andy, Domonic, Derek and Derek, Marco and Liz, whose tragic death shocked us all. Beyond the confines of UCL, I owe much to my colleagues from Maryland, Dick, Al, and Suenhou, and to the OPAL collaboration as a whole.

My friends in London: especially; Dave for friendship in and out of work, not to mention increasing my drinking capicity by at least a factor of two, Ange and Karenza for making a happy home in Clapham and not believing in neutrinos anyway (thus putting life in some kind of perspective), the Goldsmid crew, plus Martina for popping up when least expected, and Robin and Hilary and Lisa, for providing retreats from the capitals' hussle and bussle.

And on the other side of the channel, those who have made Geneva life more than an oppurtunity to work 24 hours a day; Tim, Colin and mad Bill for dragging me up mountains and down ski slopes I might otherwise have avoided, the Alps, for being there to do these things on, and "the lads" for drunken evenings when such things were required. And last but not at all least, Sara - I know she won't want a special mention, but she's getting one anyway.

I also thank the SERC for providing the necessary cash, even it wasn't always in the right place at the right time.

Contents

List of Figures

List of Tables

Chapter 1

Introduction

One of the finest scientific achievements of the twentieth century is the establishment of the Standard Model of matter and it's interactions. The Standard Model contains numerically predictive theories whose accuracy is unrivalled throughout the whole sphere of physics; in particular the description of the electromagnetic interactions of particles has been experimentally tested and found to give agreement to more than ten significant figures. However at the centre of this theory is a mystery; there are approximately twenty six parameters that have to be put into the model "by hand". There is no description of why these parameters should take the values that they do. Since the establishment of the Standard Model, the goal of experimental particle physicists has been to test it as rigorously as possible, searching for deviations between the theory and experiment, in the hope that something might emerge that will illuminate this darker side and hint at a more fundamental theory beyond. In the last ten years, although vast progress has occurred in the range and complexity of calculations and experimental tests, little has emerged to change this situation. Thus in order to search in a previously inaccessible range of energies, new experimental facilities have been built, in particular the LEP (Large Electron Positron) Ring at CERN (The European Particle Physics Laboratory), Geneva, and SLC (Stanford Linear Collider) at Stanford, California. In addition HERA (Hadron Electron Ring Accelerator), at DESY, Hamburg, will come into operation later this year. There are also machines of even higher energies being planned to come into operation

in the late nineties; the SSC (Superconducting Super-Collider) in Texas, and the proposed LHC (Large Hadron Collider) at CERN. Since each of these facilities and the experiments using them require hundreds of physicists to design and build them, in the process breaking new ground in many areas of technology, it is not inappropriate to describe this search for cracks in the standard model as an epic global struggle.

There are many text books giving thorough accounts of the Standard Model [1] so there is no attempt to give a detailed description here. In outline, there are three forces described by the model; the electromagnetic force, the weak nuclear force, and the strong nuclear force. Each force has its own mediating particle or particles, and these types of particle are known as gauge bosons (summarised in table 1.1). There is also a theory that "unifies" the weak and electromagnetic force, the most favoured mechanism for doing this being through an as yet undiscovered particle, the scalar Higgs boson. Attempts to unify the electroweak theory with the theory of the strong interaction, quantum chromodynamics (QCD), have so far been unsuccessful, despite striking similarities in the structure of the theories. In addition to the bosons associated with interactions, the model includes "families" of particles which make up matter. Each family contains two types of quark (particles which interact through the strong force and make up protons and neutrons), and two types of lepton (particles which do not interact through the strong force) - an electron-type particle and an associated neutrino. The quarks and leptons are collectively known as fermions (table 1.2). The theory does not predict the number of such fermion families; this is one of the free parameters. Three families have been discovered so far (although not all members of the heaviest family have been observed), and there are various experimental constraints limiting the number of families to about five (these will be discussed in detail in section 2.1).

Electromagnetic interactions have been thoroughly studied and no significant disagreement has been observed between theory and experiment. Strong interactions have been experimentally investigated and have been found to be in broad agreement with theory though technical difficulties in calculating QCD

Table 1.1: Gauge Bosons

Boson	Mass (GeV/c^2)	Type of Interaction	Relative Strength of Interaction
gluon	0	strong interaction	1
γ (photon)	0	electromagnetic	10^{-2}
$Z^0, W^{\pm}$	92, 81	weak interaction	10^{-5}

Table 1.2: Fermions

Quarks			charge
u (up)	c (charm)	t (top)	+2/3
d (down)	s (strange)	b (bottom)	-1/3
Leptons			
e (electron)	μ (muon)	τ (tau)	-1
ν_e (e-neutrino)	ν_μ (μ-neutrino)	ν_τ (τ-neutrino)	0

processes mean that precise comparisons are not yet possible. Thus the prime motivation behind the construction of LEP (and SLC) was to investigate the weak force and the electromagnetic and weak (electro-weak) unification. The weak force is mediated by three massive particles, the W+,W-, and Z°. Direct and clean production of the Z° has been possible for the first time with LEP and SLC (previous machines having been too low in energy or producing the Z° only in conditions of high background), and this allows new precision tests of the electroweak theory.

This thesis describes one of the first important results from LEP, the measurement of the Z° boson lineshape, and the extraction from the lineshape of the coupling of the Z° to decay products not observed directly in the OPAL detector. If one assumes that the only unseen particles are light neutrinos this coupling can be interpreted as a measurement of the number of families of light neutrino. A light neutrino in this context is one with mass less than half the Z° mass and which can therefore be directly produced at LEP. The assumption that neutrinos are light is based on experimental evidence placing upper limits on the electron neutrino mass of a few eV, the other two known neutrinos having somewhat higher upper limits on their mass. All experimental evidence is consistent with massless neutrinos. A further assumption that there exist only complete families of two quarks, a charged lepton, and a light neutrino, allows one to infer from this measurement the number of fermions types present in nature.

The lineshape can be calculated assuming differing numbers of neutrinos, so the extraction of the number of neutrino generations from the data is carried out by a fit with the number of neutrinos as a free parameter. A precise lineshape calculation is essential for the analysis, encompassing a knowledge of couplings of the Z° to all its decay products. However, as an integer result is expected for the number of neutrino families, any significant departure from an integer will indicate either unexpected new decays, or some basic disagreement with standard model assumptions. In addition to acting as a probe of the number of basic constituents of matter, the measurement therefore forms an important test of the standard model. Furthermore, it is relevant to models of the evolution

of the early universe, and so has significance beyond the boundaries of particle physics.

As any experiment in modern particle physics is a large collaborative effort, it is inevitable that the concept of a thesis being an individual's work is somewhat diluted. The first part of this thesis is a description of the theoretical background to the measurement. The OPAL detector is then described, with emphasis on the part the author was personally responsible for, the tube chambers of the forward detector. The method developed by the author for measuring the luminosity of collisions at OPAL using these tube chambers (in conjunction with the forward calorimeter) is then presented. Finally the multi-hadron selection analysis and fit to the Z° lineshape is described, yielding the mass and width of the Z° and the number of neutrino generations. The author was not directly involved with the multi-hadron selection, but this is presented for completeness. Some of the more technical aspects of the tube chambers together with other work not directly relevant to the main theme of the thesis are presented as appendices.

Chapter 2

Theoretical Background to the Determination of the Number of Neutrino Generations

Three generations of fermions have been discovered so far, but there is no theoretical reason within the Standard Model why there could not be a large number of fermion generations as yet unobserved. The heaviest quark of the three generations remains outside the reach of todays accelerators, and the tau neutrino has only been indirectly seen. Upper limits on the number of light neutrino generations have been experimentally determined both at colliders and from measurements of the ^{4}He abundance in the universe (which will be described in section 2.1), but before the advent of the LEP and SLC e+ e- colliders, a precise determination of the number of neutrinos had not been possible. The study of the Z° resonance at LEP allows the number of light neutrinos to be extracted in two distinct ways; through a study of the Z° lineshape (section 2.2) using one or more of the decay channels of the Z° and through the direct measurement of the cross section for single photon production from the reaction $e^+e^- \rightarrow \nu\bar{\nu}\gamma$(section 2.3), the photon acting as a tag on the production of an otherwise unobservable final state. The former of these methods has the advantage that it can be carried out during a scan of the Z° and requires less integrated luminosity, but relies quite heavily on a detailed understanding of the standard model. The latter

is more model-independent, but requires running LEP at energies above the Z° resonance, which is of limited interest for other physics topics, and in addition requires greater integrated luminosity for a measurement of equal precision. The most significant systematic errors on the two measurements are from different sources, so the two methods are complementary. In particular the lineshape method is heavily dependant on a precise knowledge of the absolute luminosity (section 2.4), whereas the cross section method is limited by the understanding of the relative contributions of signal and background processes.

2.1 Limits on the Number of Neutrinos Prior to LEP

2.1.1 Limits on the Number of Neutrino Generations from Astrophysics

One of the interesting features of the problem of determining the number of neutrino generations is that the limits have arisen from such diverse sources. The first limits of any sort were derived from measurements of the ^{4}He abundance in the universe, and relating this to the number of neutrino types through models of the evolution of the early universe (early, in this context, meaning the first 100 seconds). A thorough account of the implications such models have for a whole range of issues in particle physics is given by Dolgov and Zeldovich [2]. In outline, the argument leading to a limit on the number of neutrinos proceeds as follows. In the very early moments of the universe (t$<$ 1 second) the enormous temperatures lead to quarks, leptons and bosons being in a statistical equilibrium. The universe is at this stage in a state of "free expansion" where the energy density ρ is related to the expansion timescale t by

$$\rho \propto t^{-2}.$$

'Extra' particles increase the energy density and hence decrease the expansion timescale. As the universe cools with time, the quarks and gluons condense into nucleons. After this condensation, nucleons and leptons are in a statistical

equilibrium through the weak interactions

$$\begin{aligned} n + e^+ &\rightleftharpoons p + \overline{\nu_e} \\ p + e^- &\rightleftharpoons n + \nu_e \\ n &\rightleftharpoons p + e^- + \nu_e \\ p &\rightleftharpoons n + e^+ + \overline{\nu_e}. \end{aligned}$$

The ratio of neutrons to protons is given by

$$\frac{N_n}{N_p} = e^{\frac{-\Delta m c^2}{kT}} \tag{2.1}$$

where N_p, N_n are the proton and neutron concentrations, Δm is the mass difference between the two nucleons, and T is the temperature. This equilibrium is broken when the characteristic time of the above reactions is comparable with the expansion timescale of the universe (when T $\sim 10^{10}$K) which "freezes out" the neutron-proton ratio to the value at that time. Note that, unlike in conventional thermodynamics, the conditions of the rapidly expanding universe lead to equilibrium being achieved on short timescales, but as the universe gets older (and less dense) it moves away from equilibrium. At a later stage, nearly all neutrons become bound into ^{4}He (the neutron lifetime being long compared with the expansion timescale at this point), so the ^{4}He mass fraction M_{frac} (the mass ratio of ^{4}He to other matter) is given by

$$M_{frac} = 2(N_n/N_p)/[1 + (N_n/N_p)].$$

A measurement of M_{frac} yields the neutron-proton ratio, from which the freeze out temperature can be calculated using equation 2.1. Extra neutrino families increase the expansion rate of the universe and thus affect the temperature at which freeze out occurs. Calculations by Schramm and Wagoner [3] predict the value of the ^{4}He mass fraction to be be in the range 0.23-0.26, the uncertainty arising from the dependance of the mass fraction on the baryon density. Note however that the baryon density only affects the formation of ^{4}He from nucleons rather than the ratio N_n/N_p, and so only weakly affects the result.

Measurements of the mass fraction fall into the range $0.2 < M_{frac} < 0.3$. The determination of a limit on number of neutrino generations from these measurements has been the subject of some debate, with both the interpretation of the

experimental data and application of the model under dispute. As a result, it is not possible to quote a universally accepted result, but values in the literature [4] lie in the range

$$N_\nu \leq 3.0 - 5.5.$$

A second source of astrophysical limits on neutrino generations has arisen from the observation of neutrino events in underground detectors (originally designed for measurements of the proton decay lifetime). The detectors IMB III [5] and Kamiokande II [6] both observed an increased neutrino flux correlated with the supernova SN1987a, and from these data Ellis and Olive [7] derived a limit of

$$N_\nu \leq 6.7$$

using a model of supernova collapse.

2.1.2 Limits on the number of neutrino generations from e^+e^- colliders

Experiments at the PEP (SLAC, California) and PETRA (DESY, Hamburg) e^+e^- colliders, operating in the $\sim$ 30-40 GeV energy range, have placed limits on the number of neutrino generations through studying the process $e^+e^- \rightarrow \nu\bar{\nu}\gamma$ (shown schematically in fig 2.1), where the production of weakly interacting neutral particles is tagged by a photon radiated from one of the initial state particles. This method is in principle the same as that for the measurement of the single photon cross section at LEP and will be described in greater detail in section 2.3. For determining the number of neutrino types, these experiments suffered a severe disadvantage with respect the possibilities at LEP experiments by operating at centre of mass energies well below the Z° pole. As a result the cross sections were tiny; the CELLO collaboration [8] reported a limit of $N_\nu < 15$ based on a non-observation of events passing suitable cuts to remove background. The ASP experiment [9],[10] achieved a stronger limit of $N_\nu < 7.5$, essentially by accumulating a greater integrated luminosity, and observing a few events. If a global average is taken of all such experiments, however, then a relatively strong

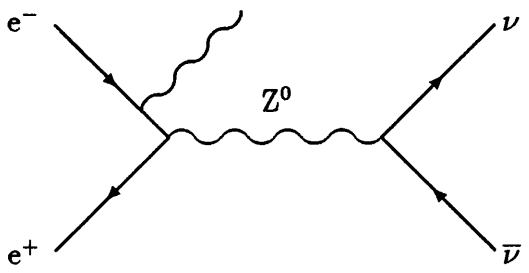

Figure 2.1: Feymann diagram of the single photon neutrino counting process

limit of

$$N_\nu < 4.9$$

is obtained.

2.1.3 Limits on the number of neutrino generations from $p\overline{p}$ colliders

The UA1 and UA2 experiments at CERN, and the CDF experiment at Fermilab, have reported limits on the number of light neutrinos. There are three ways in which this can be done. Firstly, by reconstructing the invariant mass of lepton pairs produced by $q\bar{q} \rightarrow l\bar{l}$ the Z° width can be directly measured. However this is performed far more cleanly and with greater accuracy at LEP and this method will be described in section 2.2. The second method is analogous to the single photon method; a single gluon is radiated from an initial state quark (fig 2.2) in the process $q\bar{q} \rightarrow Z^\circ g \rightarrow \nu\bar{\nu}g$. The signal is therefore a monojet as opposed to a single photon. The precision of this method is limited by the understanding of background sources of monojets, and limit of $N_\nu < 10$ is reported by UA1 [11] using this method.

The third and strongest limit on the number neutrino species comes from a measurement of the ratio R of the measured leptonic decay rate of the $W^\pm$ and

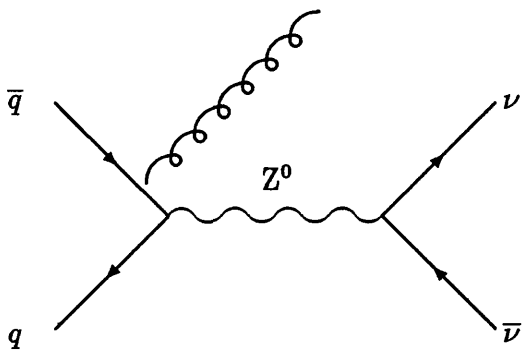

Figure 2.2: Feymann diagram of the single gluon production neutrino counting process

Z° bosons. This is given by

$$R_{exp} = \frac{N(W \rightarrow l\nu)}{N(Z \rightarrow l^+l^-)}$$

The error in this quantity is dominated by the statistical uncertainty in the number of leptonic Z decays. The theoretical expression for the same quantity is given by

$$R_{th} = \frac{\sigma_W \Gamma_Z \, \Gamma(W \rightarrow l\nu)}{\sigma_Z \Gamma_W \, \Gamma(Z \rightarrow l^+l^-)}$$

The number of neutrino generations enters through the total width of the Z°. The calculation of the total production cross section ratio involves the use of proton structure functions to determine the relative parton luminosities appropriate for $W^{\pm}$ and Z° production, and it is this which contributes the largest error. There was, at the time of the published analyses, also an uncertainty in the total width of the W boson arising from the possibility that it could have decay into $t\bar{b}$, or a fourth generation lepton. Thus the predicted R is a function of the number of neutrinos and the top mass, and assumed no extra decay modes of the $W^{\pm}$ and Z°. UA1 made a measurement of the R ratio using electronic and muonic channels [12], and found a value $9.1^{+1.7}_{-1.2}$. UA2 made a measurement using the electronic channel only [13], and this gave $7.2^{+1.7}_{-1.2}$. If were combined then a value

of $8.4^{+1.2}_{-0.9}$ was obtained. Assuming a top quark mass of 40 GeV [1] then a limit of

$$N_\nu < 5.7$$

was obtained.

2.2 Determination of the number of neutrino generations from the Z° lineshape

An extra generation of neutrinos will contribute an additional channel for the decay of the Z° and thus increase its total width. However additional generations also affect the magnitude Z° peak cross section in any channel, and so there are a number of different analyses which can yield a number of neutrinos each with semi-independent systematic errors and model dependences. Common to all these variations, however, is the need to understand the Z° lineshape and the appropriate higher order radiative corrections.

2.2.1 The Z° lineshape

In parallel to the experimental preparation, a large effort has been put into improving the accuracy of theoretical calculations to enable true precision tests of the standard model at LEP. The calculation of radiative corrections for electroweak processes has become a field of study in its own right,and a comprehensive review of the current status of theoretical understanding of Z° physics is given in [14]. This section describes the form of the Z° lineshape in lowest order, what corrections have to be applied, and how these affect the lineshape.

The total cross section for the process

$$e^+e^- \rightarrow Z^\circ \rightarrow f\overline{f}$$

(shown diagramaticaly in fig. 2.3) as a function of centre of mass energy of the

[1] A top quark of this mass is now excluded by LEP, CERN collider and Fermilab experiments, but the 40 GeV top quark mass represented a conservative estimate at the time of the publication of the above results.

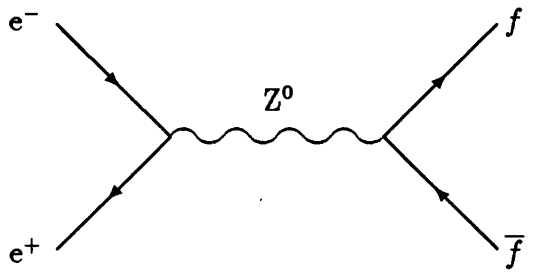

Figure 2.3: Feynman diagram of lowest order s-channel Z° process

electron positron pair is in lowest order (and neglecting the QED contribution and fermion masses) given by the Breit-Wigner formula

$$\sigma(s) = \frac{12\pi}{M_z^2} \frac{s\Gamma_e\Gamma_f}{(s - M_z)^2 + M_z^2\Gamma_z^2}$$

where s is the centre of mass energy squared, M_z is the mass of the Z° and $\Gamma_z, \Gamma_e, \Gamma_f$ are the total, electronic, and final state widths of the Z° respectively. Radiative corrections substantially modify this form, and as it stands, it is of little use for precision comparisons with experiment, but serves as a starting point. The following corrections to the simple Breit Wigner must be considered:-

- QED radiative corrections
- QED lowest order and $\gamma - Z$ interference terms
- Vertex and self-energy corrections
- QCD corrections[2]

QED Radiative Corrections

Full QED corrections include initial state and final state radiation Fig. 2.4, the contribution of interference between the two, and virtual and vertex corrections. If no

[2]only applicable for quark final states

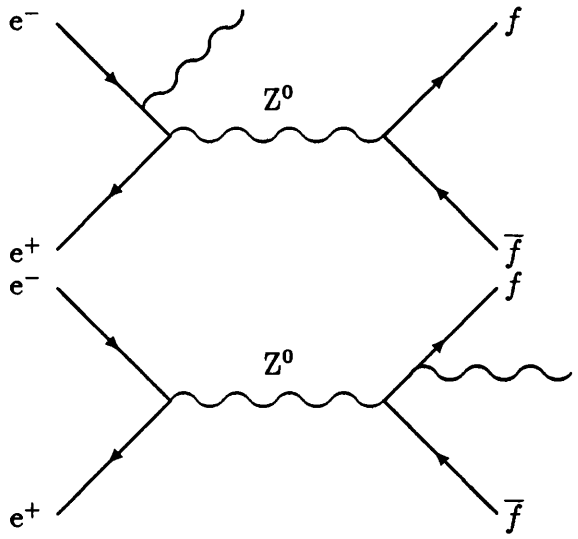

Figure 2.4: Feynman diagram of initial and final state radiative QED corrections to s-channel Z^0 process

cuts are made on the final state fermions, the final state and interference contributions are negligible. Initial state radiation, by contrast, has an extremely large effect on the lineshape. Even $O(\alpha)$ corrections are insufficient for accuracies of O(1%), and $O(\alpha^2)$ calculations are necessary to match experimental precision.

Initial state radiative corrections can be decoupled from other corrections by the structure function approach [15]. The cross section for centre of mass energy s is written

$$\sigma(s) = \int_{x_0}^{s} G(s,s')\sigma_{weak}(s')\,ds'$$

where s' is the reduced centre of mass energy, σ_{weak} is the "weak" cross section (i.e. the cross section for fermion pair production with all other corrections applied) and $G(s,s')$ is the structure function. The principle is that initial state radiation takes the centre of mass energy to a lower value than twice the beam energy, so σ_{weak} is the cross section at the lowered energy, and $G(s,s')$ (the structure function) represents the probability density of the incoming particles of centre of mass energy s, radiating to the lower energy s'. x_0 is a low energy cut off value. The effect of QED corrections can be seen in fig. 2.5. The peak cross section is reduced to approximately 3/4 of the lowest order value. Calculations

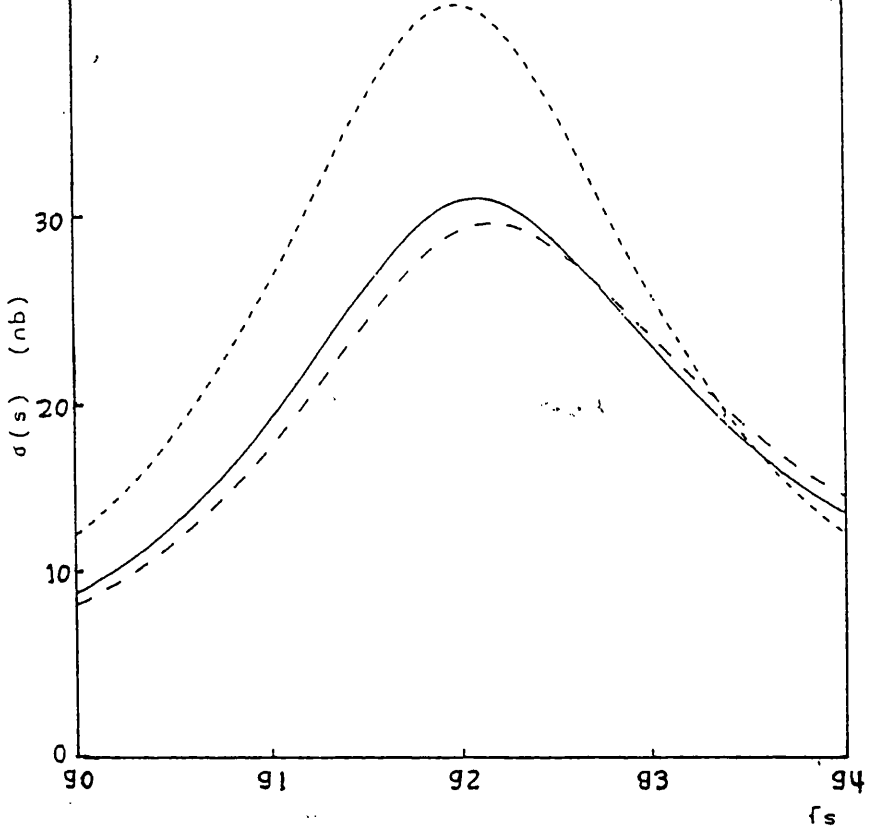

Figure 2.5: The effect of QED corrections on the lineshape for e^+e^- Z° $\rightarrow$ hadrons. Shown are the uncorrected lineshape (fine dashed line), first order QED corrections applied (dashed line), and second order exponentiated corrections applied (solid line).

exist by many authors, including those to full second order and those using exponentiation techniques, and the reader is referred to ref. [14] for a comprehensive review of the literature.

QED Lowest Order and $\gamma - Z$ Interference Terms

The relative contribution of the Z° and photon diagrams is dependant on the final state, as the relative couplings to the photon and Z° are different for different states, and in particular the electron channel must be considered separately due to the presence of the extra t-channel diagram. The qualitative effect of QED lowest order diagram is the same; as the QED cross section is almost constant over the Z° resonance, the result of the photon diagram is to create a baseline on which the Z° resonance lies. The effect of $\gamma - Z$ interference is more complicated as the sign of the correction changes across the Z° peak, but for the

hadronic channel both terms are small and can be accounted for with a lowest order calculation.

Vertex and Self-Energy Corrections

The presence of virtual fermion loops in the Z° propagator (known as self-energy terms) is already accounted for to some extent by the existence of a width Γ_z in the Breit-Wigner formula (what is considered a "correction" and what is included in the width is partially a matter of definition). The width is not independent of s however and so a better approximation is the "s-dependant" Breit-Wigner

$$\sigma(s) = \frac{12\pi}{M_z^2} \frac{s\Gamma_e\Gamma_f}{(s - M_z)^2 + s^2\Gamma_z^2/M_z^2}.$$

Similarly corrections to the vertex (other than QED corrections already encompassed in section 2.2.1) can be included by modified s-dependant couplings of the Z°. These corrections are channel dependent, and so must be calculated separately for the final state required. The full vertex and self energy corrections are dependent on the top mass, as virtual top quarks can appear in the diagrams, and thus the uncertainty in the top mass introduces an error in in the theoretical calculations.

QCD corrections

Due to the strong coupling of quantum chromodynamics, final state corrections to $q\bar{q}$ decays of the Z° are significant. They can be included in a fairly simple way however, by a multiplicative factor to the cross section $1 + \delta_{QCD}$, which has a measured value of

$$\delta_{QCD}(\sqrt{s} = 34\,GeV) = 0.047 \pm 0.009$$

which when allowing for the running coupling constant of QCD takes on a value

$$\delta_{QCD}(\sqrt{s} = 92\,GeV) = 0.04 \pm 0.007.$$

Uncertainties in the value of this correction factor and the value of α_s to use lead to an error in the theoretical results.

2.2.2 Determination of the Number of Neutrino Generations from the Z° lineshape

An extra generation of neutrinos will both increase the total width of the Z° and decrease the peak cross section. As a result, methods of determining the number of neutrinos based on based on either of these effects can be devised, though the systematic errors involved are correlated. Two slightly different approaches are presented below, although there are a large number of minor variations on these themes.

2.2.3 Determination of the Number of Neutrino Generations by a Comparison of the Total and Expected Width

The number of neutrino generations is given by

$$N_\nu = \frac{\Gamma_z - \Gamma_{vis}}{\Gamma_{\nu\nu}} \tag{2.2}$$

where

$$\Gamma_{vis} = \Gamma_{ee} + \Gamma_{\mu\mu} + \Gamma_{\tau\tau} + \Gamma_{hadronic}. \tag{2.3}$$

The standard model predictions for the individual partial widths are

$$\begin{aligned} \Gamma_{ee} = \Gamma_{\mu\mu} = \Gamma_{\tau\tau} &= 83.4^{+1.3}_{-0.6}\, MeV \\ \Gamma_{hadronic} &= 1734^{+47}_{-21}\, MeV \\ \Gamma_{\nu\nu} &= 166^{+2.7}_{-0.7}\, MeV \end{aligned}$$

where the uncertainties are derived from allowing a variation of the top quark mass from 50 to 250 GeV, the Higgs mass from 20 to 1000 GeV, and the strong coupling constant α_s from 0.09 to 0.15.

The total width of the Z°, Γ_z, is not a free parameter in the standard model with a fixed number of generations, once the couplings and particle masses have been fixed. However the total width can be measured in a fairly model independent way, by fitting the hadronic cross section[3] data in the following way.

[3]In fact any channel can be used, but the hadronic channel offers a far greater statistical precision

A lineshape is described in terms of a resonance term and a pure QED term. In addition this lineshape is convoluted with an initial state radiation function as described in section 2.2.1. The resonance term is an s-dependant Breit-Wigner (equation 2.2.1) with M_z, Γ_z and an overall normalization factor as free parameters (allowing these three parameters to vary independently allows departure from a strict standard model calculation). The number of neutrinos can then be determined by using the best fit value of Γ_z in equation 2.2, Γ_{vis} coming from substituting predicted values for the terms in equation 2.3.

2.2.4 Determination of the Number of Neutrino Generations by a Standard Model "Free-Neutrino" Fit

In this method the number of neutrinos is allowed to be a free parameter in an otherwise rigid standard model. The total width and the pole hadronic cross section are constrained by the equations

$$\begin{aligned} \Gamma_z &= 3\Gamma_{ee} + \Gamma_{hadronic} + N_\nu \Gamma_\nu \\ \sigma_{had}^{pole} &= \frac{12\pi\Gamma_{ee}\Gamma_{had}}{M_z^2\Gamma_z^2} \end{aligned}$$

where σ_{had}^{pole} is the hadronic cross section at $s = M_z^2$ before initial state radiative corrections are applied. The Standard Model values in section 2.2.3 are used for the partial widths. The hadronic cross section data are fitted with the only free parameters being N_ν and M_z, and the number of neutrino generations is determined by the best fit value of N_ν. This measurement is statistically the most precise, but theoretically relies heavily on precise calculations within the standard model. Experimentally a large fraction of the systematic error arises from the absolute determination of luminosity as the measured peak cross section determines the value obtained for N_ν.

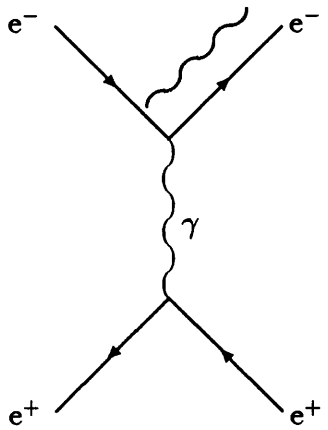

Figure 2.6: Principle background to neutrino counting by a direct measurement of the cross section

2.3 Determination of the Number of Neutrino Generations from a Measurement of the Single Photon Cross Section

This method of neutrino counting is to directly measure the cross section for the $\nu\bar{\nu}$ production. Events where just a $\nu\bar{\nu}$ pair are produced will not be seen in the detector so the process used to measure the cross section is $e^+e^- \rightarrow \nu\bar{\nu}\gamma$, where the photon is radiated from either the incoming positron or electron (fig 2.1). Thus the signal for this process is a single photon in the detector, and nothing else. The advantage of this method is that it is the least model dependant of the three; it relies only on the theoretical calculation of a single relatively simple electroweak process, and furthermore it is in principle the most sensitive measurement of the three as the cross section increases by about 30 % for an extra generation. The main disadvantage of the method is the large background that arises from radiative Bhabha scattering (see fig 2.6) where both the charged particles are lost down the beam pipe. The signal is also experimentally difficult to trigger on without introducing an unacceptable background rate. By operating at an optimized energy above the Z° (100 - 104 GeV), the background can be reduced and the triggering made more straightforward by selecting only high

energy photons, as the photons arising from the signal have an energy spectrum peaked at approximately $\sqrt{s} - M_z$ whereas those arising from the background have an energy spectrum almost independent of $\sqrt{s}$. However the overall cross section is so low that operating in this energy range only becomes worthwhile once the machine luminosity is high.

As a preliminary investigation to assess the feasibility of the measurement, generators were used for both the signal and background processes to study the single photon energy spectrum. For the signal process, the generator of Mana and Martinez [17] was used, which in addition to the lowest order term[4] calculates:-

1. The important soft and virtual corrections to e+e- $\rightarrow \nu\bar{\nu}\gamma$
2. The cross section for e+e- $\rightarrow \nu\bar{\nu}\gamma\gamma$.

In the second case the single photon signal can be imitated if the second photon is outside the detector acceptance or below the required energy threshold, or the two photons are sufficiently collinear so as to be detected as a single photon. To simulate a realistic detector configuration, cuts are applied on the detected photon as follows:-

- $\theta_\gamma > 15°$ (i.e. that the γ is inside the end cap lead glass acceptance)
- $E_\gamma > 1$ GeV (minimum energy for gamma detection)
- Second γ (if generated) fails above criteria, or is within 5° of first photon, in which case they are assumed indistinguishable.

The effect of the higher order corrections is summarised in table 2.1, where the cross sections correspond to the above selection.

The background is simulated using the generator TEEGG [18]. Care is required simulating the background as the "standard" generators for Bhabha scattering (used for studying wide angle Bhabha scattering and luminosity processes) are not suitable when one of the incoming particles scatters at zero angle. This has in the past led to backgrounds for neutrino counting to be significantly underestimated. The TEEGG generator includes:-

[4]Note that as this is a radiative process the "lowest order" term is $O(\alpha^3)$

1. Lowest order calculation

2. Soft and virtual corrections by an approximate technique.

3. e+e- $\rightarrow$ e+e-$\gamma\gamma$ using matrix elements of Martinez and Miquel [19].

For the background, if the either the electron or positron scatter by more than 2.3° then it is considered detected, and thus the event can be rejected. The selection criteria for the photon are the same as for the signal process. Fig. 2.7 shows the detected photon energy spectrum for both signal and background, using the selection criteria for signal and background described above, running on the peak of the Z° resonance (a nominal Z° mass of 92 GeV is assumed). The signal is displayed under the assumption of both three and four neutrino generations, but the background completely overshadows the distinction. Whilst various measures can be taken to improve this situation, it is unlikely a competitive measurement can be made. The situation considerably improves for energies above the Z°. The background remains (kinematically) limited to approximately 5 GeV by the veto on scattering angles $> 2.3°$, whereas a substantial fraction of the signal extends to much higher energy. Fig. 2.8 shows the photon energy spectrum of the signal process at a beam energy of 104 GeV. The effect of higher order radiative corrections is also shown in this plot. By means of a suitable energy cut, background can be virtually eliminated, leaving only the small cross section as a major limitation on the precision of the measurement. For a realistic set of cuts a cross section of 0(30-40pb) could be expected, although a full detector simulation is needed to calculate a final number.

2.4 Theory of Luminosity Measurement

2.4.1 Outline of Luminosity measurement at LEP

A measured cross section at an e^+e^- collider experiment is given in terms of experimental observables by

$$\sigma_{e^+e^-\rightarrow YY} = \frac{N_{YY}}{\epsilon_{YY} \times \mathcal{L}_{e^+e^-}}$$

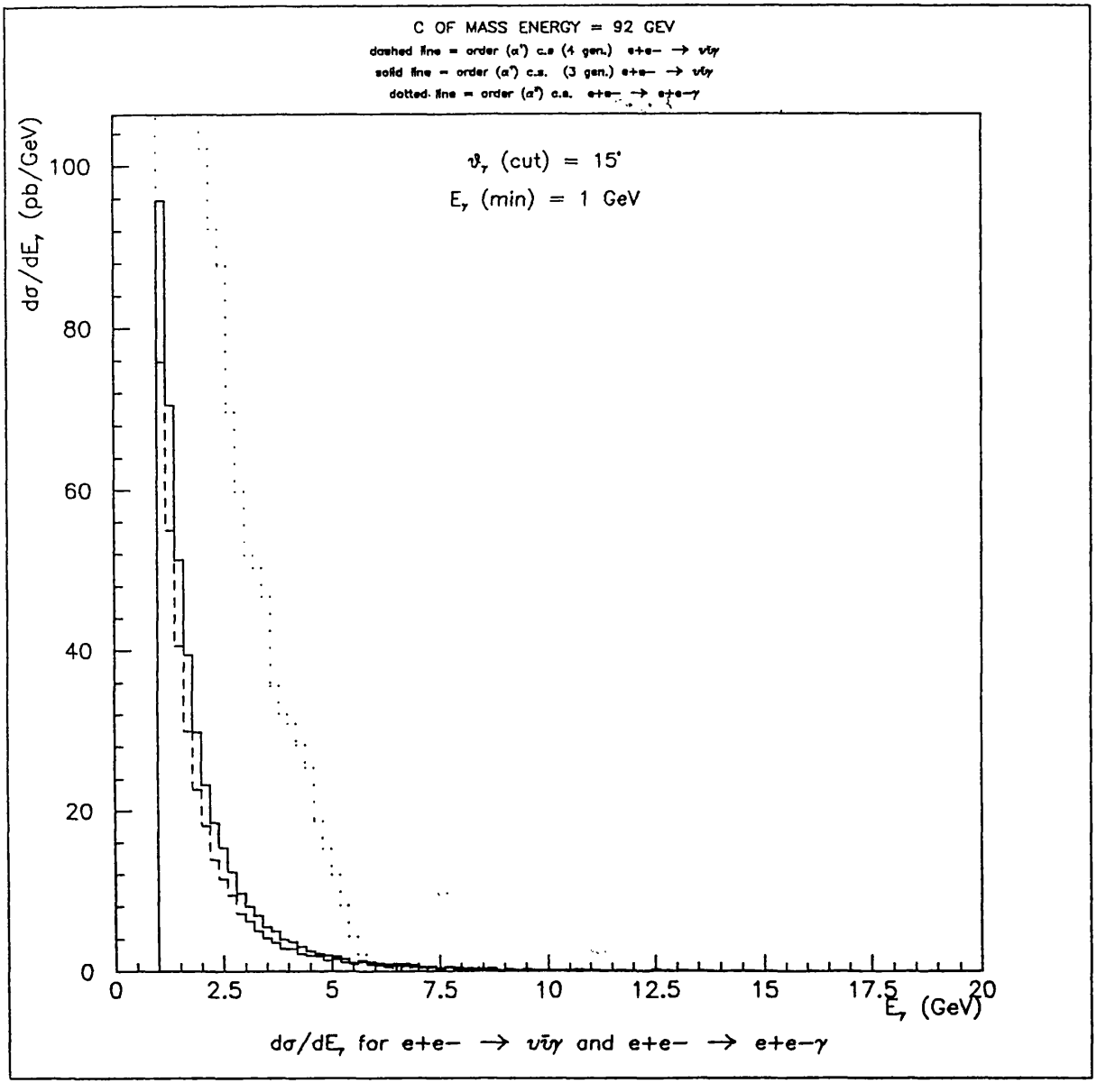

Figure 2.7: Differential cross section distribution showing the energy spectrum of the γ in the processes e+e- $\rightarrow \nu\bar{\nu}\gamma$ and e+e- $\rightarrow$ e+e-γ

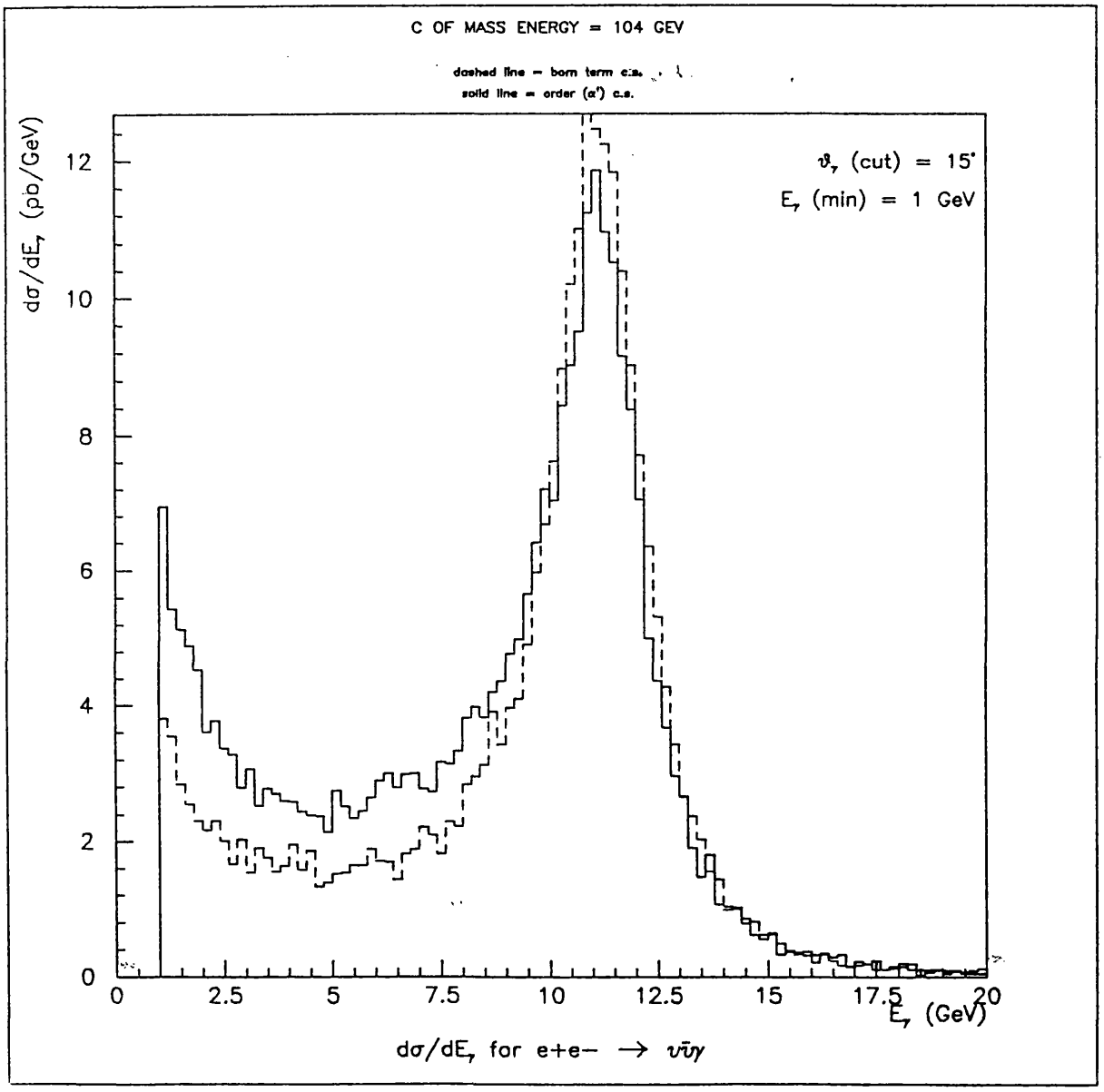

Figure 2.8: Differential cross section distribution showing the effect of radiative corrections on the energy spectrum of the γ in the process e+e- $\rightarrow \nu\bar{\nu}\gamma$ at E_{cm} = 104 GeV

where N_{YY} is the number of observed of events of type YY, ϵ_{YY} is the efficiency for detecting such events, and $\mathcal{L}_{e^+e^-}$ is the machine luminosity, representing the intensity of collisions of the electron - positron beams. To measure the luminosity, the above equation is inverted

$$\mathcal{L}_{e^+e^-} = \frac{N_{YY}}{\epsilon_{YY} \times \sigma_{e^+e^- \to YY}}$$

but now the process $e^+e^- \to YY$ must be one that is understood theoretically rather than one that is being studied. In e^+e^- colliders this has conventionally been achieved by measuring the rate of elastic e^+e^- collisions, as these are well described by the long established theory of QED. The differential cross with scattering angle θ for this process is given approximately by

$$\frac{d\sigma}{d\theta} \propto \frac{1}{\theta^3} \tag{2.4}$$

so the cross section is peaked at low scattering angle. At previous e^+e^- colliders a high statistics measurement has been possible at low angle, while a determination with lower statistical precision but often higher systematic precision was possible studying wide angle Bhabha scattering. At LEP, the wide angle option is no longer available, as for scattering angles greater than 10°, the Z° has an increasingly large contribution to the process, which becomes dominant at scattering angles greater than about 45°; thus a measurement in this region would rely on calculations in the electroweak sector of the standard model - precisely the sector LEP is primarily designed to test. Furthermore at LEP, the high rate of signal processes (due to the Z° resonance) mean that there is a greater demand for high statistical precision in the luminosity measurement. Therefore one is obliged to measure luminosity in the forward region where the t-channel photon exchange ensures a high rate QED dominated process.

From equation 2.4 the integrated cross section is given by

$$\sigma \propto (\frac{1}{\theta^2_{min}} - \frac{1}{\theta^2_{max}}).$$

The OPAL forward detector, used for measuring low angle bhabha scattering has a nominal acceptance of $40mr < \theta < 120mr$. The cross section is highly sensitive to the inner edge of the acceptance, which consequently must be known to a high

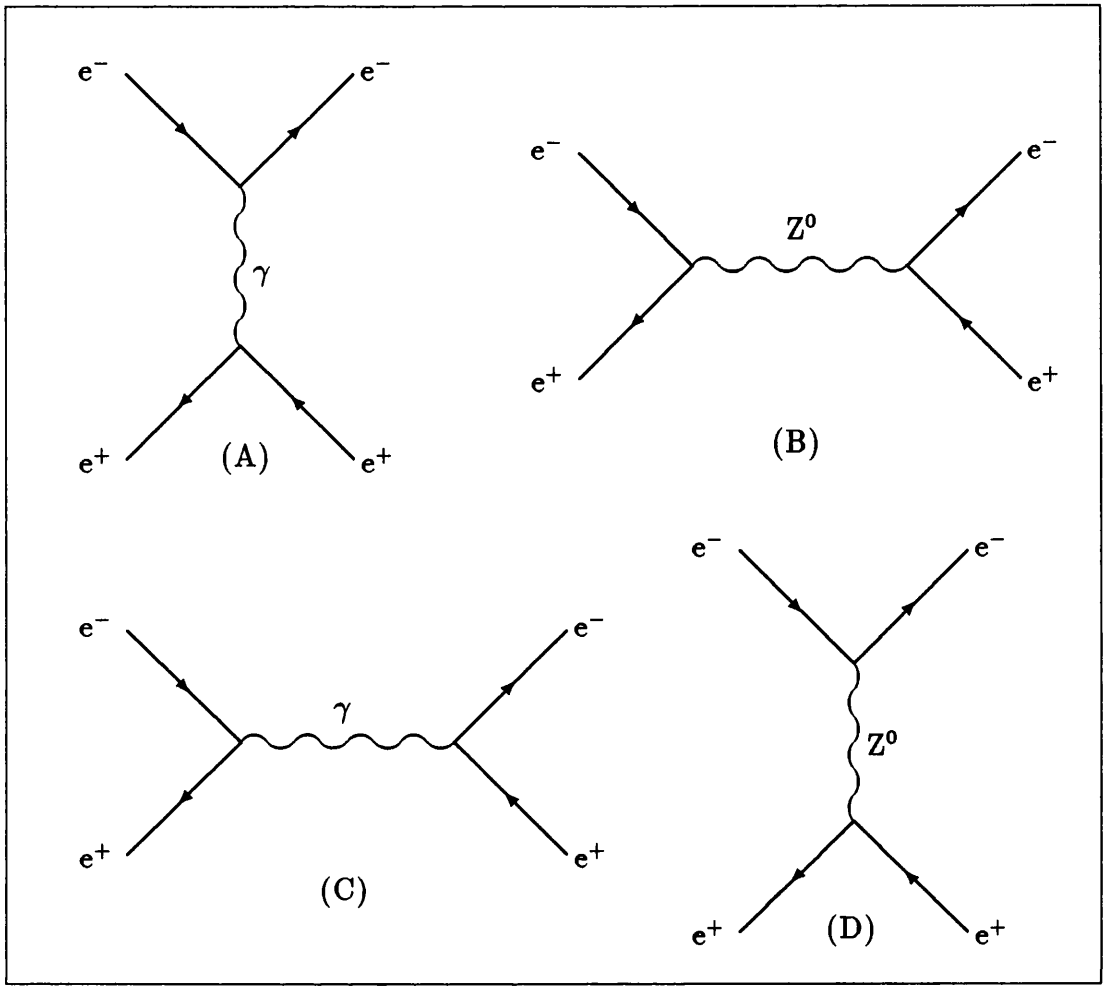

Figure 2.9: Lowest order Feynman diagrams for Bhabha scattering

accuracy. As an illustration of the sensitivity of the luminosity to the absolute position of this inner edge, if one uses the nominal OPAL forward detector inner acceptance angle, then a 1 mm error in the inner edge generates a 2% error in the luminosity.

2.4.2 Calulation of the Cross Section for Bhabha Scattering

The lowest order Feynman diagrams of Bhabha scattering are shown in figures 2.9. The differential cross section for this process corresponding to the QED diagrams is given by

$$\frac{d\sigma_0}{d\Omega} = \frac{\alpha^2}{16E_b^2}\left(\frac{3+\cos^2\theta}{1-\cos\theta}\right)^2, \tag{2.5}$$

where α is the fine structure constant, E_b is the energy of the $e^{\pm}$ beam, $d\Omega = dcos\theta d\phi$, θ and ϕ being the polar and azimuthal angles of the outgoing $e^{\pm}$. In calculating the above expression, the electron mass, m_e, was assumed negligible compared to E_b. For the θ range used for measuring luminosity at OPAL diagram 2.9A dominates, and equation 2.5 simplifies to

$$\frac{d\sigma}{d\theta} = \frac{8\pi\alpha^2}{E_b^2\theta^3} \tag{2.6}$$

which is the Rutherford scattering formula.

The lowest order calculation is insufficient for the precision of a few percent in the luminosity measurements that is the target for LEP experiments, and the following corrections must be included:-

- QED initial state radiative corrections
- $\gamma - Z$ interference terms
- Vertex and vacuum polarization diagrams

Of these, the largest are the QED radiative corrections to the t-channel diagram. The Z° contribution is of order 1%, and thus any uncertainties in this cause a negligible error in the luminosity measurement. A generator including the above corrections to first order, BABAMC [20] is available which calculates total cross sections over a given angular range and in addition can produce an unweighted event sample. The error in calculating cross sections for luminosity has been quoted verbally by one the authors of the generator to be 1% at various talks and workshops, although it is difficult to find a written confirmation of this figure. The error arises from the estimated size of higher order diagrams.

Total Cross Sections (pb) for e+e- $\rightarrow \nu\bar{\nu}\gamma$			
Energy	Lowest order	after soft and virtual corr.	after soft/virt and hard corr.
92 GeV	77.7 ± 0.3	47.4 ± 0.18	66.1 ± 0.2
96 GeV	153.1 ± 0.4	91.5 ± 0.3	149.3 ± 0.3
100 GeV	86.1 ± 0.2	49.3 ± 0.1	88.4 ± 0.1
104 GeV	52.6 ± 0.1	31.8 ± 0.1	59.8 ± 0.1

Table 2.1: Total cross sections for e+e- $\rightarrow \nu\bar{\nu}\gamma$ with radiative corrections

Chapter 3

The OPAL Detector

The OPAL detector (**Omni Purpose Apparatus for Lep**) was designed with the aim of being able to detect all Z° decay products (except neutrinos) so as to be sensitive to the full spectrum of electroweak physics. It was therefore required to be able to identify electrons, muons and hadronic particles and accurately measure their 4-momenta, covering as much of the 4π solid angle as possible. The philosophy of OPAL was to use proven detection techniques and thus be ready to take data from the first day of LEP operation. This chapter describes the detector, with emphasis on the parts used for the mass and width measurement, and with special detail given to the forward detector on which the author worked. A more comprehensive description can be found elsewhere[21]. The Detector is shown in perspective in fig 3.1, with the OPAL co-ordinate scheme marked and sub-detectors labeled, and sectional views are shown in figs 3.2, 3.3.

3.1 The Central Detector

The Central Detector consists of three separate drift chambers, designed to operate together to measure the origin, four-momentum and dE/dX of charged tracks. It is contained in a region with a uniform magnetic field of 0.435 Tesla, which allows the momentum of tracks to measured through their curvature.

Surrounding the carbon fibre beam pipe is the Vertex Chamber which is 1 m long and 470 mm in diameter. It consists of an inner layer of 36 axial jet

cells containing 12 anode sense wires, and an outer layer of 36 stereo jet cells containing 6 anode sense wires and inclined at an angle of $\sim 4^o$.

The axial cells give an r-ϕ resolution of $\sim$ 50 μm and the axial and stereo measurements give a z resolution of $\sim$ 5 cm. It is intended to detect the decays of long lived particles such as B mesons and τ leptons and to improve momentum and z resolutions of the track measurements.

The Jet Chamber is a cylinder of length about 4 m with internal and external diameters of 0.47 m and 3.7 m, respectively. It contains 24 identical sectors, each with 159 anode sense wires and 2 cathode planes, the sense wires being staggered to avoid left-right ambiguities. The chamber gives good coverage of solid angle; 98% of 4π has at least 8 points on a track. The average resolution per point of the jet chamber is 160 μm in the $r - \phi$ plane. The z-coordinate is calculated from charge division and is measurable to within 5 cm.

Outside the Jet Chamber lie the Z Chambers – 24 chambers each 4 m long and 50 cm wide. Each chamber contains 8 bidirectional cells with 6 wires spaced by 4 mm. They are designed to give a precise measurement to the z-co-ordinate of Jet Chamber tracks, the Jet Chamber being optimized for $r-\phi$ measurements. The Z resolution obtained is $\sim 300\mu$m, dominated by survey errors.

A track trigger system is driven from the central detector, which can set a trigger based on having some programmable number of tracks. A track is defined as a set of hits lying in broad band of r-z and is recognized by a purpose built processor, which is sufficiently fast to be used in the primary OPAL trigger (section 3.6)

3.2 Time of Flight Counters

The Time of Flight Counters consists of plastic scintillator covering the barrel ($|cos\theta|$ <0.82) region, inside the electromagnetic calorimeter. The detector is divided into 160 segments in azimuth, each segment covering the whole polar angle range. They provide information on the time of arrival of a particle with respect to the beam crossing with a resolution of 460 ps and can identify particles by giving their velocity, reject out of time signals such as cosmic rays, and act

as a primary trigger.

3.3 Calorimetry

The Electromagnetic Calorimeter is split into two sections, the barrel, and the end cap, both of which are composed of lead-glass blocks. The barrel contains 9,440 lead-glass counters made of a newly developed glass SF57, with a density of 5.5 g/cm^3, covering 82% of 4π. The blocks are positioned such that the gaps do not quite point to the interaction region. The counters' longitudinal length of 37 cm corresponds to 24.6 radiation lengths. Each block is optically polished and wrapped in a black film of vinyl fluoride laminated with mylar. Phototubes at the rear of the blocks collect Cerenkov light radiated from the electromagnetic shower created by an incoming particle. The energy resolution for electrons is $\sigma_E/E = 0.2\% + 6.3\%/\sqrt{E}$.

The endcap leadglass covers 17% of 4π at $10^o < |\theta| < 35^o$, and is composed of CEREN 25 leadglass, polished and covered in aluminium foil and mylar. Vacuum phototriodes are optically coupled to the blocks with epoxy resin. The blocks give at least 20.5 radiation lengths for possible trajectories from the interaction region. At low energy, the resolution can be represented by $\sigma_E/E = 0.5\% + 5\%/\sqrt{E}$. This does not improve so rapidly at energies above $\sim$ 10 GeV due to shower leakage, though it can be improved by use of the presampler information.

Fluctuations arise from the energy lost by a showering particle in the aluminium of the magnet and in the end walls of the Central Detector pressure vessel. There are Presamplers placed immediately in front of the lead glass, which can be used to improve lead glass energy measurements by detecting the degree of preshowering, so any energy loss can be corrected. In the barrel region this detector consists of an array of limited streamer tubes, and in the end cap region thin high gain multiwire chambers. The Presamplers can also improve the resolution of the position measurement of electromagnetic showers. The Hadron Calorimeter is an iron sampling calorimeter read out with wire chambers and cathode pads, but as 80% of energy from a multihadronic event is deposited in the electromagnetic calorimeter, it was not necessary to use it in this analysis.

3.4 Muon Detectors

Muon detectors cover the barrel and endcap regions, consisting of drift chambers in the barrel region, and arrays of streamer tubes in the endcap region. This system lies outside the Hadron Calorimeter, so virtually all particles other than muons originating from the interaction region will have been absorbed before reaching this detector. The muon detectors were not used in this analysis.

3.5 Forward Detector

The Forward Detectors complete the electromagnetic calorimetry by covering the region between the endcaps and the beam pipe ($40< \theta <120$ mrad) leaving the beam pipe region itself the only part of the solid angle through which electrons and photons can escape undetected from OPAL. The detectors are optimized to detect electrons and positrons from low angle Bhabha scattering, for the purpose of measuring the luminosity of collisions in OPAL, the principle of which was described in section 2.4. The practical details will be discussed further in chapter 5, but the key factors affecting the design were the need to precisely define an inner edge of acceptance in polar angle θ, and the need to separate true Bhabhas from background by precise energy measurement and by being able to require a back to back condition in azimuthal angle phi. There are two identical forward detectors, one at each end of OPAL.

The need for specialized forward detectors for luminosity measurement at LEP and SLC is far greater than at lower energy e+e- colliders such as PEP (Stanford,California) and PETRA (DESY,Hamburg). At such previous colliders wide-angle bhabha scattering could be used as a luminosity determining process. At LEP, wide angle bhabha scattering is dominated by the Z° contribution, and extremely low angle bhabha scattering is the only QED dominated process with a sufficiently high rate. Another feature of LEP is that the large cross section to multi-hadrons at the peak of the Z°, coupled with the clarity of the multi-hadronic signature, has made the determination of the number of multi-hadronic events extremely precise ($\sim$1%). It is therefore desirable to match this accuracy

as closely as possible in the luminosity measurement, to achieve precise cross sections from which the Z° lineshape parameters can be extracted. (By contrast, experiments at the PETRA e+e- collider at DESY, Hamburg, attained systematic errors in the luminosity measurement of approximately 3% after several years of running, with little motivation to improve on this.) The choice of very low angle Bhabha scattering for luminosity measurement allows high statistical precision, but inevitably leads to problems of beam related background, and achieving a precision luminosity measurement has been one of the greatest challenges at LEP.

The forward detectors are themselves composed of several separate detectors in order to provide cross checks on the detector performances, alternative luminosity measurements that are largely independent, and to meet the different demands of absolute and relative point to point measurements. One of the forward detector is shown in fig 3.4 with the separate sub-sub-detectors labelled.

3.5.1 Forward Calorimeter

The calorimeter is of lead-scintillator sampling type, composed of 39 identical layers of 3.4mm lead and 6.0mm scintillator It is in two parts; the pre-radiator and the main calorimeter, 4 and 20.5 radiation lengths thick respectively, and is divided into 16 azimuthal (ϕ) segments. The light deposited in the scintillator in the main calorimeter is read out by BBQ bars mounted on the inner and outer edges; the pre-radiator is read out only on the outer edge. There is a 10mm gap along the vertical axis (necessary for reasons of mechanical construction) but otherwise this design allows complete coverage in ϕ. Beam tests in August 1988 showed the calorimeter to have a resolution of $18\%/\sqrt{E}$ with a θ resolution near the inner edge of ± 0.8 mr, calculated from the ratio of light deposited in the inner and outer BBQ bars. The phi resolution is ± 25 mr, obtained from the ratio of signals in adjacent segments. The resolution is highly dependent on the quality of the calibration so there was some variation in resolution obtained during the running period, but on the whole the performance matched the test beam response.

3.5.2 Proportional Tube Chambers

Sandwiched between the main calorimeter and pre-radiator are three planes of tube chambers used to determine the positions of electromagnetic showers. In the beam tests of August 1988 the position resolution was ± 2 mm. They are read out by a custom built multiplexed readout system. The construction and installation of this readout, the commissioning of the detector and the analysis of the data formed a substantial part of the author's own work and the detector and corresponding data analysis will be discussed in detail in the following two chapters. For the data taken in 1989 the tube chambers provided the most accurate absolute determination of the luminosity, and the normalization of the Z° resonance curve depended directly on these results.

3.5.3 Fine Luminosity Monitor

The Fine monitor is composed of 4 pairs of scintillation counters at each end of the forward detectors , approximately 20cm in front of the Calorimeter front face. Each counter is a piece of type NE102 scintillator connected via a perspex lightguide to a photomultiplier tube. These counters measure luminosity by demanding an end to end coincidence to count bhabha events, the principal feature of the system being a well defined acceptance obtained through precise machining and surveying. They are mounted on an aluminum truss that is supported by the calorimeter. A luminosity determination based on these counters has been performed on the 1989 data, although the analysis was not completed until after the publication of results on the Z° mass and width.

3.5.4 Forward Drift Chambers

The Forward Drift Chambers are mounted in front of the calorimeter, and are designed to give a precision measurement of the position of charged particles entering the Calorimeter. Due to particles showering in material in front of the forward detector, clean measurements will not be possible for every event, so the main role of this detector is to provide a sample of clean events with a precise

position measurement, which can be used to calibrate the position of other parts of the forward detector less sensitive to showering effects. In studies of two photon physics, forward going hadrons can also be detected.

The detector has two layers, one mounted in front of the fine monitor and the second immediately in in front of the Calorimeter front face. Each layer has four chambers. Those nearest the interaction region have composite faces of glass-reinforced plastic (GRP) and polystyrene foam to reduce the probability of secondary interactions occurring in them, whereas those by the calorimeter have GRP faces. Each chamber has two gas gaps, each with two anode wires lying perpendicular to a radius to the centre of the chamber. From cosmic ray and beam tests, the drift chamber resolution in the drift direction is 300 μm and that along the wire of the axis 1 mm. Further details of construction and performance are given in Appendix B.

3.5.5 Gamma Catcher and Far Forward Monitor

The Gamma Catcher is a small lead-scintillator calorimeter designed to cover a small gap in the acceptance in the region between the endcap lead-glass and the forward Calorimeter. It is 7 X_0 thick and beam tests have shown it to have a linear response for electrons with momenta up to 5 GeV/c. It is intended to act mainly on a veto on background to the process $e^+e^- \rightarrow Z^\circ \rightarrow \nu\bar{\nu}\gamma$. It will also help to define the endcap lead glass inner edge. Noise problem which prevented this device being used in the 1989 data taking were resolved in the winter shutdown of 1989/90.

The far forward detectors are small lead-scintillator calorimeters located either side of the beampipe, 7.85 m from the interaction region. Their polar acceptance angles are between 5 and 10 mrad and so they measure a large Bhabha rate. While this detector is not likely to produce an accurate absolute number for luminosity, it's high rate allows a high statistics fill by fill measure, and immediate feedback to the LEP control room on the effect in changes in the beam orbit. Although operational in the during the 1989 data taking, these detectors were not fully analysed due to the urgency of understanding other detectors.

3.6 The OPAL Trigger and Data Aquisition

3.6.1 The general OPAL trigger

The beam crossing rate at LEP is approximately 45 kHz; this is to be compared with an expected "physics rate" of 1 to 5 Hz. A fast hardware trigger makes a decision whether or not to read out within 16 μs of the beam crossing, so allowing the subsequent beam crossing to be sampled if a trigger is not generated. Many sub-detectors create one of more individual triggers which are used in various AND and OR combinations to generate an OPAL trigger. If a trigger is generated then data is digitized, and passed to the Filter crate via the Event Builder, the latter merging data from the different sub-detectors. All sub-detectors are read out for each triggered event irrespective of the source of the trigger. The Filter performs a fast software analysis of the digitized data to classify the event. For the 1989 data taking events were flagged to aid rapid analysis of interesting data offline, but it is envisaged that as LEP increases luminosity it will be necessary to use the Filter to reject events online. The data is then passed to a VAX 8700 which writes data to cartridges. The VAX also performs the function of the general control of the running of the experiment.

3.6.2 The Forward Detector triggers

The forward detector contributes five triggers[1] to the OPAL main trigger unit. Any one is sufficient to cause a full OPAL readout.

a) At each end, the summed energy recorded in the calorimeter is > 15 GeV

b) At each end, the summed energy in any two adjacent pairs of segments is > 12 GeV, and the two pairs are back to back in azimuth. This trigger exploits the collinearity of Bhabha events to use a lower energy threshold.

c) A fine monitor trigger, which requires hits in three counters out of the four in a set of two back to back pairs, together with an energy deposition in

[1]There is also a Gamma Catcher trigger, but as this detector was not used during the 1989 data taking the trigger was not operational

the calorimeter > 12 GeV in the two segments behind the fine monitor counters.

d) A single end trigger of the summed energy measured at one end >12GeV. This trigger samples the off-momentum particles deflected into the forward detector. Due to a high rate, this trigger is prescaled before being passed to the central trigger.

e) Trigger d) together with tracks or electromagnetic clusters detected elsewhere in the detector. This enables the collection of tagged two photon events.

In the early part of the running used for this analysis, the triggers operated only on the energy in the main calorimeter, with a threshold set to compensate for the *average* energy lost in the pre-radiator. This was found to have some inefficiency for events with a high deposition in the pre-radiator, so the energy sum trigger was then altered to operate on the total energy deposited.

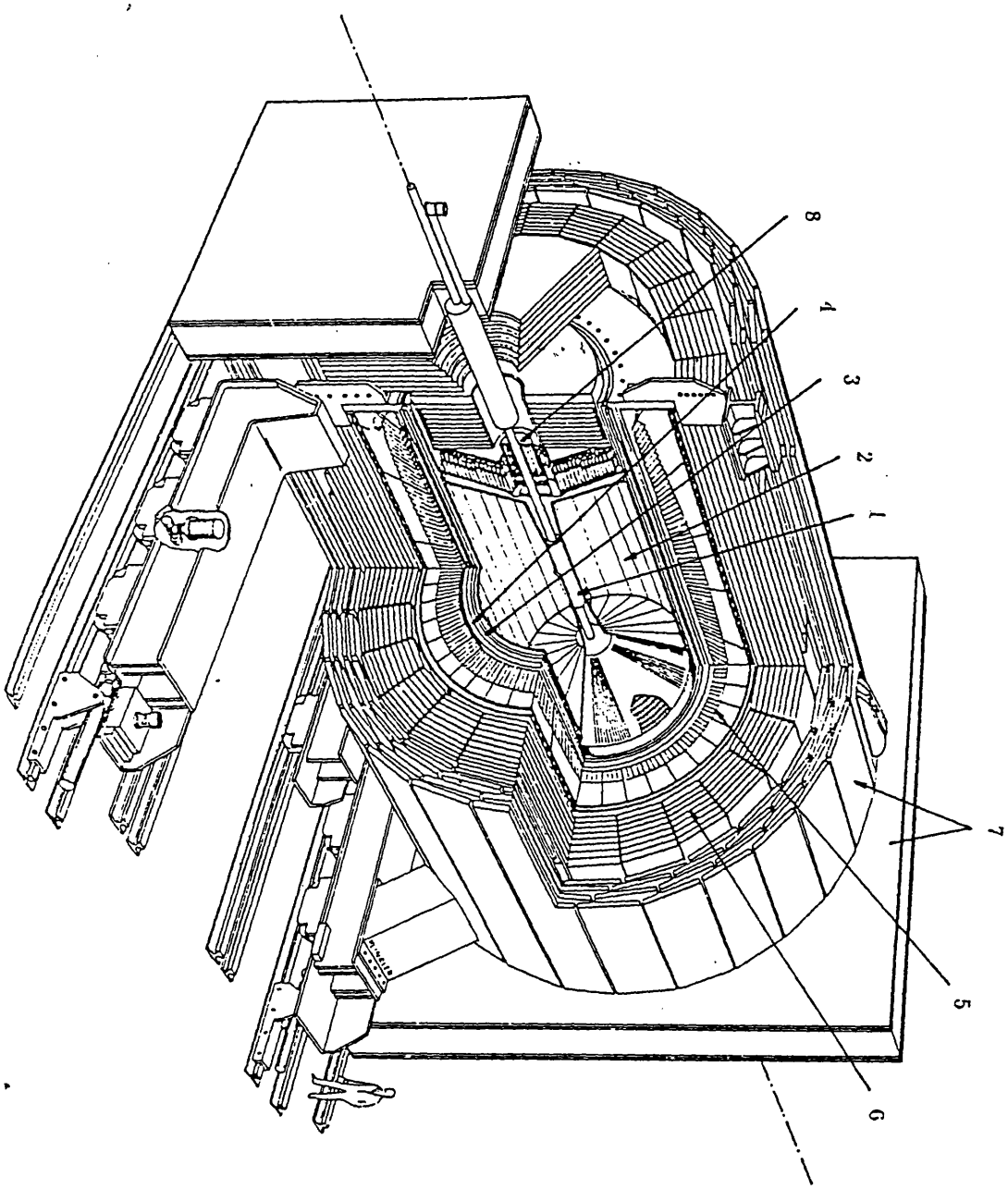

Figure 3.1: OPAL detector shown in perspective, showing all sub-detectors.

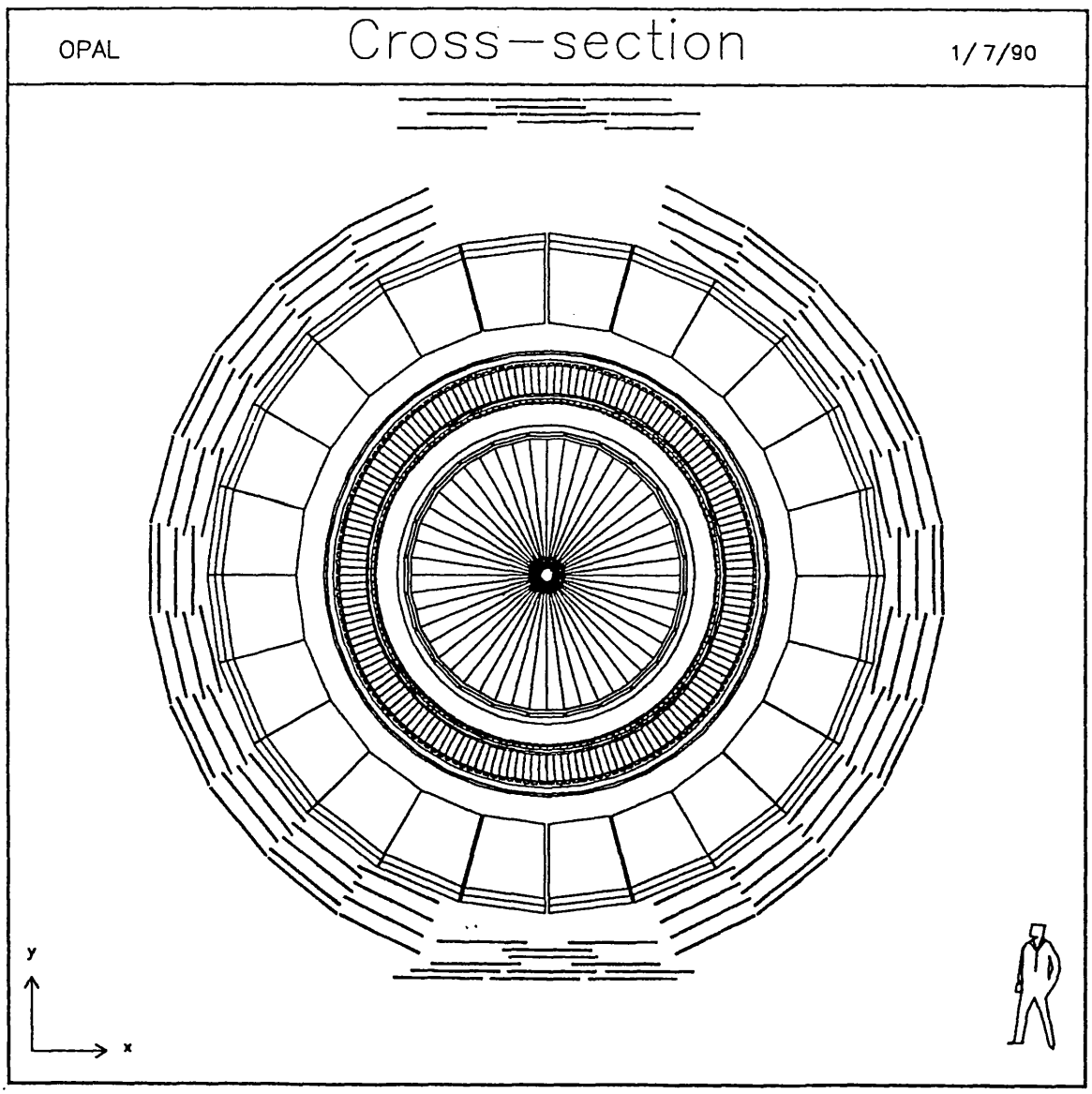

Figure 3.2: OPAL detector in x-y section

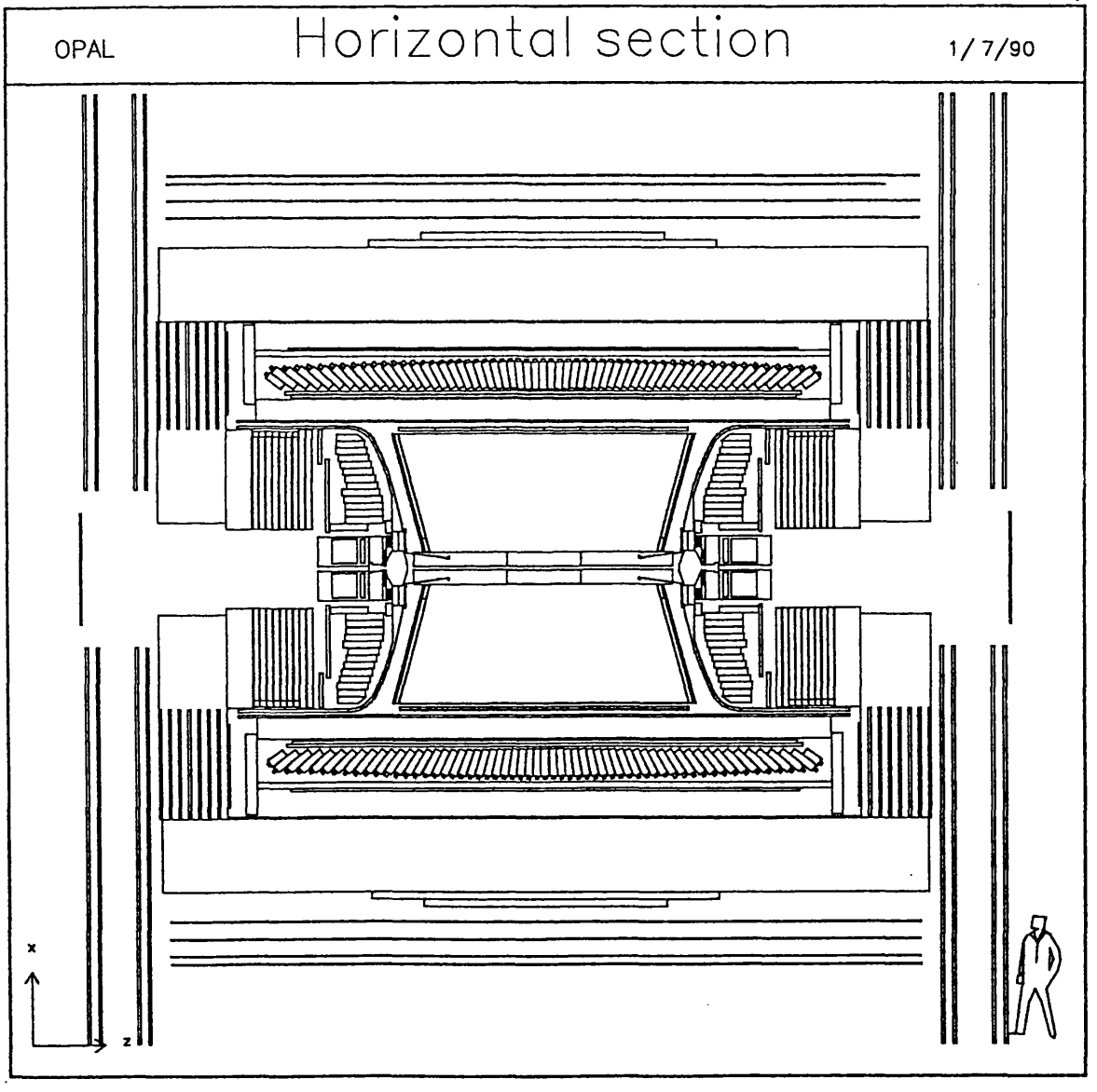

Figure 3.3: OPAL detector in y-z section

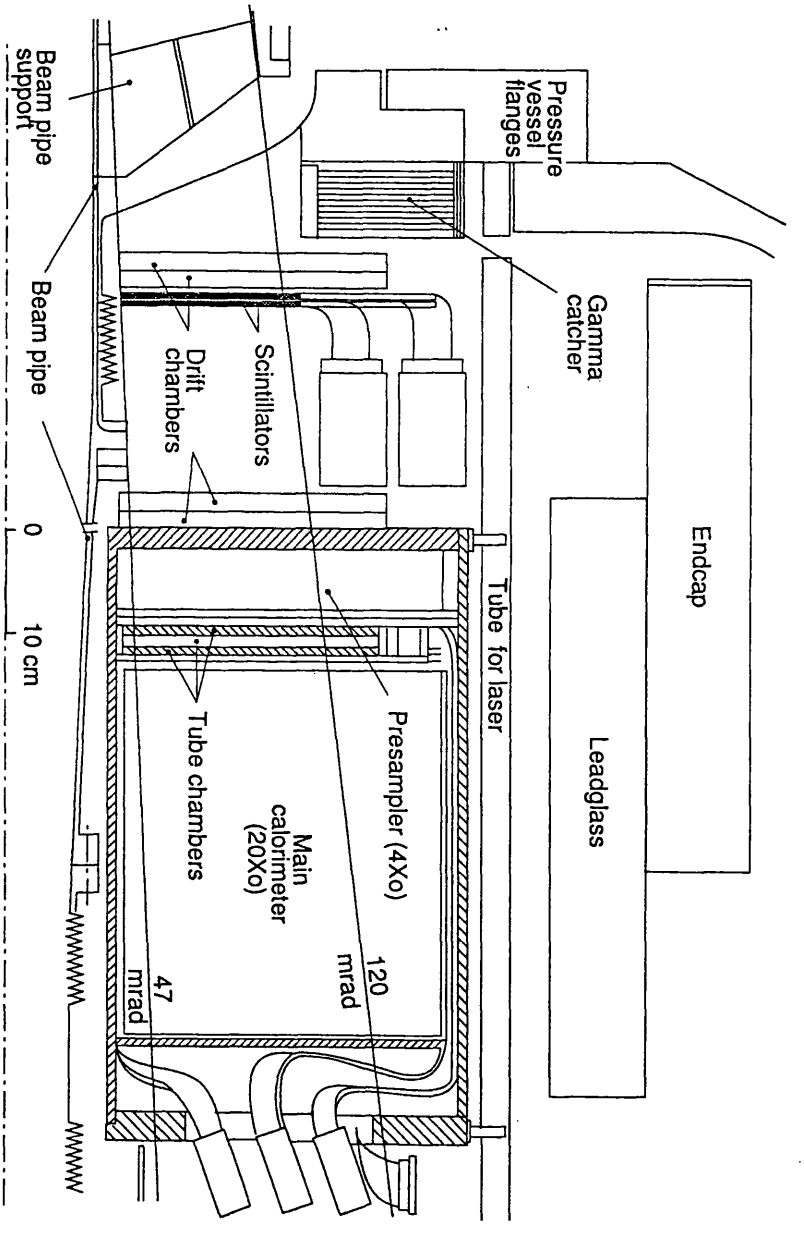

Figure 3.4: OPAL forward detector in y-z section. Seperate components are labelled.

Chapter 4

The Forward Tube Chambers; Design, Readout and Performance

4.1 Design aim of the Forward Tube Chambers

As outlined in section 2.4, as a result of Bhabha scattering having a rapidly varying differential cross section with polar angle θ, a high precision position measurement of the outgoing particles from this process is of vital importance in making an accurate luminosity determination. Both the calorimeter and the forward drift chambers measure the position of Bhabha electrons, but each has its problems. The calorimeter measures polar angle θ by the ratio of light gathered in its inner and outer readout strips. The accuracy obtained is highly dependant on the calibration of each channel, and in any case is highly non-uniform, being very good at the inner edge but rather poor at the outer edge. The drift chambers are in principle highly accurate devices, but technically more demanding to operate, read out, and analyse. Furthermore, at the time of designing the forward detector, it was unknown what the background conditions would be, and it was feared that the drift chambers might be inoperable some or even all of the time due to syncrotron radiation or other background.

The tube chambers were envisaged as an accurate position measuring device,

giving a uniform response across their acceptance, thus acting as an independent check on the calorimeter in its good region, and as the primary measurement where the calorimeter is poor. Unlike the drift chambers, which are designed to measure minimizing ionizing tracks and so are highly sensitive to beam related background, the tube chambers measure the position of a shower with $\sim$ 100 particles. The position of the tube chambers inside the calorimeter provides considerable shielding and further reduces their sensitivity to beam effects.

4.2 Mechanical Construction

A particle originating from the interaction region passes in sequence through three planes of tubes, with the axes of the tubes being horizontal, diagonal and vertical. The diagonal tubes have this axis pointing towards the beam axis. Each of the 3/8$''$ ($\sim$ 9.6mm) brass walled square cross section tubes contains a single anode wire running down the centre, the case of the tube being earthed. In each layer, the tubes covers an approximately annular area centered around the beam pipe. The tubes therefore have varying lengths in the range 50-300 mm. The tube layers are divided into quadrants, with no tubes crossing quadrant boundaries at 0,90,180 and 360 degrees. There are two separate D-shaped boxes or "tube chambers" at each end, mounted inside the two separate halves of the calorimeter. The complete detector therefore comprises four identical tube chambers (two at each end of OPAL), each chamber containing two quadrants each composed of three planes. Fig. 4.1 shows half of one tube chamber with a single quadrant plane of tubes drawn. The sensitive area of the detector covers a range of approximately $50 < \theta < 145$ mrad in polar angle, and almost the complete azimuthal range, except for a gap where the two calorimeter halves are joined. The tubes become less sensitive at the ends; however the measurement of the position of an electromagnetic shower will in any case be biased when part of the shower extends beyond the edges of the detector, and so the region of good position measurement is smaller than the sensitive area. This point will be discussed further in chapter 5.

4.3 Electrical Connections to the Detector

4.3.1 High Voltage

Each quadrant plane of tubes has a separate high voltage connection for the anode wires, and a separate cable running to the high voltage supply unit. Each channel of the high voltage unit supplies two quadrant planes via a fanout crate located inside the gondala[1]. Each tube is connected to the high voltage supply of its quadrant plane via an individual 75 MΩ resistor, so that if a wire breaks and shorts to the brass tube wall, a current of $\sim$ 20 μA will be drawn from the supply, but the rest of the plane can remain in operation. The absolute maximum high voltage is +2 kV (limited by the signal coupling capacitor). The high voltage and signal connections for one tube are shown in the circuit in fig 4.2. The high voltage cables from each quadrant plane run inside the calorimeter shell to a patch panel at the rear. This panel carries all the tube chamber electrical connections. The walls of the tubes from different planes are insulated from one another, the grounds being connected together and to the low voltage circuit on the outside of the chamber.

A monitoring system was developed to check the tube chamber high voltage unit for trips, and to reset channels that had tripped. Trips tended to occur at two points in the LEP cycle; when ramping the beam energy and carrying out the final focus, and when the beam was lost. Both these were accompanied by high rates in the forward calorimeter. Trips were rare while the beams were stable at full energy.

4.3.2 Signal and Low Voltage Connections

There are 32 signal channels per quadrant plane. A largely one to one correspondence exists between tubes and channels; however some of the shorter tubes are

[1]A 'gondala' is a prefabricated hut where the racks of electronics, computers and power supplies necessary to operate the detectors are located. They are so named because they are hung from and slide along rails on the ceiling like cable cars (locally called Gondolas) used in the many ski resorts in the region surrounding Geneva

electrically coupled together. A preamplifier for each channel is mounted on the outer edge of the tube chamber box. These pre-amplifiers are miniature hybrid circuits, physically arranged into "blocks" of sixteen channels. The tube anode wire is a/c coupled via a 100 pF capacitor to the input of the amplifier (fig 4.2). In the configuration used the amplifiers give a differential output of maximum level $\pm$ 200 mV . From each block a flat cable runs inside the calorimeter shell to the patch panel at the rear where external connections are made. Each whole quadrant has a separate low voltage ($\pm$6 V) connection to power the pre-amplifiers, and each block receives power in parallel.

4.4 Charge Integrating Multiplexed Readout

A technical description of the readout with full circuit diagrams is presented in Appendix A. This section outlines the principles of operation of the system.

The tube chamber detector at each end has 384 channels. There is a severe space restriction for running cables to the forward detector in OPAL, so the signals are multiplexed using a UCL designed system of special circuits. There are two principal components in the system; the 'mothercards' located on the detector itself, which are inaccessible when all components of OPAL are in position for data taking and can only be reached during major shutdowns, and the 'eurocrate' which is accessible at all times in the gondala. The mothercards are circuit boards based around the ALEPH multi-channel charge integrating amplifier hybrids [22], there being an integrator channel for each of the 384 output channels of the detector. Each mothercard contains 4 8-channels hybrids and is connected to the 32 channels of a single quadrant plane. There are 12 mothercards at each end of the detector. The operation of the mothercards is controlled by the eurocrate, this crate also acting as an interface to the main OPAL readout chain. A gate is opened for 4μs, timed so the beam crossing occurs in the middle of this gate, and the charge from each tube chamber channel is individually stored on it's integrator. If an OPAL trigger is not generated, then these integrators are cleared in the 6.5μs, before the next crossing. In the case of a trigger, each integrator is read out sequentially, the analogue charge

integral is digitized and the data is stored in a local memory in the eurocrate The crate sets a flag to indicate that it has ended it's readout sequence, and the data can then be accessed by the master processor in the VME crate controlling the forward detector online system.

With this system, each half of the detector at one end is read out using a single 20-way twisted pair cable for both digital mothercard control signals and the analogue data. The data read by the VME processor and written to the output stream (and ultimately onto raw data tapes) is a value of the charge collected on the anode wires of each of the 384 channels of the detector at each end. It is envisaged that some level of zero suppression and online reconstruction will be implemented at a later stage, but for the 1989 data taking this was not necessary.

4.5 Measurement Technique

As the tubes are operated in the proportional mode, the charge collected measures the number of particles passing through each tube. After four radiation lengths, a 50 GeV electromagnetic shower has a transverse spread of several tube widths and contains $\sim$100 particles so the tube chambers can measure a profile of the particle density of the shower. For a single shower a single plane of tubes makes a measurement of the centre of the shower position in one dimension. The horizontal tubes measure the particle position in the vertical direction, and vice versa. From the horizontal and vertical tubes a co-ordinate for the polar angle θ and azimuthal angle ϕ of the event can be obtained. The diagonal tubes can then be used to check this result, and resolve ambiguities in the case of more than one cluster. A typical shower profile is shown in fig 4.3.

4.6 Operating Conditions

The gas used for the Tube Chambers was 40% Ethane - 60% Argon. The tube chambers shared the same gas system as the forward drift chambers, and this gas mix was chosen primarily for the drift chambers in order to give a drift

speed insensitive to small changes in the mixing ratio. The tube chambers were tested with different gas mixtures in test beam studies in August 1988 and the performance was found to be insensitive to the gas used (except in so far as changing the overall chamber gain, which could be compensated for by using different high voltages). The final operating high voltage was set at + 1.5 kV; this value gave a high efficiency without showing any evidence of saturating the gain of the chambers or electronics.

4.7 Reconstruction Software

A reconstruction program was written by the author to find cluster centroids in each of the individual quadrant planes, and combine these 1-dimensional hits to form 2-dimensional cluster positions. The output reconstructed data for each cluster comprises a value for R (the distance from the centre of the beam pipe to the point where the incoming particle hit the calorimeter front face),ϕ (the OPAL azimuthal angle) and the charge integral (the sum of the pedestal subtracted ADC counts from all the tubes used to make the cluster). The charge integral is a measure of the particle multiplicity of the electromagnetic shower as it passes through the tube chambers. The position co-ordinates are derived from the horizontal and vertical planes; the diagonal plane is used to resolve ambiguities in the case of more than one cluster in one of the planes. This program was developed to analyse the data collected during the test beam of 1988, then integrated into the main OPAL reconstruction program, ROPE.

4.8 Results from August 1988 Test Beam Run

4.8.1 Test Beam Arrangement

The tube chamber detector and readout was first tested under realistic operating conditions using the SPS X5 electron beam in the West Area at CERN, which was tunable from 5 - 80 GeV. A summary of the results from this test has been reported [23]. The chamber had been tested with a radioactive source and

the readout tested with pulses, but since the detector was designed to observe showers of large numbers of particles a high energy beam was needed for a test of the full system.

At this time one full quadrant of readout electronics was available. The mode of operation of the readout crate had to be altered as the SPS has a beam spill of $\sim$ 2 seconds and so, unlike LEP, events did not occur at a predetermined time. Consequently the integration gate could not be opened in advance of an event. The solution adopted was to have a continuous cycle of having the gate open for a long period (100 μs) followed by a fast reset ($\sim$ 10μs). When a trigger occurred, the gate was immediately shut (to prevent charge leakage), and the full readout sequence took place. This meant that the tube chambers were not active for $\sim$ 10% of the time, but the events occurring in the reset part of the cycle were flagged, so a clean sample of tube events could be extracted.

4.8.2 Position Resolution Studies

It was not possible to perform an absolute calibration of the tube chamber positions as the beam position was spread over a range of $>$ 1 cm (to be compared with the mm scale precision required for luminosity measurement), and such a calibration would in any case have been made redundant by the need to disassemble the calorimeter after the test beam to replace light guides. A first estimate of the position resolution was obtained by comparing the measured position of the centroid by the diagonal plane with the position predicted from the diagonal projection of the horizontal and vertical planes. The difference of these values is plotted in fig 4.4. From the RMS of this distribution one extracts a single plane position resolution of 1.6 mm. This is obtained from data with the beam entering the calorimeter at a single position in the centre of the detector, and so represents a measure of resolution limitations from shower statistics, gain variation, electronic noise, and other event by event fluctuations in the operation of the detector and readout. More extensive studies were carried out with data obtained at LEP as will be described later in this chapter.

4.8.3 Energy Dependance of Results

Figure 4.6 shows the dependance of the position resolution (measured by the method described above) with energy over the range 5-80 GeV. This plot shows that although position resolution is degraded at lower energies, the tube chambers are capable of measuring e.m. showers down to 5 GeV. Furthermore the system is optimized for showers in the region of 50 GeV as will be encountered at LEP. The variation of the charge integral with energy is shown in fig 4.5. At LEP as the beam energy is injected into the machine at 20 GeV, then smoothly ramped to the peak energy (for the first phase of LEP) of around of 50 GeV, at which point the beams are brought into collision. Although there are a considerable number of particles deflected into the detector with energies in the range 20-50 GeV, the uncertainty in the energy would make it hard to repeat such a study even for energies within this range.

4.9 Performance of the detector at LEP

4.9.1 General Performance

The readout electronics were installed in June 1989 shortly before the OPAL detector was closed and access was lost to the detector. At the time of installation it was found that two planes in the same quadrant of the detector were not working, but in the limited time available it was not possible to trace the fault; thus one quadrant of the right end was not able to generate a co-ordinate. When LEP running began a further quadrant plane (at the left end) was found to be inactive, though in this case the redundancy of the third plane allowed a co-ordinate to be generated. Thus it was possible to measure the position of Bhabha events at both ends in three quadrants out of four. During the 1989 running period, there was a period when a high voltage failure, coupled with an error in the relevant monitoring system, allowed a large number of high voltage channels to trip and remain undetected. This meant that full tube chamber data were only available for approximately three-quarters of the total running period.

4.9.2 Resolution Studies

A Bhabha sample was selected by demanding the following conditions on the tube chamber coordinates :-

1. $R_{left}, R_{right} > 140$ mm
2. $R_{left}, R_{right} < 300$ mm
3. $160° < abs(\phi_{left} - \phi_{right}) < 200°$.
4. $E_{left}, E_{right} > 25$ GeV

R is the radial co-ordinate (i.e. distance from the beam pipe) of the incoming electron on the front face of the calorimeter. The cut at 140 mm is equivalent to a polar θ angle of $\sim$ 58 mrad. ϕ is as defined in the standard OPAL cylindrical coordinate system, with zero directed towards the centre of LEP and $\phi/2$ upwards. E is the energy measured in the forward calorimeters, and this cut is imposed to remove beam related background. The left and right subscripts refer to measurements in the two forward detectors.

To measure the resolution of the chambers, the measurement of R and ϕ at each end were compared for this sample. Fig. 4.7 show distributions of the difference of these coordinates. As the chamber resolution is expected to be a constant distance rather than angle, the angular difference in ϕ is converted to a difference in millimetres using the tube chamber radial measurement. A gaussian curve is fitted to the central part of this distribution to estimate a resolution. The σ of the fitted gaussian is 3.5 mm, which corresponds to a single end resolution of 2.5mm.

As the R and ϕ co-ordinates are generated from different projections of the same x-y co-ordinates one expects the resolution in the two directions to be identical. However one finds that the R distribution is somewhat broader, and contains significantly longer tails than the ϕ distribution. This behaviour is attributed to radiative events. The dominant type of radiation is initial state emission of a photon very close to the beam pipe axis, which will make an event acollinear but not acoplanar. To confirm this explanation of the acollinearly

measured events, a scatterplot was made of the tube chamber ΔR between ends against the difference in calorimeter energy measured in each end (fig 4.8). A strong correlation is seen between an energy difference and a difference in measured tube chamber radius. The correlation has the correct sign to explain a radiative event of the type described above; low measured energy being correlated with high measured radius. If one naively assumes that these events all have a single photon carrying all the missing energy exactly along the beam pipe, then the constraint that total transverse energy must be zero leads to the relation

$$sin(\theta_{left}) \times E_{left} = sin(\theta_{right}) \times E_{right}.$$

Using $sin(\theta) \propto r$, and assuming all the energy is taken from one of the outgoing electrons, we find

$$\Delta E = -E_{beam}\frac{\Delta r}{r_r}$$

where Δ is defined as right - left. With typical values of $r_r = 200$ mm, $E_{beam} = 46$ GeV, one would expect the correlation in the scatterplot to lie along a line with gradient $\sim$ 0.2 GeV/mm, and this is indeed found to be the case. As a further check, a distribution of missing transverse energy was made i) for all events, and ii) for events with more than 5 GeV energy difference between ends (fig. 4.9). The two distributions are similar, the second sample having an only slightly larger width, which can be attributed to the fact that the radiated photon will not be emitted exactly along the beam pipe. To extract a detector resolution from this analysis the phi distribution is used, as it is only affected by final state radiation. This resolution of 2.5 mm is assumed to apply to both the R and ϕ projections.

A further feature of the ΔR distribution is that it's mean is offset from zero by approximately 1 millimetre. However the reconstruction algorithm used the nominal position of the detector in the z direction, whereas it was found from an analysis of the survey data that the right end detector was displaced 12 mm further away from the interaction point than this nominal position. This leads to a higher radial measurement at the right end for Bhabha events of the correct order of magnitude - a typical Bhabha at 70 mrad will be mismeasured high by an amount $12 \times \tan\theta = 0.85$ mm. An appropriate correction was applied to the

reconstruction program.

4.9.3 Correlation of Tube Chamber and Calorimeter Data

It is not possible to draw any conclusions from the comparison of the calorimeter radial measurement with that of the tube chambers, as the calorimeter r is rather poor in the region of the tube chamber acceptance, and the tube chamber radial co-ordinate is used to calibrate the calorimeter radial measurement. However the calorimeter ϕ measurement is based on the energy sharing between different segments and thus relies only on the relative segment to segment energy calibration and is completely independent of the tube chambers. Fig. 4.10 distribution of the difference between the calorimeter and tube chamber ϕ at each end for the Bhabha sample selected by the criteria described above. The calorimeter ϕ resolution varies between 0.2° and 2°, and the tube chamber resolution is $\sim$ 0.9°, so the R.M.S.'s of these distributions is consistent with the combination of these resolutions. The important feature is the agreement on mean ϕ; this serves as a measure of how accurately the tube positions are known with respect to the calorimeter. As the tube chambers are sealed inside the calorimeter and therefore cannot be directly visually surveyed after final installation, this result relates the tube chamber position to the surveyed calorimeter position. Although one would ideally like to determine that there is no error in the radial co-ordianate position of the chambers, it would be somewhat unlikely that the tube planes are displaced so as to give an error in one projection and not the other.

A further interesting comparison is the correlation of the tube chamber charge integral Q with the calorimeter presampler energy deposition. The charge integral for a plane is defined as the total number of ADC counts in the 5 tubes used to form the cluster. The overall charge integral then represents the average of the three planes. A scatterplot of these quantities is shown in fig. 4.11. A strong correlation is seen between presampler energy and tube chamber Q, indicating that the fluctuations in cluster size in the tube chambers are caused by genuine shower fluctuations rather than random variations in the detector response. The presampler energy distribution (also shown in fig. 4.11 is rather broad and has a

tail down to almost zero energy, suggesting there are some events where the particle multiplicity at the depth of the tube chambers is quite small. It is therefore expected that there might be some inefficiency due to such events not producing a shower sufficient to detected in the chambers. This issue will be discussed further in the following chapter.

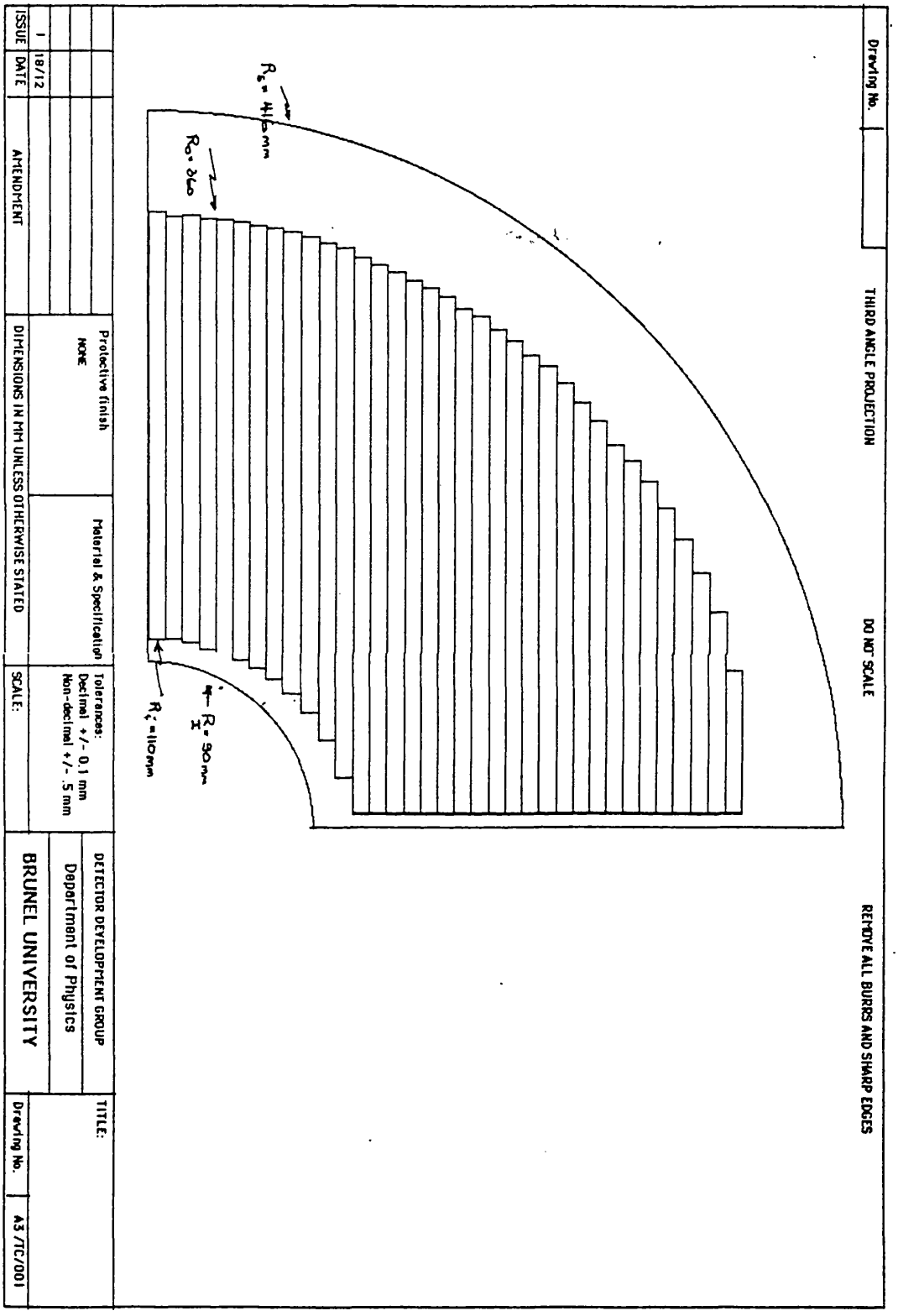

Figure 4.1: Diagram of Tube Chambers. Half of one chamber is shown, with one quadrant plane of tubes exposed

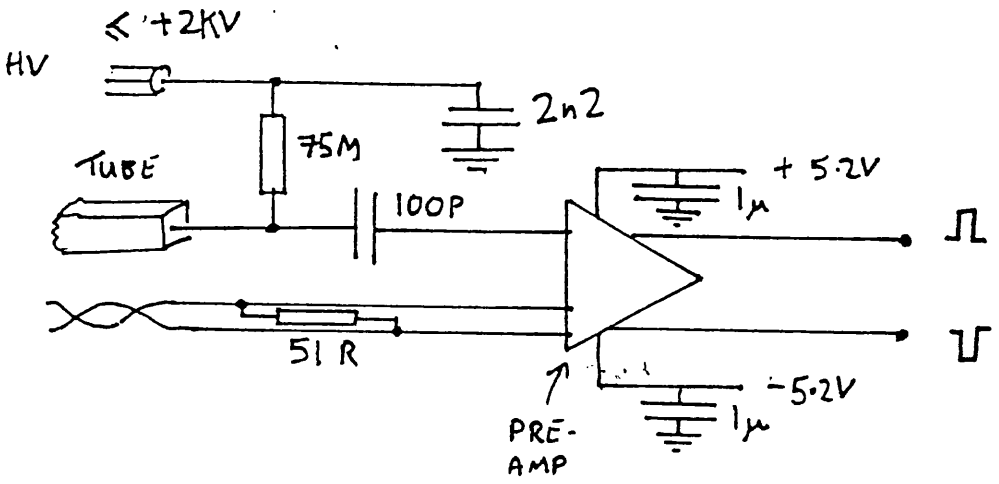

Figure 4.2: Connections of High Voltage and Pre-amplifiers to Tubes

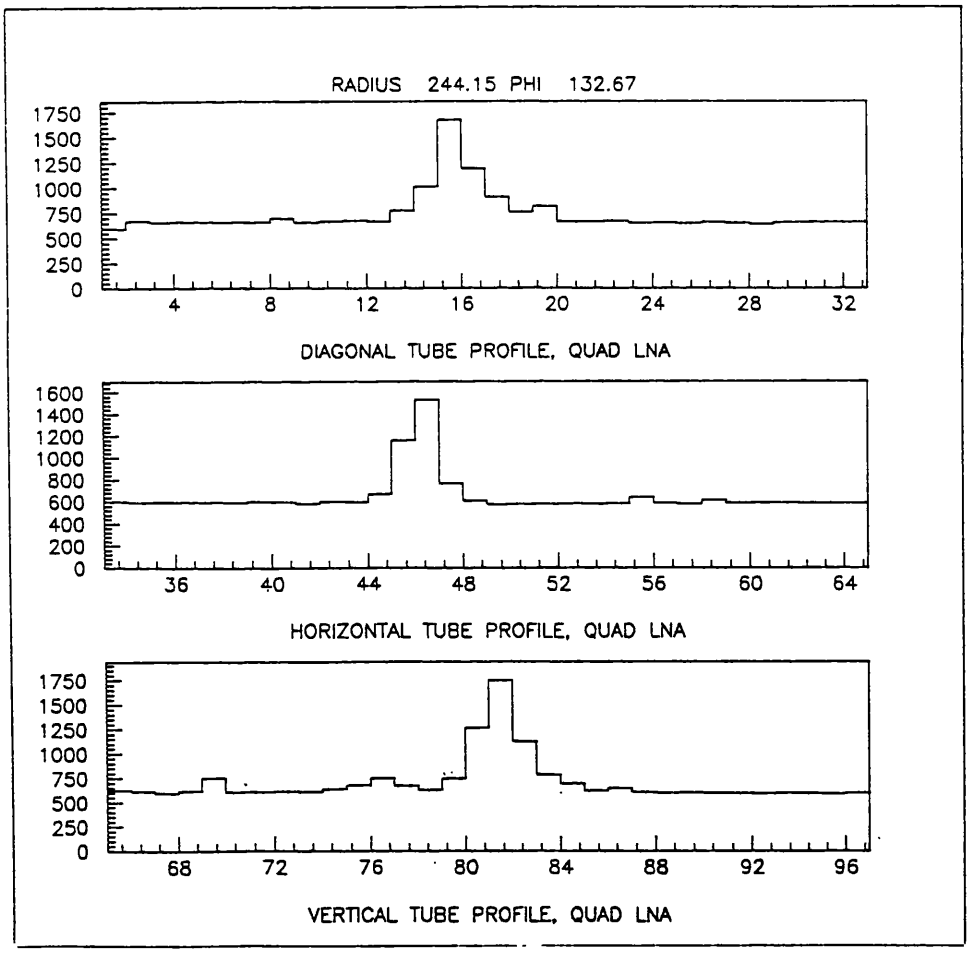

Figure 4.3: Typical 50 GeV shower profile in three planes.

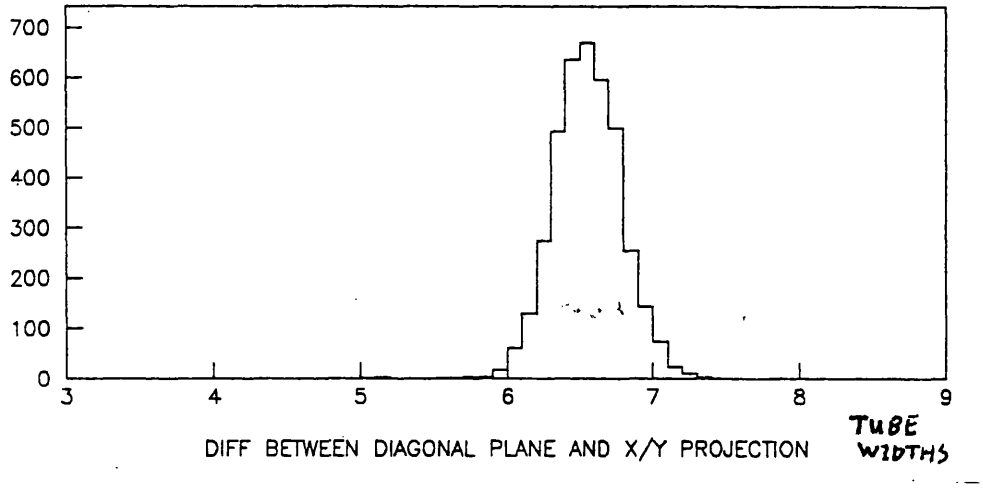

Figure 4.4: Histogram of the difference between direct and indirect measurement in the diagonal plane

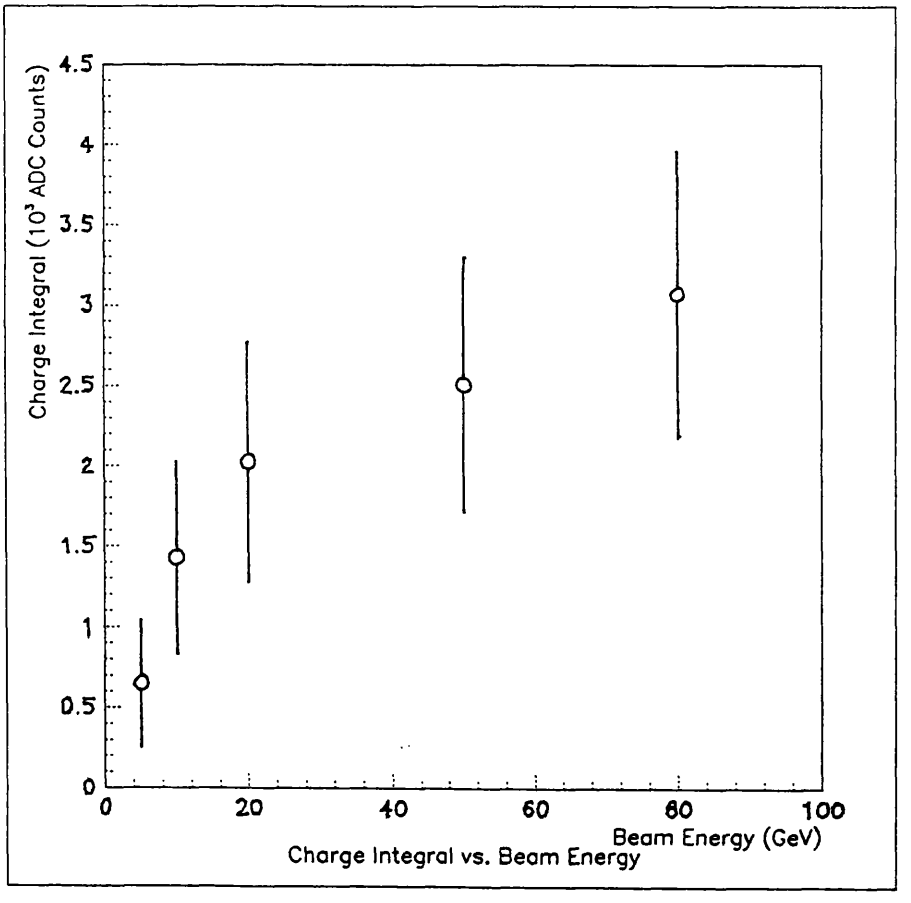

Figure 4.5: Dependance of the charge integral on beam energy in August 1988 test beam

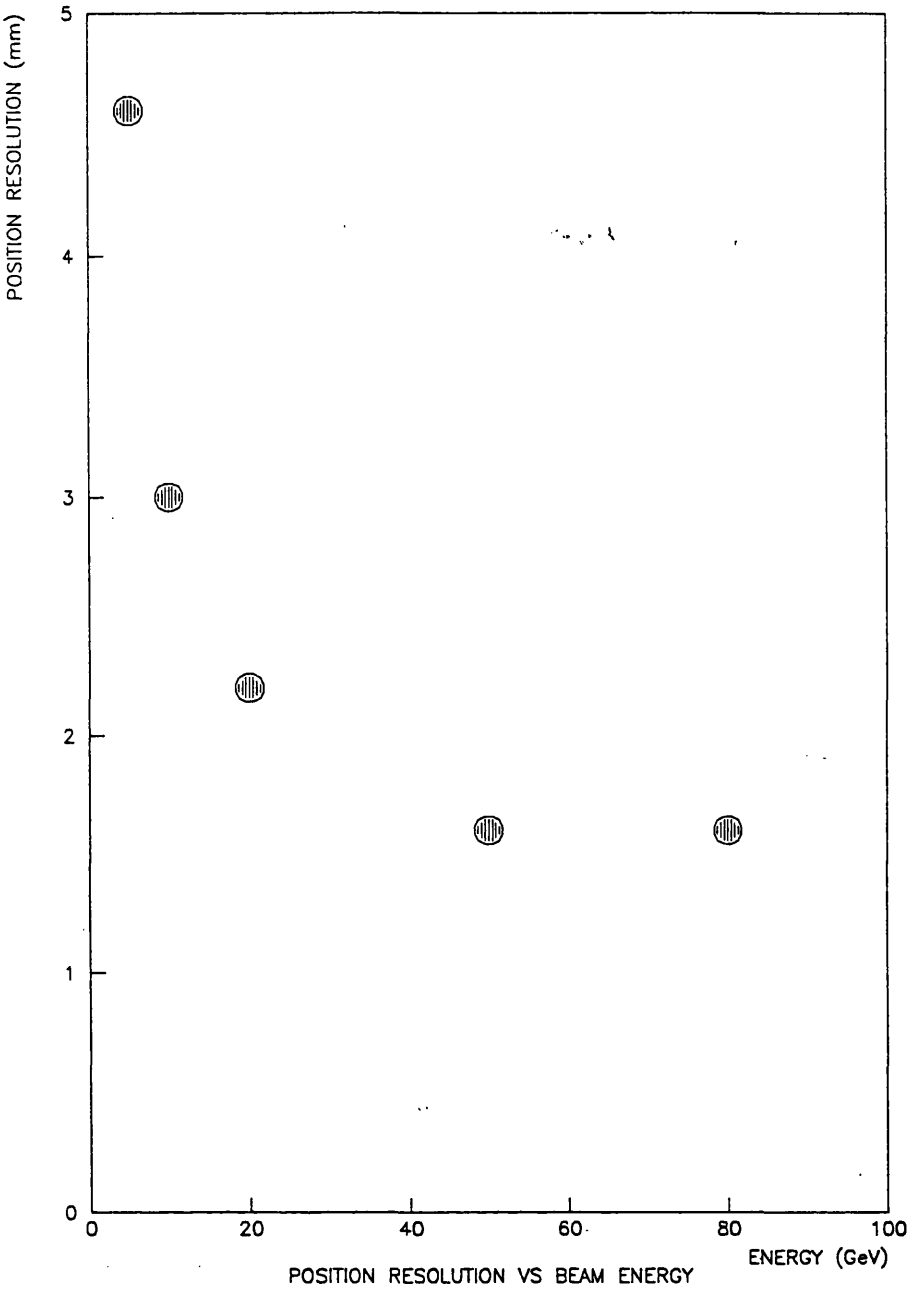

Figure 4.6: Dependance of the position resolution on beam energy in August 1988 test beam

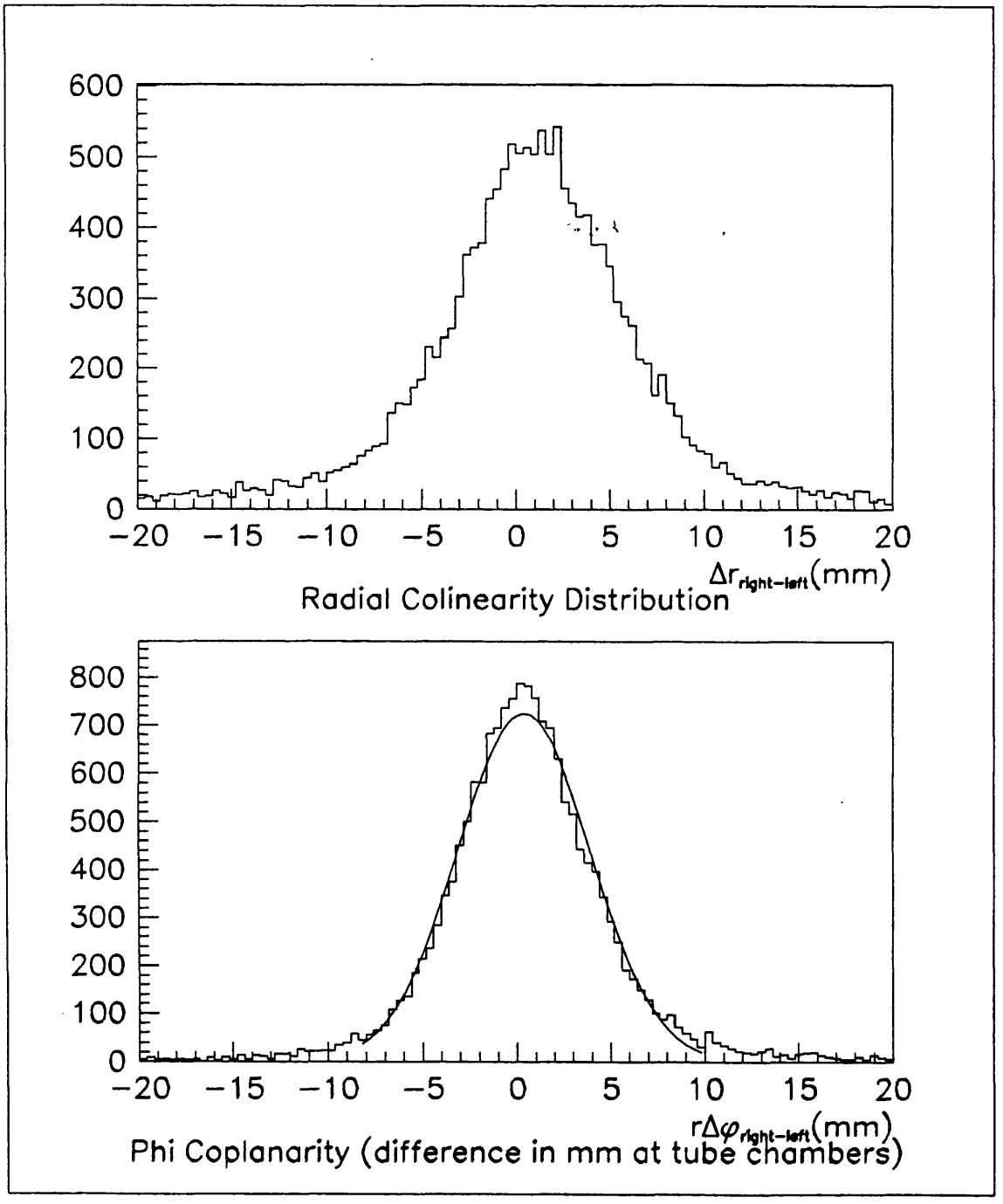

Figure 4.7: Distributions showing the difference (right - left) in R and Phi measured between the two ends for Bhabha sample.] For Phi distribution, the difference is given in mm, accounting for the radius at which the measurement took place

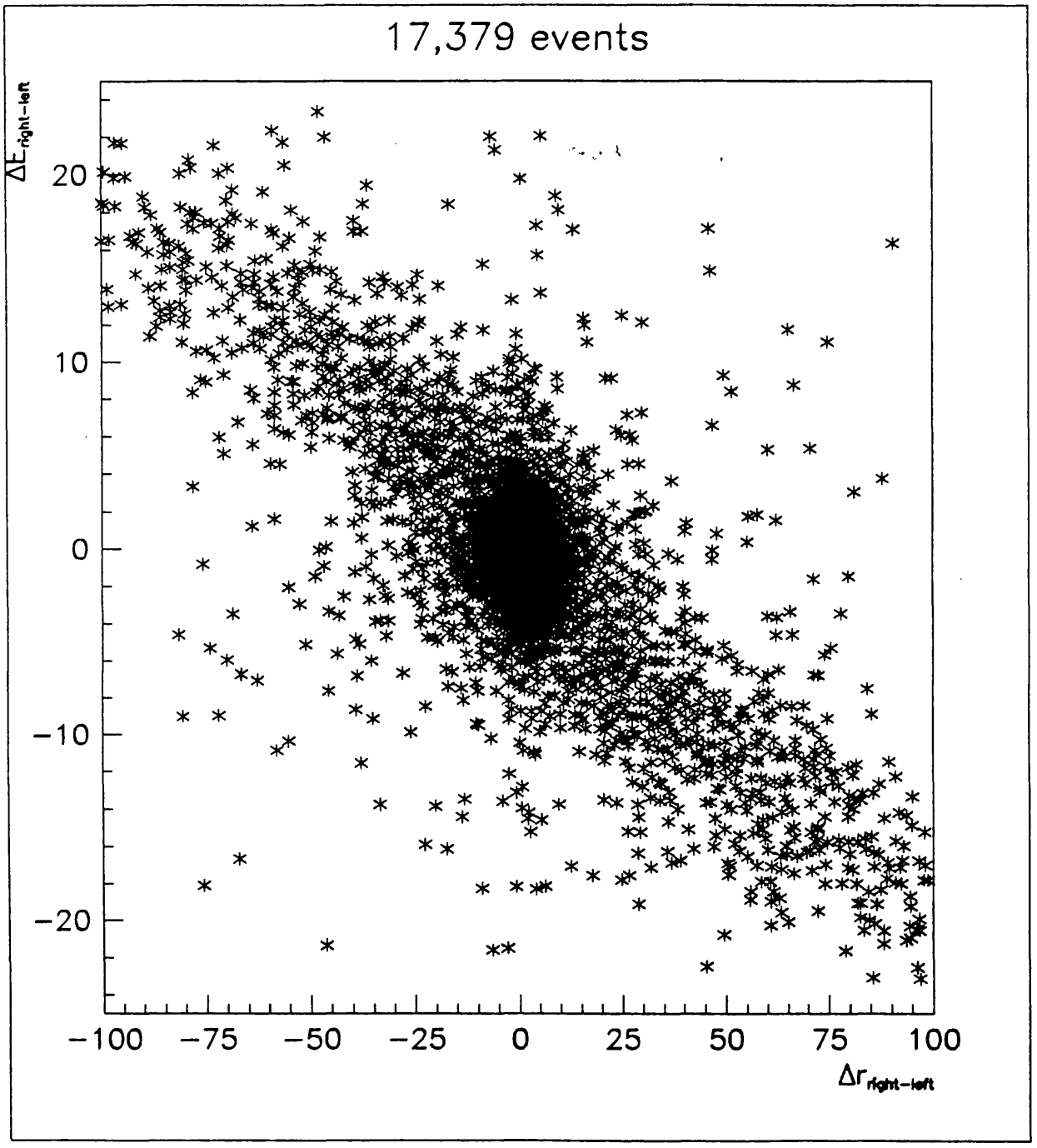

Figure 4.8: Scatterplot of the difference in energy between ends (GeV) and the difference between ends in radial tube chamber measurement.

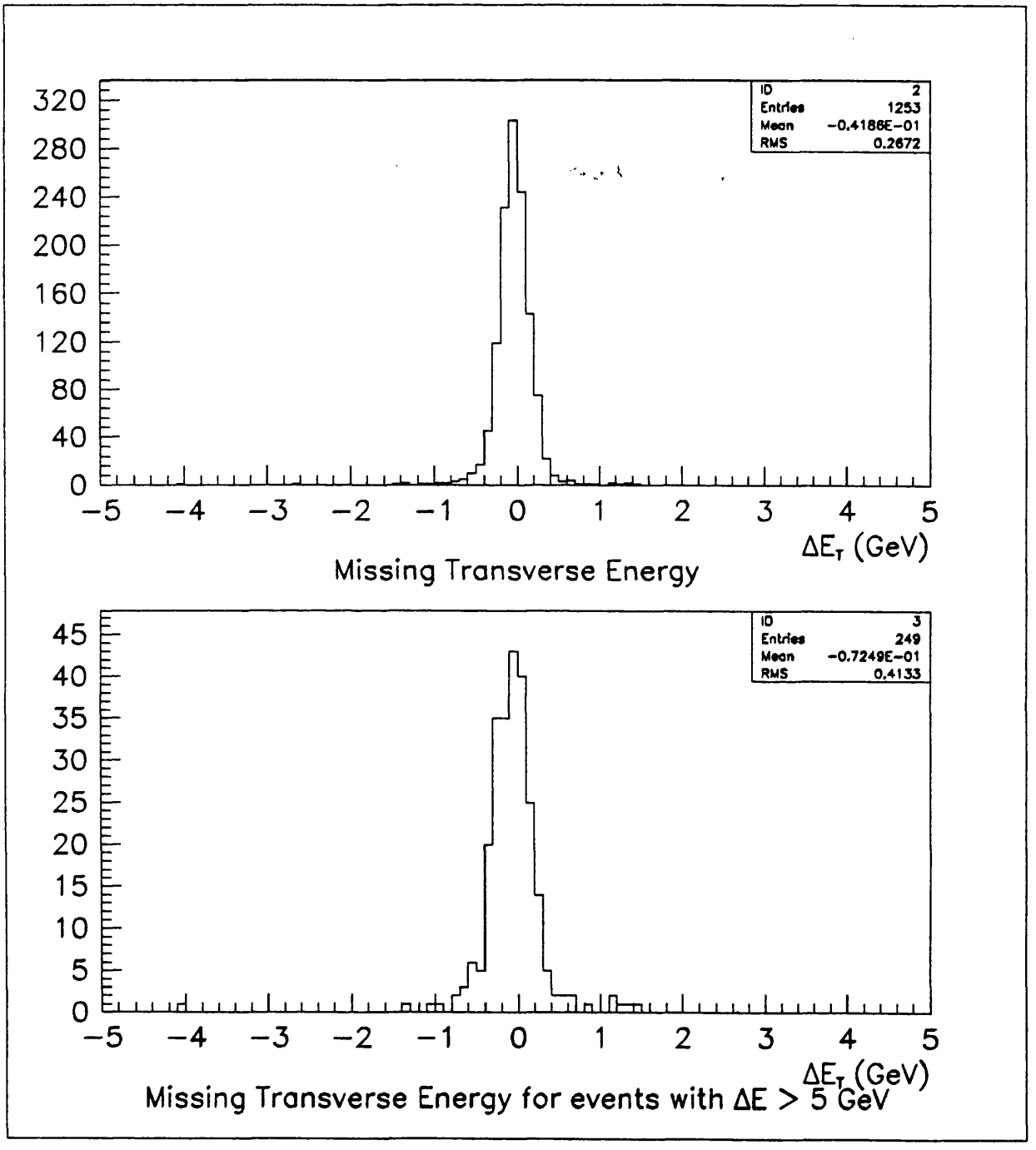

Figure 4.9: Distributions showing the missing transverse energy for a) all events and b) events with a difference in measured energy between ends greater than 5 GeV.

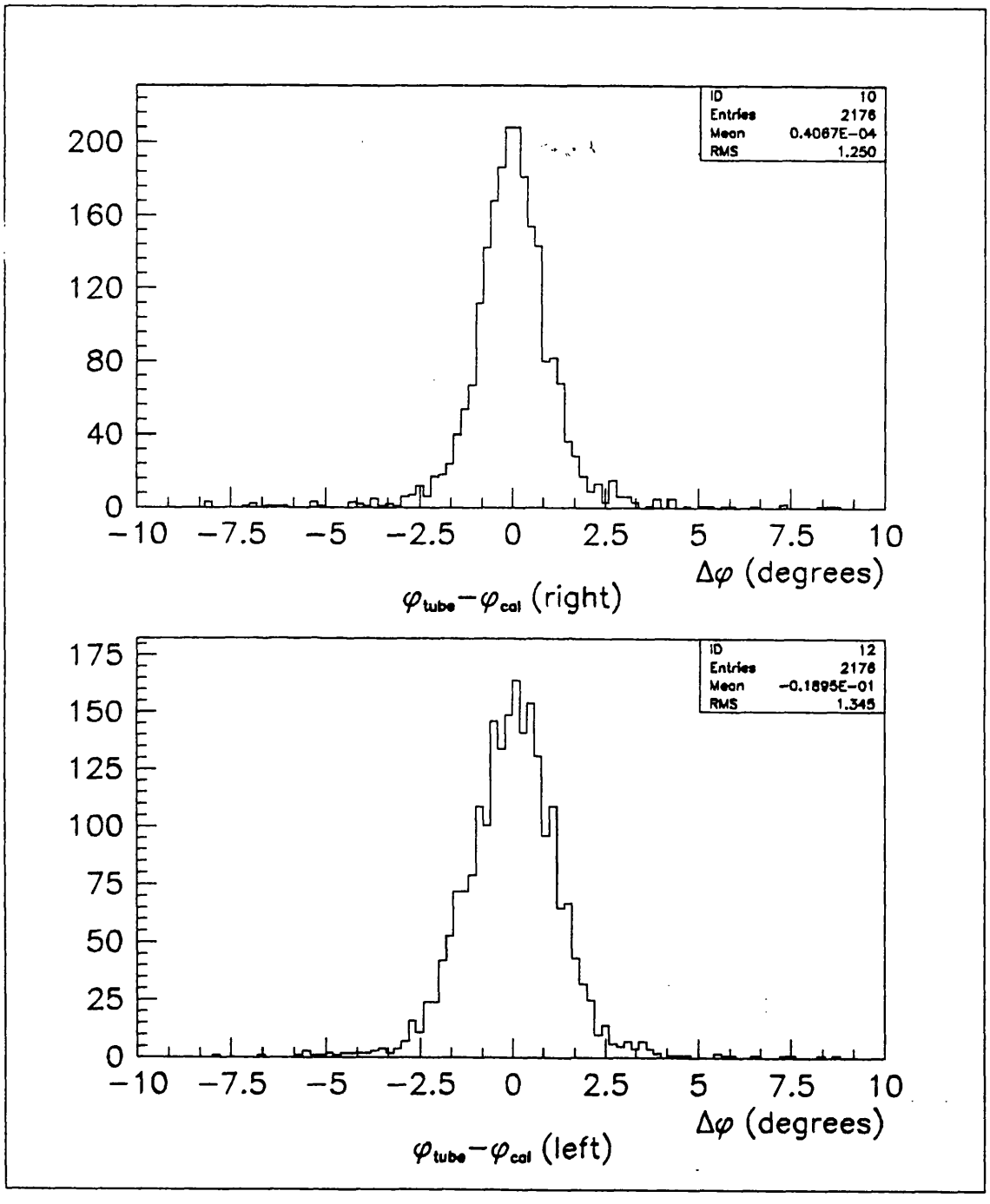

Figure 4.10: Distributions showing the difference in tube chamber and calorimeter ϕ measurement at each end for Bhabha events.

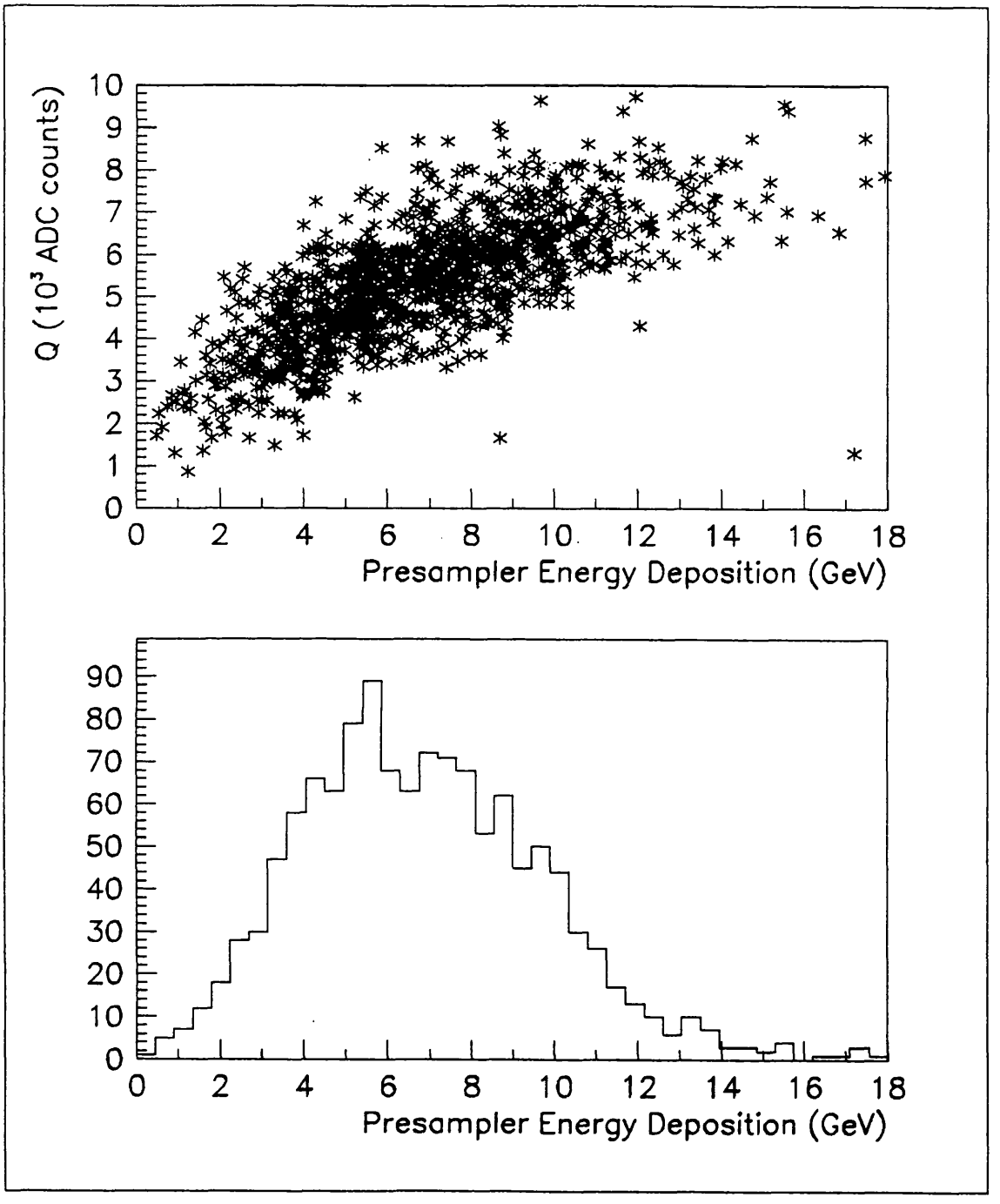

Figure 4.11: Scatterplot showing the correlation between presampler energy and tube chamber charge integral Q, and projection of the presampler energy distribution

Chapter 5

Luminosity Measurement at OPAL

5.1 Outline of the Luminosity Calculation in OPAL

The forward detector has in principle several components capable of making largely independent luminosity measurements. The first measurement to become available as LEP running began (used in the first OPAL publications [24],[25]) was a method based on defining the inner edge of the calorimeter by means of an energy cut, the energy measured by the calorimeter varying rapidly with the polar angle θ of the incident electron in the region of the inner edge, where showers become only partially contained. However, this method relies heavily on having an accurate Monte Carlo simulation of the detector and upstream material, and on a test beam calibration in 1988, and was thought to be limited to a systematic error of $\sim$ 4%. An absolute luminosity measurement with smaller and largely independent systematic errors was therefore developed using the tube chambers, which will be described in detail in section 5.2. An improved method of absolute luminosity determination was performed using the calorimeter, to act as a check on the tube chamber measurement. This will be described in section 5.3.

The tube chamber measurement, while having a low systematic error, had an unacceptably high statistical error when the data is divided into different

energy points, and in any case data from the tube chambers was not available for the whole running period. There are thus two components to the luminosity calculation for OPAL, exploiting the best features of different components of the forward detector. For the absolute luminosity determination, the forward tube chambers were used. As the majority of the statistics from the entire 1989 running period could be used, the limitation on accuracy comes from systematic errors rather than statistics.

For an accurate relative point to point determination, the requirement became one of consistent, background-free counting of Bhabha events with high statistical precision, for which the calorimeter was the more suitable instrument, having a higher cross section. The overall number of events counted by the calorimeter is normalized to the absolute luminosity for the period covered by the tube chambers; thus by the combination of the tube chamber and calorimeter data an accurate luminosity can be given for each energy point. The details of the point to point measurement and associated errors will be covered in section 5.4.

5.2 Method of Absolute Luminosity Determination using the Tube Chambers

The method used to determine a luminosity using the tube chambers was in principle simple; a fiducial area of acceptance for Bhabha events was defined within the tube chambers and events were selected on the basis of the tube chamber co-ordinates. The luminosity $\mathcal{L}$ is given by :-

$$\mathcal{L} = \frac{N_{event}}{\sigma_{tube} \times \epsilon_{tube}}.$$

There are thus three numbers to determine; N_{event}, the number of selected events, σ_{tube}, the tube chamber cross section, and ϵ_{tube} the efficiency for selecting events.

5.2.1 Bhabha Selection

The choice of fiducial area for Bhabha events was governed by the following factors.

- Mechanically and electrically, the tube chambers are divided into four quadrants, and because showers spread over several tubes, the shower centre must be some distance from the physical edge of the detector to achieve a good measurement.

- There is a beam pipe support ring of 2 X_0 with an outer surface at 47 mrad. This has arms extending out at 0°,90°,180° and 270°. It is desirable to avoid having this material upstream of the fiducial region.

The selection criteria applied are therefore :-

1. $(R_{left} + R_{right})/2 > 140$ mm
2. $(R_{left} + R_{right})/2 < 300$ mm
3. $(\phi_{left} + \phi^{proj}_{right})/2 > 10°$ away from quadrant boundaries at 0°,90°,180°,270°
4. $160° < (\phi_{left} - \phi_{right}) < 200°$.

R is the radial co-ordinate (i.e. distance from the beam pipe) of the incoming electron on the front face of the calorimeter. The cut at 140 mm is equivalent to a polar θ angle of $\sim$ 58 mrad. ϕ^{proj}_{right} is modulo$^{360}(\phi_{right} + 180)$ i.e. the projection of the right end position through the interaction point onto the left end. In the (rare) case that two clusters are found, the closest back to back pair in phi are selected. As good measurements are required at each end, only three of the four quadrants could be used, due to the two dead planes in one of the right end quadrants.

Cutting on quantities averaged between the two ends has two advantages; firstly one reduces the measurement errors by a factor $\sqrt{2}$, and secondly one is insensitive (to first order) to changes in the beam position. As the cross section changes rapidly with the polar angle θ, and variations of a few millimetres in the beam position are quite possible, this last point is extremely important.

In the scatterplot of the calorimeter energy E_{left} vs. E_{right} (fig 5.2) one can see a dense population of Bhabha events where the beam energy at measured in both ends, radiative tails where there is significantly loss of energy in one end,

and a small background from off-momentum events with $\sim$ 40% of the beam energy in both ends. The additional cut :-

$$(E_{left} + E_{right})/2 > 2/3 E_{beam}$$

is made to remove this background without cutting into the radiative tail of the signal. This last plot clearly illustrates the purity of the final sample. Notice that the number of events selected is highly insensitive to the position of this cut (only $\sim$ 2% change in number of events with a movement of 10 GeV in the cut). The dependance of this sample on the fine detail of the calorimeter calibration is minimal, as the energy resolution and absolute scale determination of the calorimeter are almost an order of magnitude better than required. The systematic errors on the tube chamber luminosity measurement are therefore truly independent of any measurement based on selecting an event sample with the calorimeter alone.

The few events that lie between the radiative tails (1%) but above the energy cut have been examined in detail. Some of these events were found to have showered in the beam pipe support ring in front of the forward detector, which is about 2 radiation lengths thick, between 40 and 47 mrad from the beam axis, and to have at least one particle scattering at higher angle into the tube chambers. This was demonstrated by using the calorimeter θ information (very accurate in this region) and the ratio of pre-sampler to main energy (high pre-sampler energy being a strong signal of early showering). Strictly speaking, these events are not background as they are genuine Bhabhas, but they are not Bhabhas that truly lie in the fiducial region and should not be in the final sample. To quantify the number of such events, correlations of the calorimeter θ and energy were made between the two ends. A class of event was found with a very low ($\sim$40 mrad) θ in at least one end and energies clustered near the cut. A minimum angle cut of 50 mrad on the calorimeter θ at each end to was used to distinguish mismeasured events from those with genuine low fluctuations in the calorimeter energy or double radiation. A 0.55% correction was applied, and a systematic error of the same magnitude assigned.

As a final check on the selected sample, the data were fitted with a $1/\theta^3$ distribution (fig 5.3) which is an approximate form of the theoretical differential cross section. The fit was performed over the θ range of the fiducial volume and gave a value of χ^2 of 0.81 per degree of freedom, and thus represents very good agreement.

5.2.2 Determination of the Tube Chamber Cross Section

The cross section for the geometric region defined above was determined using a Monte Carlo generator [26]. Events were generated over a large angular range between 35 mrad $< \theta <$ 170 mrad, for which a cross section is calculated by the program. (It is necessary to generate events over a much wider range of angles than the selection region because of the manner in which the generator treats radiation). The same selection criteria were applied to the monte carlo events as to the data and the cross section was given by the total cross section for the large range sample multiplied by the fraction selected, using a simplified simulation to reproduce the detector response. A 3 mm gaussian smearing was applied to the radial co-ordinate generated to simulate the tube chamber resolution. The generator produces a maximum of three particles (electron, positron and optional hard photon) and any two of these lying within the fiducial volume is sufficient for the event to be selected. To determine if the energy cut as satisfied, a nominal calorimeter inner edge acceptance of 40 mrad was used to determine which particles were inside the calorimeter and should therefore be used to calculate the energy that would be measured. In practice, few (<0.5%) Monte Carlo events were excluded by this cut. It was not considered necessary to use a full showering simulation of the detector as the acceptance region is in the part of the calorimeter that fully contains showers, and does not have large amounts of material upstream, and effects due to such material are negligible compared to the large statistical fluctuations in the degree of showering that occurs in the pre-sampler. The tube chamber position measurement is however insensitive to these fluctuations. The cross section calculated for the fiducial

volume, as defined by the cuts in section 5.2.1 is

$$\sigma_{tube} = 18.17nb,$$

at the peak of the Z° (excluding the dead quadrant from the calculation). The cross section was calculated individually for each energy point used in the Z° scan, with an interpolation being used for small deviations from the central value. The departure from a simple $1/s$ energy dependance was approximately 1%, which was interpreted as a measure of the Z° contribution to the calculation.

Several checks have been made of the validity of using a smeared generator for the cross section determination. The distribution of the measured energy in the calorimeter for selected tube chamber luminosity events with monte carlo superimposed is shown in Fig. 5.4. In this plot the monte carlo has a 3.1% energy smearing applied to simulated the detector response; however this does not change the fraction of monte carlo events selected as there are $< 0.2\%$ monte carlo events below the energy cut. The data agree well with the monte carlo; there is a slight excess in the region 30-35 GeV, but this is the region where the correction for mismeasured events was applied. As a further check, the calorimeter energy cut has been varied in size, and also the type of cut (average energy cut vs. minimum energy cut at each end) altered. In changing the energy cut by 10 GeV (in both data and monte carlo) the luminosity changes by $< 0.5\%$. Furthermore the calculated luminosity is insensitive at the same level to a 40 mm change in the radial cut. If the measurement was sensitive to material in front of the forward detector, and other precise details of the showering behaviour, then one would expect to observe strong variations in the calculated luminosity as a result of varying the above parameters.

5.2.3 Determination of the Efficiency for Detecting Tube Chamber Events.

There are two components to the efficiency; the efficiency for triggering and the efficiency of the detector for reconstructing clusters. The tube chambers do not generate a trigger and rely on the calorimeter trigger. As the tube chamber

acceptance is in the region where events are well contained, the trigger threshold of 12-15 GeV is well below the majority of the data. For a substantial part of the data taking only the main calorimeter was used in the trigger, and there is some inefficiency ($\sim 1.5\%$) due to events with a high fluctuation of energy deposited in the presampler. However this inefficiency can be quite precisely measured using the later data where the presampler was included in the trigger.

The efficiency of the tube chambers was measured on a fill by fill basis. The method used was to select a sample of events using the calorimeter position measurement that should lie within the tube chambers and find the fraction that were actually detected. The calorimeter selection was quite conservative in avoiding the edges of the tube chambers, though moving these cuts out towards the edges of the chambers did not greatly affect the efficiency. A second method was also used, using the position of a tube chamber cluster at one end to infer the existence of one at the other. The two methods agreed to within 0.2%. The efficiency for detecting Bhabha events was typically 98.5%. The inefficient events were correlated with a low presampler energy indicating late showering in the calorimeter and a small signal in the tube chambers.

5.2.4 Systematic Errors in the Measurement

The systematic errors in the measurement come from the following sources.

Theoretical Uncertainty In calculating the luminosity one relies on a theoretical knowledge of the cross section. The systematic error assumed for the generator cross section is 1%, and the statistical error on the sample generated is 0.2%.

Chamber Survey The absolute tube positions were surveyed to $\pm$ 1mm. As this error represents the largest systematic error in the analysis, several checks were made on the precision of the survey. If one examines distributions of $X_{left} + X_{right}$ and $Y_{left} + Y_{right}$ (standard cartesian co-ordinates), then for an ideally positioned detector and beam these distributions would have mean value zero. This is not the case; the overall mean X and Y

are displaced. If the detector were ideal, these displacements would correspond to a displacement of the beam from the nominal position. However if one makes a measurement quadrant by quadrant then one finds deviations in the beam position measured by different quadrants. It is assumed that these represent errors in the survey of the tube chambers The R.M.S. spread of these deviations is 1.5 mm; thus one assumes each quadrant is randomly mis-surveyed with a 1.5 mm error. Since one is taking the average of the two ends to make the crucial cut on the tube chamber inner edge, the error on the average radial measurement is 1 mm, which translates to a 1.5% error on the luminosity. An absolute luminosity was also determined separately from each quadrant, and these agreed to better than 1.3%, limited by statistics. The drift chambers (see Appendix B) situated in front of the calorimeter were operational for part of the data taking and these were also able to make a position measurement of incident electrons on the calorimeter. This agreed with the tube chamber measurement to 1 ± 1 mm, again the precision of the comparison being limited by statistics.

Tube Chamber Efficiency The error assumed is the variation in efficiency upon movement of the calorimeter spatial cuts (see section 5.2.3). The selection of events with the calorimeter was varied in radius and azimuth and found to show a 0.5% variation.

Trigger Efficiency As mentioned in section 5.2.3 there was a 1.5% trigger inefficiency in part of the data from using a trigger based on the main calorimeter only. The error on this number is purely the statistical error of 0.3% from the number of events from the second data taking period (when the new trigger was in operation) which would have not fired the old trigger.

Event Subtraction An error of 0.5% is assigned to the 0.55% correction for mis-measured events, based on the uncertainties in classifying these events using the calorimeter information.

Energy Cut Varying the energy cut over a 10 GeV range in the data and the monte carlo events alters the calculated luminosity with an R.M.S.

Source of error	Magnitude
Theory	1%(sys)
	0.2%(stat)
Survey	1.5%
Efficiency	0.5%
Trigger	0.3%
Energy Cut	0.5%
Event subtraction	0.5%
Radial Cut	0.5%
Overall error	2.1%
(in quadrature)	

Table 5.1: Table sumarising contributions to the systematic error on the tube chamber luminosity

deviation of 0.5%. Moving this cut varies the fraction of the radiative tail included in the sample, and thus serves as measure of how well the Monte Carlo describe the data. One would expect any background to be peaked at lower energy, so if the final data sample did include background one might reveal it by varying this cut.

Radial Cut Varying the radial cut from 140 mm to 180 mm in the data and monte carlo events alters the luminosity with an R.M.S. deviation of 0.5%. This variation might reveal a number of effects that could influence the measurement. By changing the inner edge cut one is using different channels to define the inner edge and so effects due to gain variations could be seen. Furthermore if the data were affected by material upstream (not described in the monte carlo simulation) one might expect some level of variation in the luminosity with radial cut. Any severe variation in efficiency with radius would also be revealed.

Adding these errors in quadrature an overall systematic error of 2.1% is obtained. The statistical error for the whole running period for which tube chamber

data is available is 0.65%. Thus the overall error on the total integrated luminosity for the period is 2.2%. The errors are summarised in table 5.1.

5.3 Absolute Luminosity Determination Using the Calorimeter

An independent method to measure the absolute luminosity was developed by M.Jimack using the calorimeter alone. It relies on identifying the shadow projected by the beam pipe support ring on to the front face of the calorimeter. This support ring is a precisely machined Al ring with a conical outer surface of pointing geometry at a polar angle of 47 mrad and a thickness of $2X_0$, situated 50cm in front of the forward calorimeter. Since a typical electromagnetic shower is developing rapidly as it enters the main calorimeter, the addition of an another $2X_0$ of material significantly alters the pre/main energy sharing.

To ensure a background-free sample for the support ring analysis, a total energy of at least 25 GeV is required in each calorimeter and the two energy clusters are required to be back-to-back to within 20° in azimuth. To avoid complications from the four webs which fix the support ring in place, the average azimuth of the event is required to be more than 15° away from the vertical or horizontal. In addition to excluding the quadrant containing the bad calorimeter segment, the opposite segment was also excluded in order to create a symmetrical acceptance which cancels to first order the effects of shifts in the position of the interaction region, and of shifts in the relative position of the calorimeter w.r.t. the support ring.

Fig 5.5 shows a scatterplot of the main calorimeter energy vs. the polar angle, θ, of the electron as measured in the calorimeter for such events, for both data and Monte Carlo events (with detector simulation). (The agreement of the phi distribution between data and MC is at the level of 1%.) The abrupt shift to higher main energy at the outer edge of the beam support ring is clearly visible in both plots. At higher angles, the main energy is almost independent of θ since there is little material between the forward detector and the interaction

point in this higher angular range. The support ring shadow was used to make an independent segment to segment polar angle calibration in the angular range of the support ring. This is desirable firstly to be independent of any survey information, and secondly because the calorimeter polar angle has a complicated parameterization with associated uncertainties. The angular calibration was performed as follows. The mean energy in the main calorimeter in an angular region 45.5 mr$< \theta <$49.5 mr, a narrow band containing the edge of the support ring shadow, was found for each segment It was seen (by looking at the individual segment distributions in detail) that shifts in the apparent θ position of the support ring shadow from segment to segment were proportional to shifts in these mean energies. Thus, correction shifts to the θ distributions were extracted for each segment. The distributions of mean energy (in the main calorimeter) as a function of segment (azimuth) are shown separately for the two ends of the detector in fig 5.6. A clear sine tendency is seen for the left hand end - while a fairly random behaviour is seen in the right hand end. The amplitude of the sine wave (about 1 mr) is consistent with what could be expected from a shift of the calorimeter w.r.t. the support ring. The θ shifts were applied relative to the Monte Carlo value - taking into account a global main calorimeter energy difference of 0.7 GeV between Monte Carlo and data. This gives an angular calibration fixed to the support ring shadow, and independent of survey. However, due to the imperfect simulation of the detector in the Monte Carlo, a (conservative) systematic error of 1 mr was assigned to this calibration. The application of the calibration changed the final luminosity by only 1%. (Applying the same method to the Monte Carlo segments made no significant change in the luminosity.)

The diagonal line in fig. 5.5 is used as a cut to separate between the events traversing the ring and those missing it. Performing a rotation in the energy-angle plane, we define the variable

$$f = E + R \times 0.5[GeV/mm]$$

which runs perpendicular to this line. Here R is the radial position of the cluster - equal to θ/2408mm. The line corresponds to a value of f = 92 GeV.

To select the luminosity sample, the cut is made on the average f of both sides. This reduces sensitivity to z displacements, bunch length and other variations in beam parameters. An alternative method is to cut in f only on one side, and then only on the other. The two numbers should then be averaged and compared with Monte Carlo. This method disagrees with the other by 1%. The average of the two methods was taken and a 1% systematic error assigned.

Fig. 5.7 shows the distribution in average f of events passing all cuts except the cut in f. The shape of the superposed monte carlo full detector simulation agrees quite well with the data. Disagreement at lower values of f may be due to the difficulty of reproducing the details of the complicated bellows and flanges which lie inside the support ring, and of simulating the correct response of the calorimeter at its edge. The position of the minimum in the f distribution at f = 92 GeV occurs at the very edge of the support ring, where the rate of change in the pre/main sharing is maximum. Placing the cut here minimizes the influence of many systematic effects. The f cut defines the inner radius of acceptance whilst the outer radius is defined by the detector acceptance. To check that the outer edge was simulated correctly by the Monte Carlo, the outer edge was defined by the tube chambers at a radius of 300 mm. After correcting for tube inefficiency, the result agreed to 0.05 %.

The number of events selected by these cuts is slightly less than for the tube selection - thus this method is not suitable for a point to point luminosity calculation, but is instead suitable for a check on the absolute luminosity. In those fills for which the tubes had a good efficiency, the integrated luminosity is lower in the support ring method by 0.8 %. The estimated systematic error on the support ring measurement is 2.6 % for this comparison. This includes the "intrinsic" error plus the binomial error on the number of events accepted by one method and not the other. It does not include the theoretical error, which is assumed to be the same for the two methods. A detailed evaluation of the errors is given in Table 5.2. The equivalent "intrinsic error" (neglecting theoretical and statistical errors) on the tube chamber measurement is 1.9%, so the two methods are in excellent agreement.

Source of error	Magnitude
M/C statistics	1.8%
Average f vs. f cut each end	1.0%
ϕ distribution	1.0%
Energy Cut(includes background)	0.6%
θ shift uncertainty of 1 mrad	0.6%
Position of outside edge	0.3%
Trigger Efficiency	0.2%
3 mm Calorimeter shift (xy)	0.15%
Y beam shift of 2mm	0.15%
Binom. stat. error of data sample	0.6%
Overall error (in quadrature)	2.6%

Table 5.2: Table sumarising contributions to the systematic error on the support ring method luminosity. To allow a direct comparison with the tube chamber luminosity, the (correlated) theoretical error is not included

5.4 Point to Point Luminosity Measurement

5.4.1 Event Selection

Valid luminosity events were defined by requiring that the average energy seen in the main section of both calorimeters exceed 70% of the beam energy, and that the azimuth of the calorimeter energy clusters at each end be back-to-back within 20°. The main energy (as opposed to the total energy) was used for two reasons. Firstly, for part of the data taking only the main calorimeter was used in the trigger, and so a cut in the the main energy avoids problems of trigger efficiency. Secondly, it is more straightforward to maintain the calibration of the main calorimeter alone, having only 32 constants as opposed to 48 if the pre-sampler were included. The cut at 70% of the beam energy, which corresponds to 83% of the expected main energy, is three standard deviations of the energy resolution below the peak. It was chosen so as to minimise the dependance of the luminosity on the calibration stability of the calorimeter (fig 5.9). Fig. 5.8 shows the acoplanarity distribution of events passing the energy cut. It can be seen that the width of the distribution corresponds to the expected detector resolution, and that background contributes less than 0.1% of the overall sample.

5.4.2 Determination of Integrated Luminosity for Energy Points

The luminosity derived from the calorimeter using the selection criteria listed above was normalized to the tube chamber luminosity over the whole period of data taking for which tube chamber data was available (approximately 75% of the total running period). The cross section for the simple calorimeter luminosity selection was found to be 41.4±0.9 nb at the Z° peak. The normalized calorimeter measurement was then used to give an absolute integrated luminosity for each energy point which was used to calculate the multi-hadronic and the leptonic cross sections. The final systematic error of 2.2% for the absolute luminosity at each energy point is calculated by adding in quadrature the tube chamber systematic error and statistical error for the whole data taking period. Cross

sections for each energy point were calculated assuming a simple $1/s$ energy dependance, and the validity of the assumption was checked with the Monte Carlo generator.

5.4.3 Point to Point Systematic Errors

Fig. 5.9 shows the spectrum of the average main calorimeter energy normalized to the beam energy for events passing the azimuthal cut. The 70% energy requirement is high enough to be background-free, yet low enough to accept all well contained Bhabha events. It rejects events only partially contained due to strong radiation or leakage at the edges of the calorimeter. The distributions from all the individual fills have been examined, and none was found to contain more than 0.5% background. Since energy calibration of the calorimeter could be maintained to within 0.5% over the period of data taking, the cross section for luminosity events defined by these simple requirements was stable over time to $\pm$ 0.8%. As half the accepted events were within 60 mrad of the beam axis, the measurement is almost entirely independent of Z° interference (0.3% max). Because the energy cut was imposed on the average of the main energy in the two calorimeters, and in the region of the calorimeter inner edge measured energy is an approximately linear function of polar angle θ, the acceptance was free of first-order dependence on beam displacements and the size of the beam intersection region. Thus all measurable point to point systematics added in quadrature are $< 1\%$. The overall point to point systematic error assumed is 1% as it is not possible to observe smaller effects with the statistics of the present data sample. The luminosity given from the above method was compared with the luminosities from the tube chamber (fig 5.10) and calorimeter/support ring methods and no statistically significant trend was observable. This last check in itself gives a 2% upper bound on the point to point systematic error.

The point to point luminosity error is assumed to be random. It arises mainly from fluctuations in the calorimeter energy calibration with time, and during the scan of the Z°, the LEP fills of a particular beam energy were evenly spread throughout the three month running period. Calibrations were performed several

times over the running period, but each energy point takes fills corresponding to several calibrations, averaging out fluctuations.

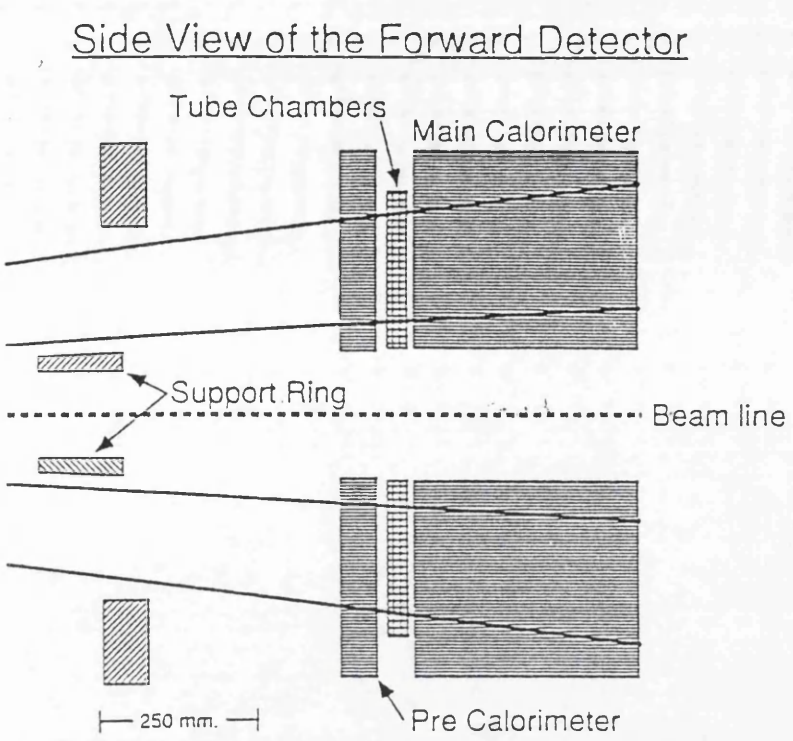

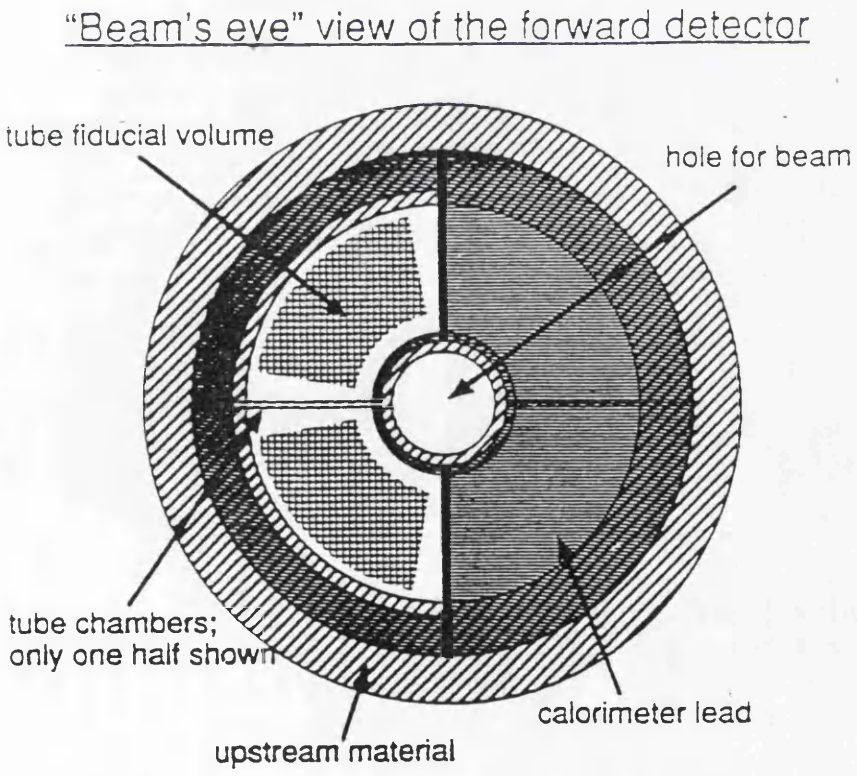

Figure 5.1: Schematic diagram of the parts of the forward detector used in the luminosity analysis

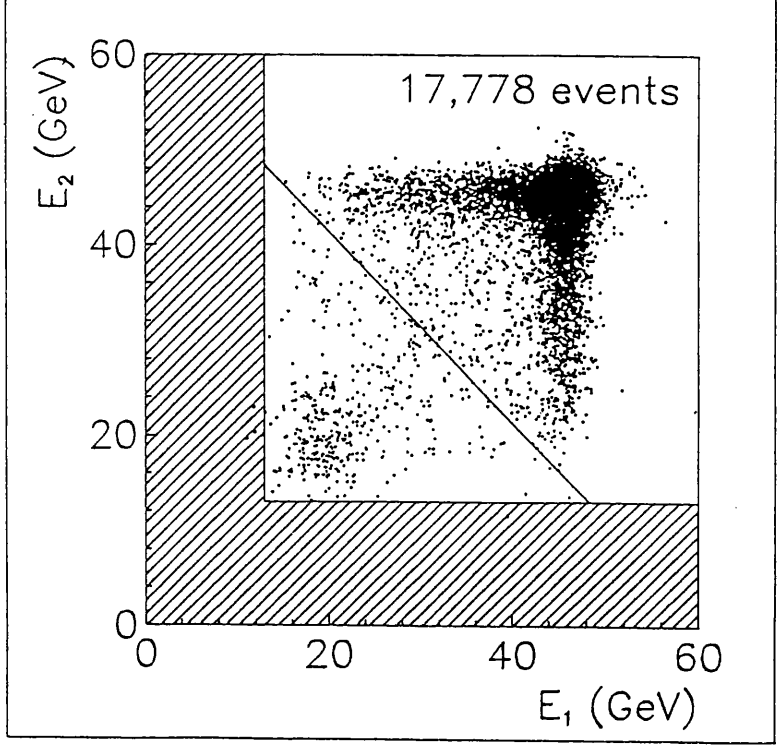

Figure 5.2: Scatterplot showing right vs. left calorimeter energy for events satisfying tube chamber spatial cuts. The energy cut is shown; shaded area represents region where the trigger excludes events.

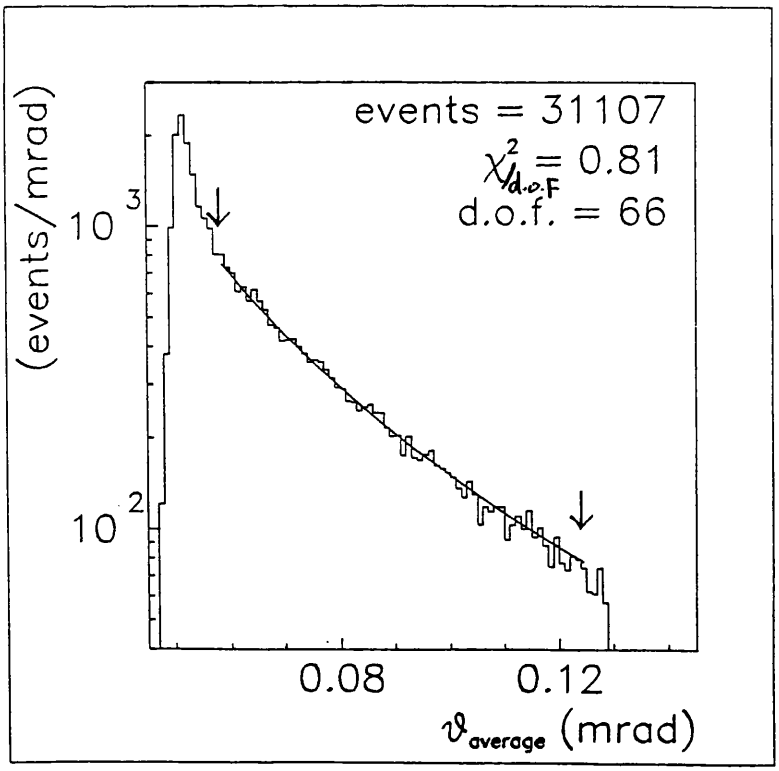

Figure 5.3: Distribution of tube chamber luminosity events in θ with a $1/\theta^3$ fit

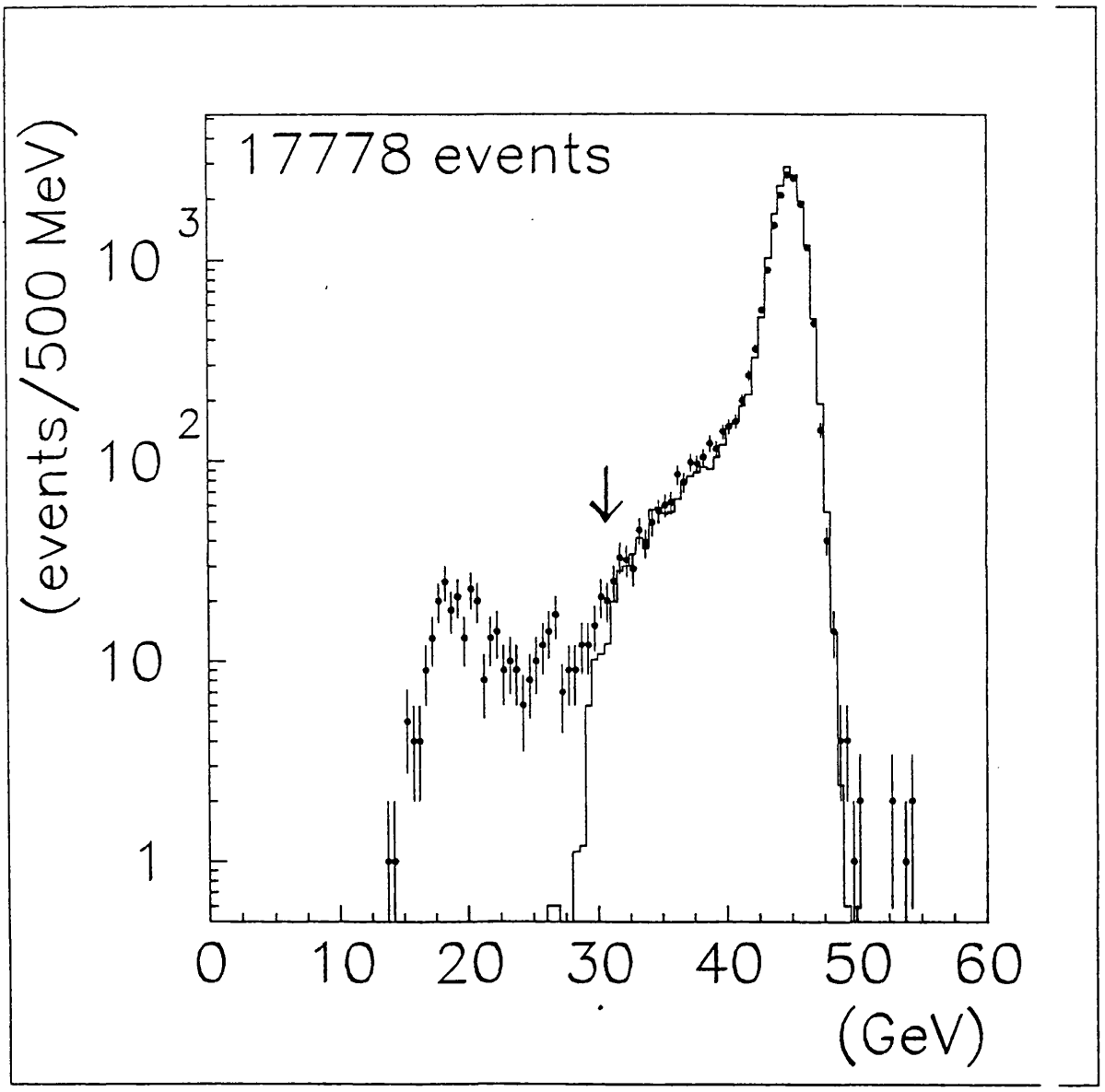

Figure 5.4: Distribution of tube chamber events (crosses) in average calorimeter energy with monte carlo data (solid line) superimposed

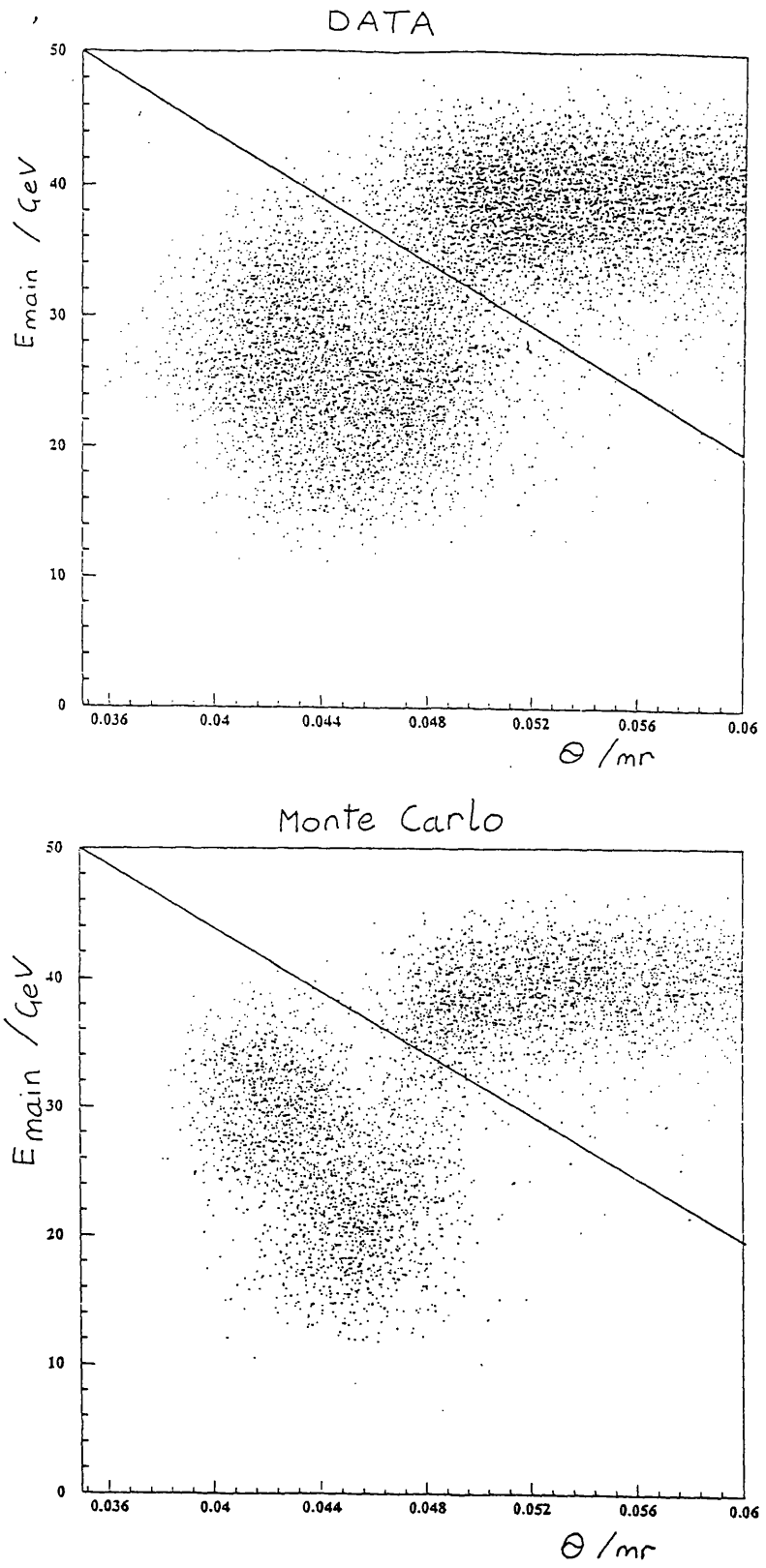

Figure 5.5: Scatterplot of main calorimeter energy vs. θ for data and monte carlo showing applied cut

45.5 mr < θ < 49.5 mr

Right end

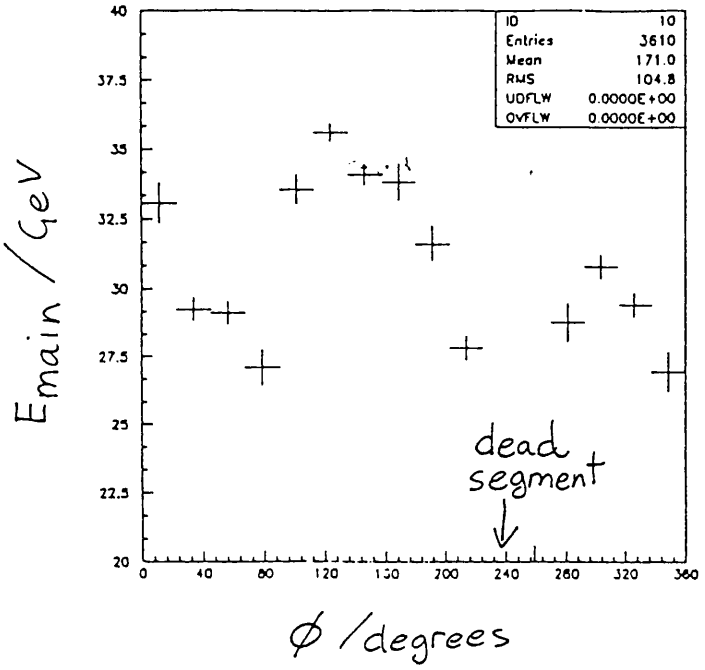

Left end

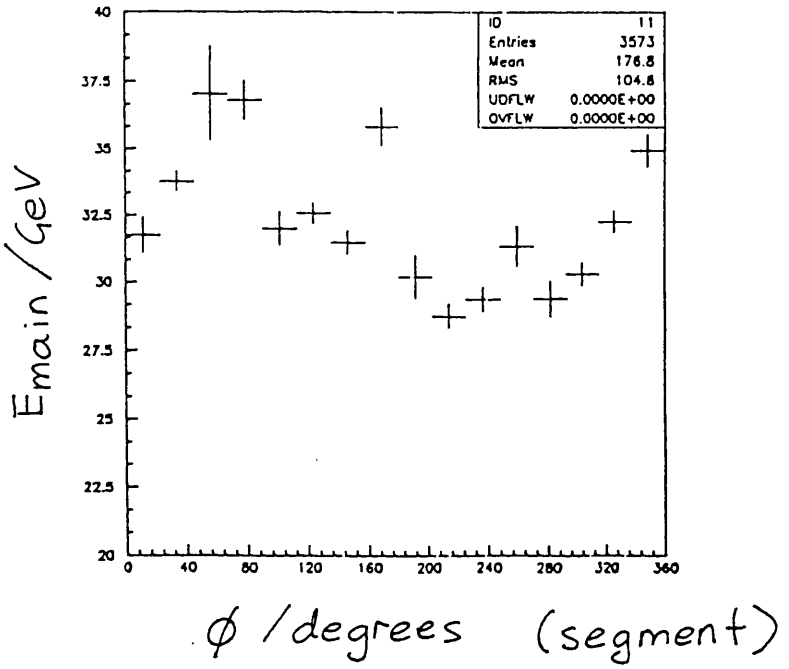

Figure 5.6: Average main energy in each segment for events in the region 45.5 mrad $< \theta <$ 49.5 mrad

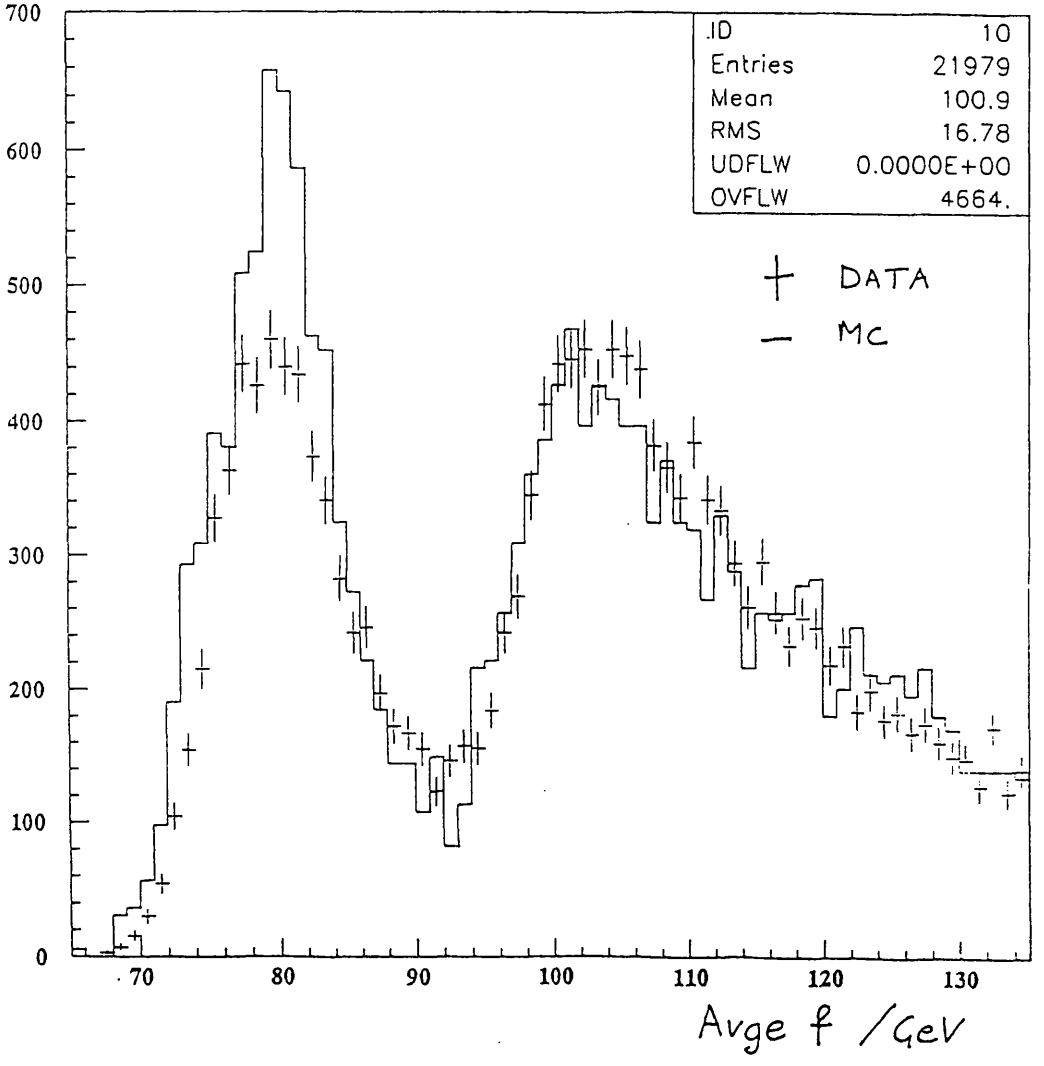

Figure 5.7: Average (between ends) f distribution for data and Monte Carlo used in calorimeter absolute luminosity determination

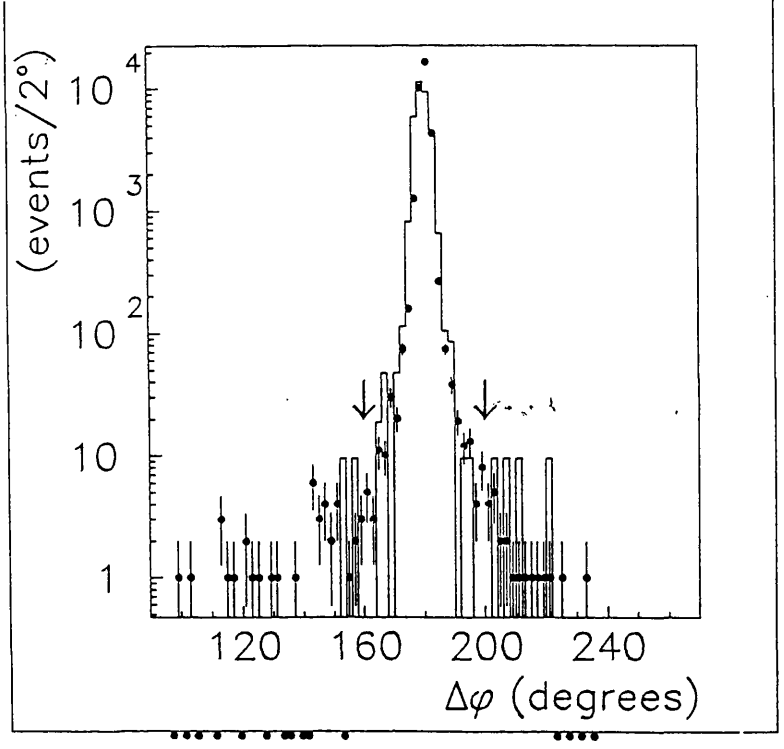

Figure 5.8: Acoplanarity of data (crosses) and Monte Carlo (solid line) for events selected for point to point luminosity determination.

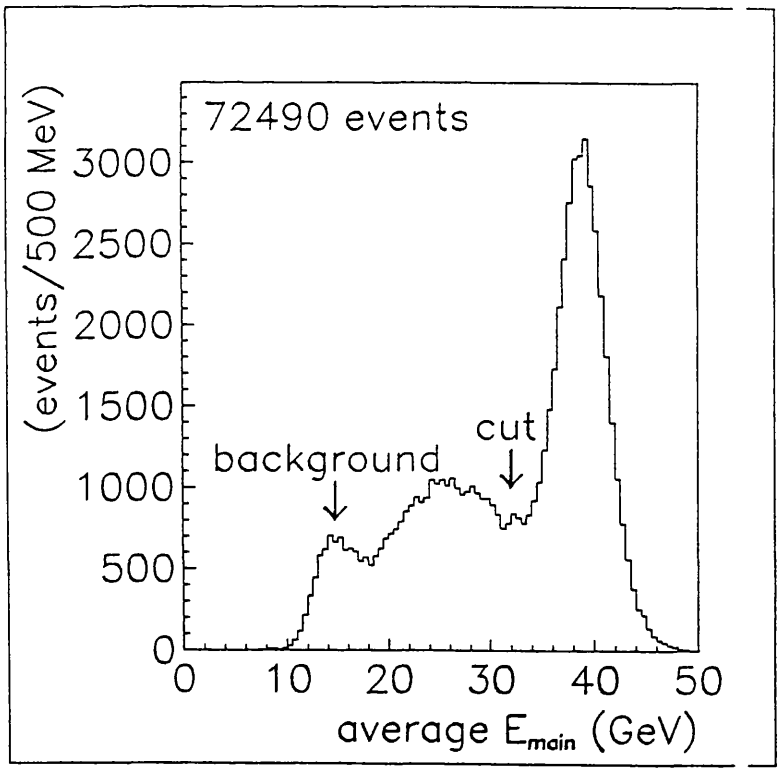

Figure 5.9: Distribution of main calorimeter energy for events selected for point to point luminosity determination.

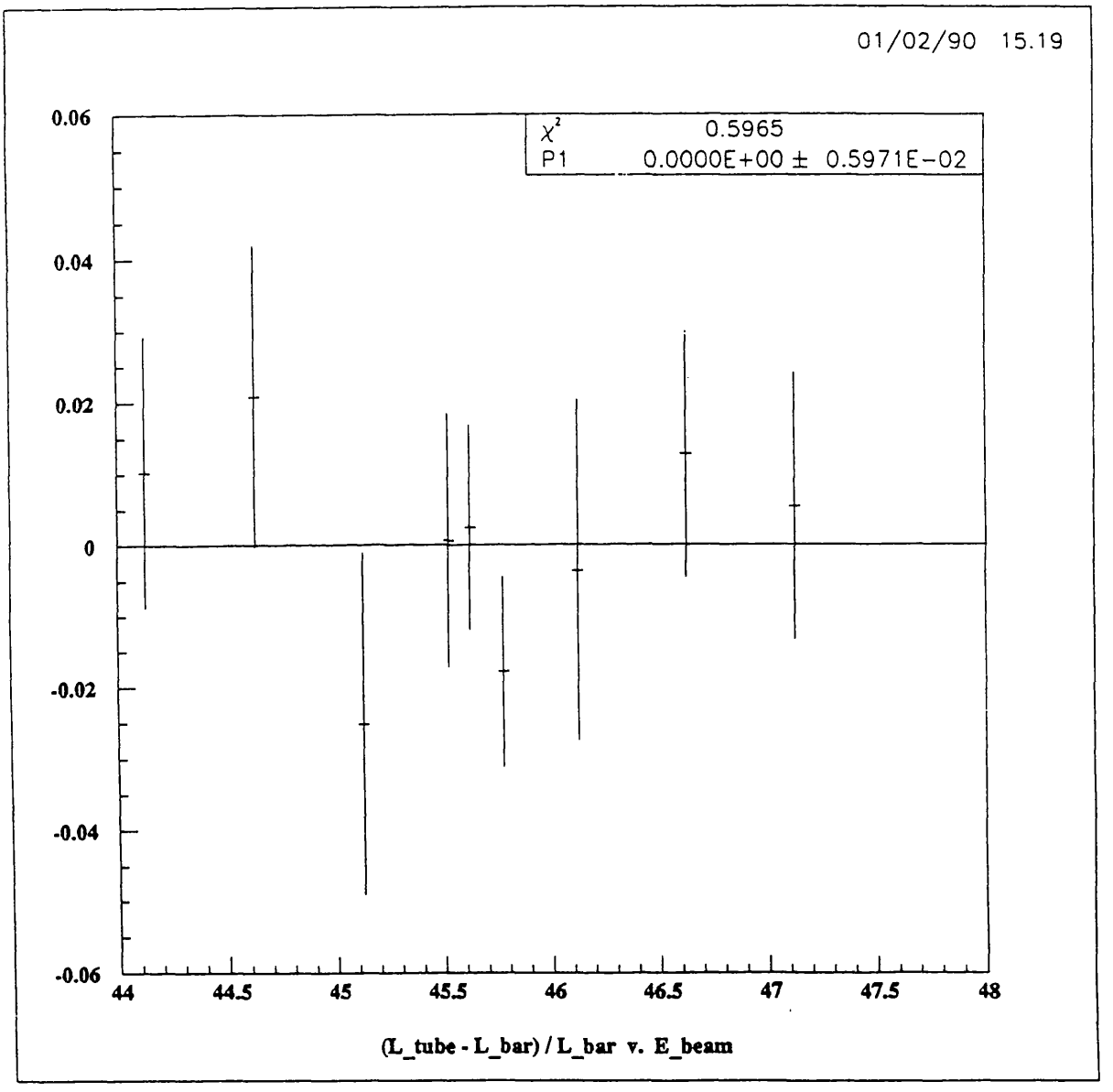

Figure 5.10: Difference between tube chamber and calorimeter (point to point) luminosity measurement as a function of beam energy. Errors represent statistical binomial error of two samples.

Chapter 6

The Hadronic Decays of the Z°

Hadronic events leave a clear signature in the OPAL detector: a typical event has ~10-30 charged tracks in the central detector, and up to 50 clusters in the electromagnetic calorimetry. In addition, charged tracks in the barrel region will produce hits in the time of flight counters. Thus hadronic events can be both triggered and selected with a high degree of redundancy. A typical hadronic event as displayed by the OPAL graphics package is shown in fig 6.1. The author did not take a direct part in this analysis.

6.1 Hadronic Event Selection

The hadronic event selection was mainly based on the energy of clusters in the lead-glass electromagnetic calorimetry (the forward calorimeter is not included in the analysis). A cluster is formed by requiring one block to be >60 MeV above pedestal, looping over nearby blocks, and including those in the cluster that are >40 MeV above pedestal. A maximum of 9 blocks can contribute to a cluster. Cluster algorithms have been developed to deal with the case of overlapping clusters in a way that avoids double counting of block energies. For a cluster to be included in the event selection cuts, a threshold of 100 MeV was applied to clusters in the barrel region. In the end cap region a cluster threshold of 200 MeV was applied, with the additional requirement that the end cap cluster was composed of at least two adjacent lead glass blocks contributing to the

energy sum. The last requirement was imposed to avoid counting noisy blocks as clusters.

To select a hadronic candidate, the following requirements were made on the above threshold clusters :-

1. Number of clusters, $N_{clus} > 8$,

2. A total energy deposited in the lead glass of at least 10% of the beam energy, i.e.

$$R_{vis} = \frac{\Sigma E_{clus}}{\sqrt{s}} > 0.1$$

where E_{clus} is the energy of each cluster,

3. The energy imbalance along the beam direction, R_{bal}, satisfies the condition

$$R_{bal} = \frac{|\Sigma(E_{clus} \times cos\theta)|}{\Sigma E_{clus}} < 0.65.$$

The cut on the number of clusters is imposed to remove Z° decays into e^+e^-, $\mu^+\mu^-$ and $\tau^+\tau^-$, the first two of these being characterised by typically having only two electromagnetic clusters, and the τ decays by a low cluster multiplicity. The distribution of N_{clus} is shown in fig. 6.2, with Monte Carlo simulation of hadronic events (see section 6.4) superimposed. Good agreement is seen between the Monte Carlo and data in the region included in the hadronic sample; the sharp peak at low cluster multiplicities is due to lepton pair production.

The visible energy cut is imposed to remove two photon events and beam gas events, which can have a large number of clusters and so pass cut 1, but are characterised by low visible energy. The visible energy distribution is shown in fig 6.3, with Monte Carlo simulation imposed. The energy balance cut is imposed to reject beam-wall, beam-gas and beam-halo events, and cosmic rays in the end caps, where a significant energy imbalance can be expected. The distribution of R_{bal} is shown in fig. 6.4. To demonstrate the effect of these cuts in a more visual way, fig 6.5 contains scatterplots of N_{clus} against R_{vis}, and R_{bal} against R_{vis} with the cuts shown as dashed lines.

The time of flight counters (TOF) and central detector were used to veto cosmic rays in the barrel region as follows :-

- All events with hits timed within 8 ns of the beam crossing in at least 4 TOF counters were accepted
- Events with less than 4 TOF counters firing within 8 ns for which $> 50\%$ of the measured energy was in the barrel lead glass were rejected.
- All events remaining unclassified after this selection were visually scanned.
- All events which were taken while the central detector was at full voltage but which had no central detector tracks with good primary vertices (less than 70cm in z-direction and 2cm in radial direction from OPAL centre) were also scanned

In total $\sim$2% of the hadronic event sample was scanned. From this sample 36 events were rejected, 20 being classified as cosmic rays, 2 as beam wall events and 12 as beam-halo events. In this scan, use was made of the tracking information of the central detector to identify misplaced primary vertices. After all the above cuts had been applied, a sample of 25,801 hadronic Z° decays remained, corresponding to an integrated luminosity of 1.25 pb^{-1}.

6.2 Trigger Efficiency

There were four principal independent triggers for the hadronic decays; the TOF, track trigger(TT), electromagnetic endcap calorimeter(EE), and electromagnetic barrel calorimeter(EB), although these triggers do not all overlap in all ranges of θ. In the barrel region the TOF, EB and TT triggers overlap and have constant efficiency as a function of θ. By studying the events failing one or more of these triggers, the three triggers were found to be independent, and individually to have an efficiencies of 99.97$\pm$0.013%, 99.35$\pm$0.064% and 90.57$\pm$0.023% respectively. The overall trigger inefficiency was therefore less than 0.01% in the barrel region. In the end cap region the trigger efficiencies were calculated as a function of θ_T[1], as the trigger efficiency is not expected to be constant in this region. The triggers available were the the EE, TT and TOF. The TT loses efficiency as

[1] $cos\theta_T$ is the angle of the thrust axis to the beam direction

$\cos\theta_T$ approaches 1, and the TOF trigger is set only when the event contain particles which pass through the TOF, although the thrust axis is in the endcap region. However, even in the lowest angular range ($0.96 < cos\theta_T < 1.00$) where the greatest inefficiency could be expected, due to increased material in front of the electromagnetic calorimeter, and limited cover from other triggers, the trigger efficiency was found to be $99.72 \pm 0.06\%$.

By integrating the efficiency over θ the overall trigger inefficiency was estimated to be much less than 0.1%, and therefore negligible.

6.3 Background Estimation

6.3.1 $\tau^+\tau^-$ Events

The main background in the hadronic data sample arose from $\tau^+\tau^-$ events. A quantitative estimate of the size of this contamination was obtained using Monte Carlo events generated with the KORALZ generator [27] run through the full detector simulation program GOPAL [28]. GOPAL includes a representation of the detector geometry and material as well as detector resolutions and efficiencies, and uses the GEANT [29] package for simulating the tracking of particles. A sample of $\tau^+\tau^-$ events corresponding to the same integrated luminosity as hadronic decays was generated, and after detector simulation, passed through the same reconstruction program as the real data, and the selection cuts for hadronic decays were applied. By this method a background fraction of $0.33 \pm 0.04\%$ was estimated. This fraction was statistically subtracted, and the error included in the systematic error. A second method of calculating this background was performed using the data. In general, $\tau^+\tau^-$ events have a charged track multiplicity <5. All events with less than 5 tracks were visually scanned, and the fraction of $\tau^+\tau^-$ events identified was consistent with the Monte Carlo estimate.

6.3.2 Two Photon Events

A second source of possible background was two photon events. A Monte Carlo calculation using a quark parton model was used to estimate the number of

events corresponding to the integrated luminosity of the hadronic decay sample that would have passed the hadronic selection cuts. As two photon events are an essentially QED process, their rate is approximately constant over the Z° resonance. Thus a second method of estimating this background, this time using the data, is to compare the ratio of events with low visible energy to those with high visible energy as a function of the beam energy. The two methods gave consistent results, and the estimated size of the background is 0.03±0.03% on the peak of the Z°, and 0.2±0.2 in the tail region.

6.3.3 Other Backgrounds

From the visual scan of events with less than four TOF counters hit, the remaining cosmic ray and beam related background was estimated to be less than 0.1%. A further check was on cosmic ray background was performed by taking data with no beam circulating in LEP, and passing the data through the hadronic selection program. The cosmic ray rate predicted was 1-4 every 100 hours of data taking, which is consistent with the 20 cosmic rays identified in the scan.

A sample of 3700 e^+e^- (wide angle Bhabha scattering) Monte Carlo events was passed through the detector simulation and hadronic selection. None of them passed the selection cuts, and this background is estimated to be less than 0.1% and therefore negligible.

6.4 Acceptance Calculation

Due to the complicated nature of the hadronic decays, it was necessary to use the GOPAL detector simulation to calculate the detector acceptance. Hadronic events were generated using the JETSET parton shower model with five flavours and string fragmentation [30], and tracked through the detector simulation. After running the same reconstruction program that was used on the data, the hadronic event selection was applied. An acceptance of 97.9% of the generated sample was calculated, with negligible statistical error. Good agreement between the simulated and real data is demonstrated by the similarity of the

distributions of figs. 6.2,6.3,6.4. Further evidence that the hadronic event generator and detector simulation offer a realistic representation of the data is given in [31], where a comparison is made of jet shape variables such as thrust and sphericity between the data and Monte Carlo. To estimate the uncertainty in the acceptance arising from the details of the generator, the parameters of the JETSET were varied, and an alternative hadronisation package, HERWIG [32], was used. An estimated 0.5% acceptance uncertainty arose from this source. A further source of systematic uncertainty arises from imperfections in the detector simulation; in particular certain (small) regions in θ were found to show discrepancies between data and Monte Carlo in the visible energy detected. This is attributed to missing material in the simulation of the structure of OPAL. If extra material is added arbitrarily to compensate for these discrepancies, a 0.5% change in the acceptance is observed, and this is assigned as a systematic error. When calculated at centre of mass energies ± 4 GeV of the peak, the acceptance changed by -0.23$\pm$0.26% and 0.17$\pm$0.23% respectively (errors on these numbers are statistical). A systematic error of 0.2% was assigned to account for this.

An error due to the specific choice of cuts for hadronic selection of 0.17% was estimated by varying the cuts over a range comparable to the resolution in these variables. In addition, in the distribution of R_{vis}, a significant discrepancy between Monte Carlo and data can be seen, which is thought to arise from an improper simulation of hadronic interactions in the lead glass. The difference corresponds to a 5.3% error in the energy scale, and if the Monte Carlo (or data) are "tuned" to compensate this effect, then the acceptance changes by 0.09%. Combining these two effects, a total error of 0.2% arises from the hadronic selection cuts.

6.5 Summary of Results

Hadronic events were selected with an overall efficiency of 97.9%, with the only significant background being from $\tau^+\tau^-$ decays. These were statistically subtracted; all other backgrounds were removed on an event by event basis by scanning. The errors from all sources of uncertainty in acceptance and background

Source of error	Magnitude
Acceptance(MC)	0.5%
Acceptance(frag.)	0.5%
Acceptance(E dep. etc)	0.2%
Selection Cuts	0.2%
Trigger Efficiency	$< 0.1\%$
Backgrounds	$< 0.1\%$
Overall error (in quadrature)	0.8%

Table 6.1: Table summarising contributions to the systematic error on the hadronic event selection and acceptance determination

estimation, when summed in quadrature, give an overall systematic error in the hadronic cross section of 0.8%. The sources of error are summarised in table 6.1. This error is considered to be an overall normalization error which has a size and magnitude independent of energy.

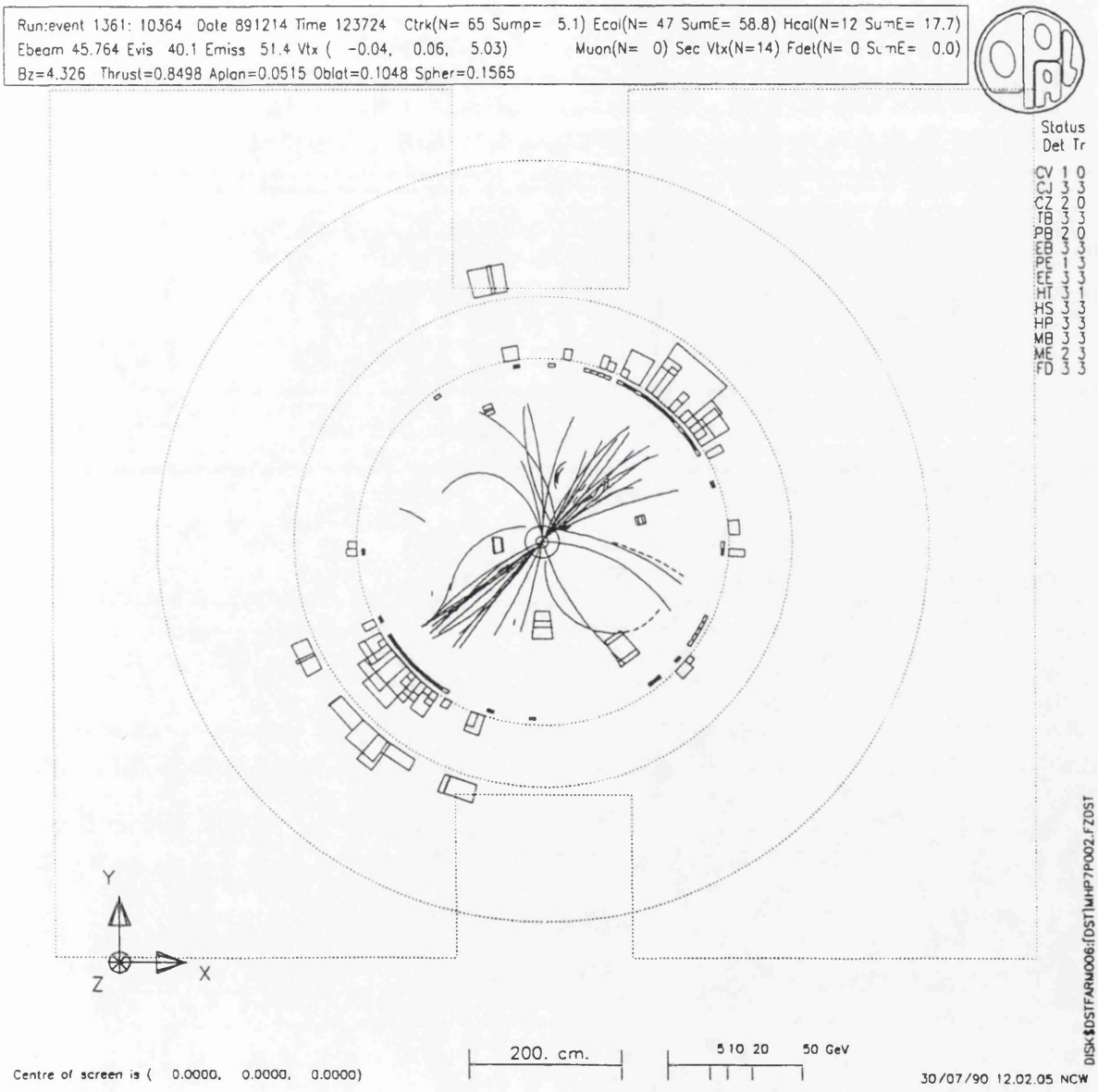

Figure 6.1: A typical hadronic event as displayed by the OPAL graphics package. Tracks in the central detector and clusters in the calorimetry are shown.

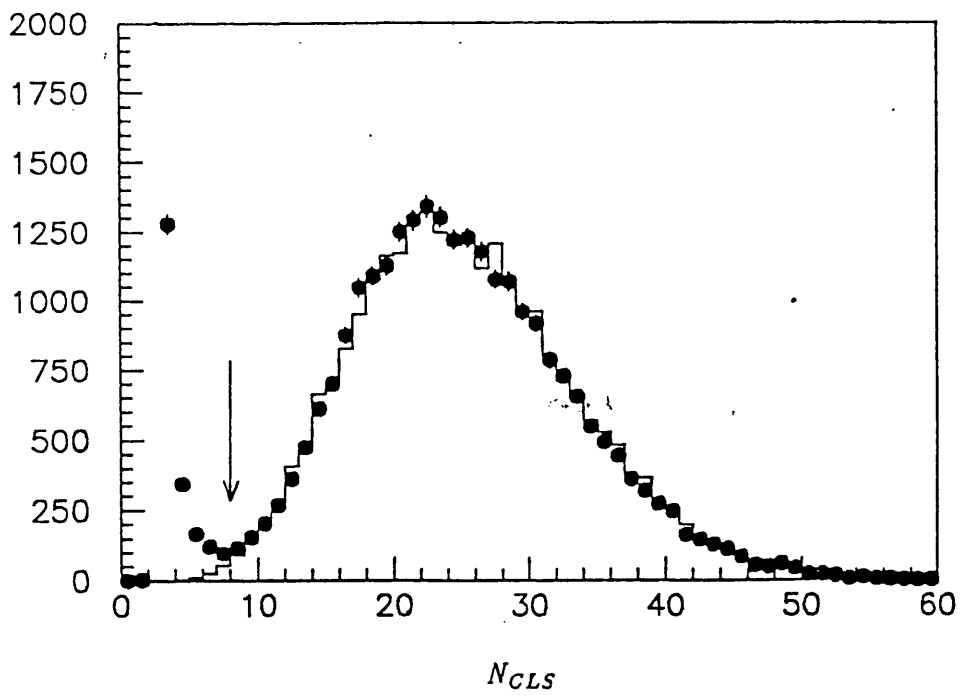

Figure 6.2: Measured distribution of N_{clus} for hadronic event sample with all other cuts imposed (data points). Also shown is Monte Carlo prediction using QCD parton shower model

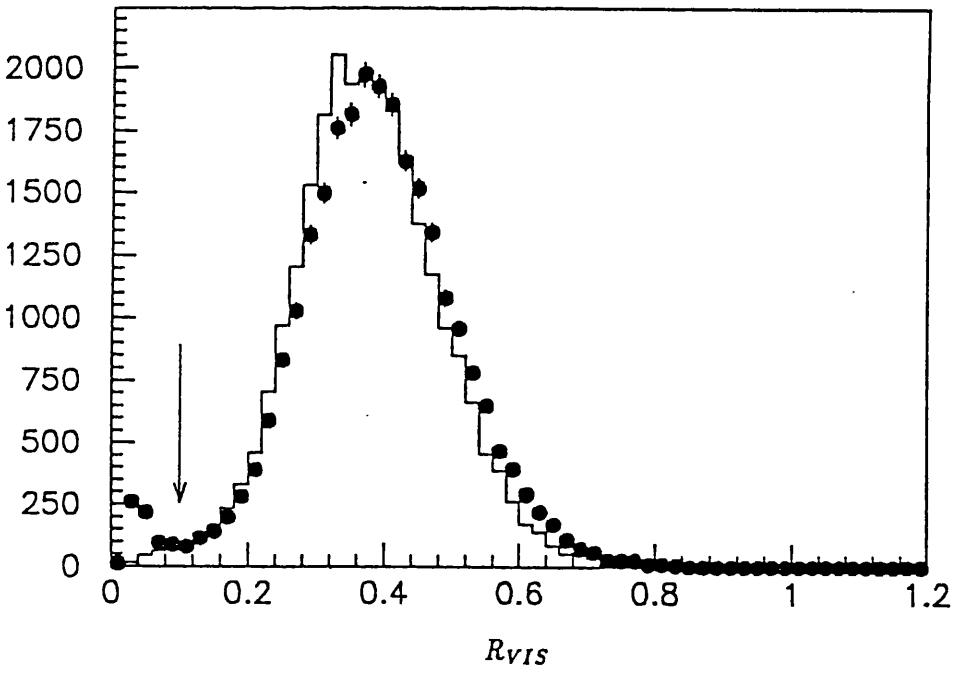

Figure 6.3: Measured distribution of R_{vis} for hadronic event sample with all other cuts imposed (data points). Also shown is Monte Carlo prediction using QCD parton shower model

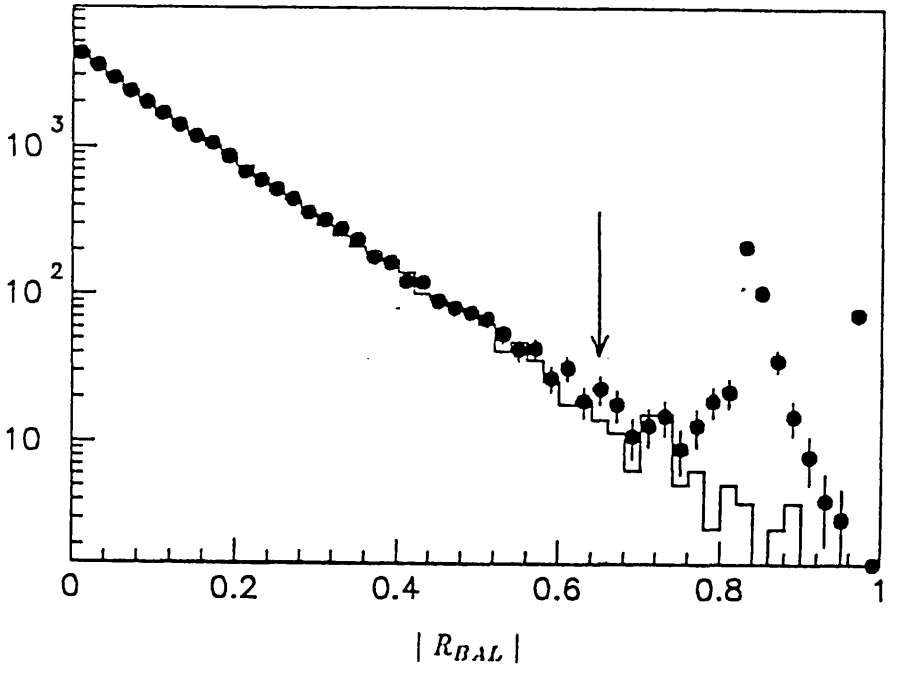

Figure 6.4: Measured distribution of R_{bal} for hadronic event sample with all other cuts imposed (data points). Also shown is Monte Carlo prediction using QCD parton shower model

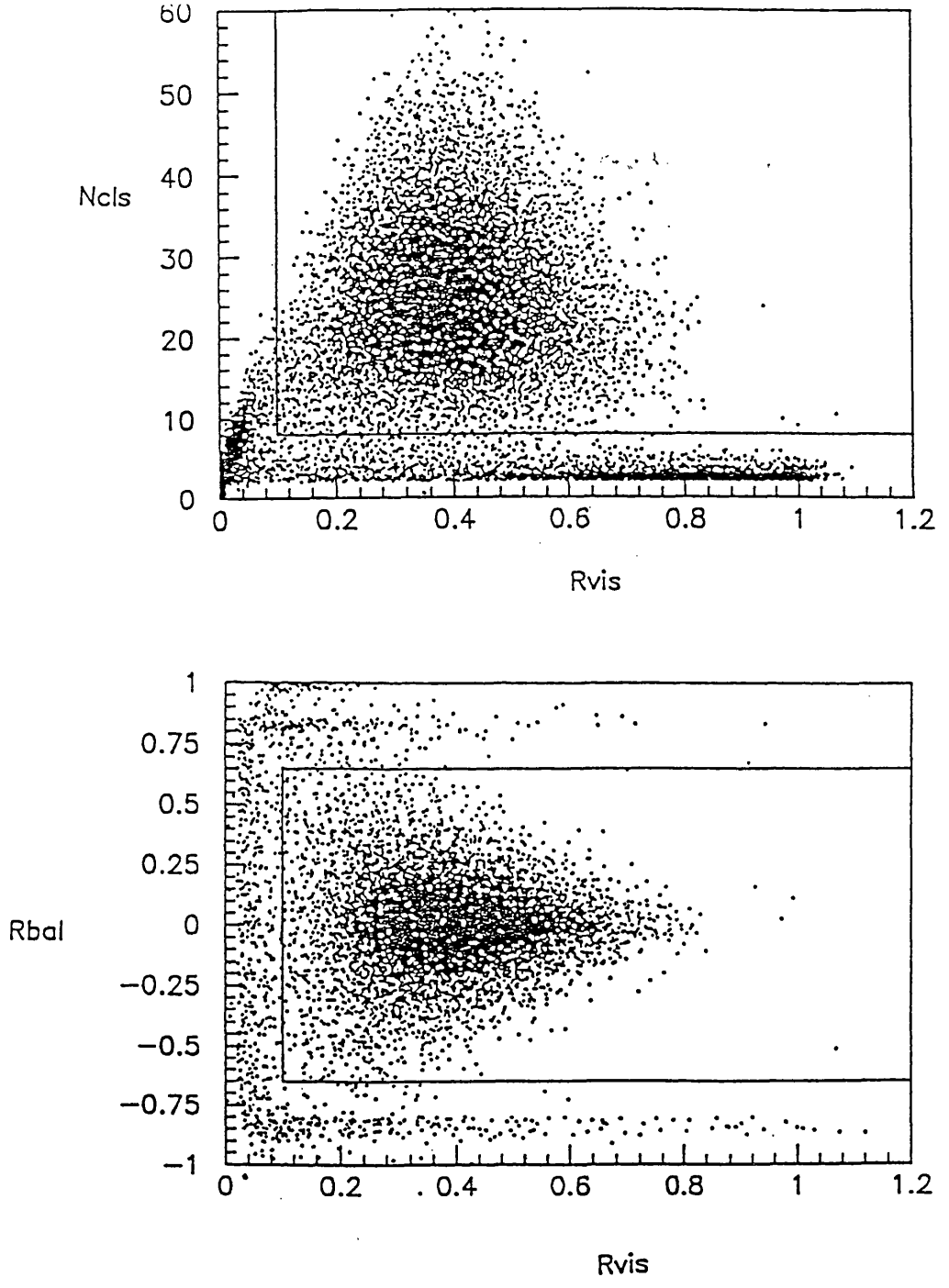

Figure 6.5: Scatterplots of a) N_{clus} against R_{vis}, and b) R_{bal} against R_{vis}, with the hadronic selection cuts shown as dashed lines.

Chapter 7

Extraction of the Number of Neutrino Generations from a Fit of the Z° Lineshape to the Hadronic Cross Section Data

To determine the number of neutrino generations, total hadronic cross sections (in nb) at different energy points are calculated by combining the hadronic event selection of chapter 6 with the luminosity measurement of chapter 5. A fit of the Z° lineshape to this data is performed, from which a measurement of the number of neutrinos is extracted.

7.1 Hadronic Cross Section Data

7.1.1 Beam Energy Measurement at LEP

Precision measurements of the Z° resonance at OPAL require an accurate knowledge of the LEP beam energy. Small, well understood, errors are desirable on both the absolute energy scale and point to point differences. The LEP beam energy is derived during the run from measuring the magnetic field of the bending magnets. It is not possible to use the actual magnets that form part of the accelerator, as the measurements would disturb the beam, so a set of reference

magnets are used. These are identical to the main ring magnets and are powered in series, so the field is the same up to a known correction factor. The field is measured in two ways; by a Hall probe, which gives a continuous measurement to an accuracy of about $\pm$ 100 MeV, and by a "flip coil" method which is usually carried out once per fill. The flip coil gives a stable precise measurement to $\pm$ 10MeV, although the absolute scale is considerably more uncertain. The most accurate absolute calibration of the energy scale was carried out by filling the machine with protons, which can be injected at a known energy, and have a negligible energy loss to syncrotron radiation. This gives a calibration of the beam energy to $\pm$ 30 MeV. The beam in any particular fill has a gaussian spread in energy with a standard deviation of $\sim$ 40 MeV, but this can be neglected in the analysis since the scale of variation of the resonance curve is much larger.

7.1.2 Summary of 1989 Data

Data was taken at eleven energy points across the Z° resonance, summarised in table 7.1. The data at each energy point represents several fills of LEP, and the final energy achieved by the machine showed small deviations on a fill by fill basis from the target energy. The data for a given energy point is therefore a sum of data from a small($\pm$ 20MeV) spread of energies around the quoted energy. The energy in the table represents the luminosity weighted average of the individual mean fill energies. For the luminosity calculation, the Bhabha cross sections for the calorimeter and tube chambers (see sections 5.2.2,5.4.2) were determined for each fill using the measured energy, so the integrated luminosity of each fill has a negligible error from the energy spread of any particular point.

7.1.3 Error Treatment for Hadronic Cross Sections

The hadronic cross section at each energy point has statistical errors associated with both the hadronic event selection and the luminosity measurement, although the contribution from the hadronic events is always larger and is dominant away from the peak. The 1% point to point systematic error in the luminosity measurement (section 5.4) is assumed to be random and uncorrelated between energy

$\sqrt{s}$(GeV)	$\mathcal{L}_{int}$(nb^{-}1)	N$_{had}$	σ_{had}(nb)
88.278	115.1±1.6	569	5.04±0.23
89.283	80.7±1.4	766	9.68±0.40
90.284	103.7±1.6	1990	19.56±0.56
91.034	210.9±2.3	6192	29.94±0.58
91.289	186.2±2.1	5633	30.86±0.62
91.529	230.8±2.4	6612	29.21±0.55
92.282	85.5±1.5	1781	21.24±0.66
92.562	9.2±0.5	150	16.66±1.62
93.286	111.4±1.7	1286	11.77±0.39
94.277	95.4±1.6	710	7.59±0.32
95.036	17.7±0.7	112	6.44±0.66
Total	1246.6	25801	

Table 7.1: Hadronic cross section, σ_{had} at each centre of mass energy $\sqrt{s}$. The integrated luminosity, $\mathcal{L}_{int}$, and the number of observed hadronic event, N_{had}, are also given for each energy.

points. The errors in the final column of table 7.1 are calculated by adding the three contributions in quadrature. The point to point error in the energy measurement is also assumed to be a random error, uncorrelated between energy points.

In addition to the above, the hadronic selection and absolute luminosity measurement contribute overall normalization errors of 0.8% (section 6.5) and 2.2%(section 5.2.4) respectively, which have a totally correlated effect on the cross section at each energy. Adding these two in quadrature, an overall normalization error of 2.3% is obtained. A further source of common error is the machine energy absolute scale error, although this only affects the value of the mass of the Z°. Other lineshape parameters are totally independent of the absolute energy scale.

7.2 Fitting the Z° lineshape to the 1989 Hadronic Cross Section Data

7.2.1 General Method

To fit the Z° lineshape, a χ^2 minimization technique was used. The calculations described in section 2.2 were used to calculate theoretical values of the hadronic cross section for each of the eleven energies. To account for the correlated normalization errors, a covariance matrix method was used, where χ^2 is expressed as

$$\chi^2 = (\tilde{\sigma}^{\mathbf{meas.}} - \tilde{\sigma}^{\mathbf{theor.}})\mathbf{V}^{-1}(\sigma^{\mathbf{meas.}} - \sigma^{\mathbf{theor.}}) \tag{7.1}$$

where $\sigma_{\mathbf{meas.}}$ is an 11 component vector containing the measured hadronic cross sections at each energy, $\sigma_{\mathbf{theor.}}$ is an 11 component vector containing the theoretical cross sections at each energy, and $\mathbf{V}^{-1}$ is the inverse of the covariance matrix of the data. For a derivation of this expression, the reader is referred to [33], or other introductory texts on statistics. The covariance matrix elements are given by

$$\mathbf{V}_{ij} = \delta_{ij}(dX_i)^2 + (dN)^2\sigma_i\sigma_j \tag{7.2}$$

where dN is the overall normalization error of 2.3%, dX_i is the individual error associated with the energy point i, σ_i, σ_j are the hadronic cross sections for energy points i, j, and δ_{ij} is the kroneker delta function. The uncorrelated errors are taken into account by the first term of equation 7.2 which is non-zero only for the diagonal elements of the matrix, and the correlated normalization error is accounted for by the second term. The first term, dX_i, includes the error from the hadronic cross section $d\sigma_{had}$ (listed in the last column of table 7.1) plus a term from the point to point error in the energy measurement, ΔE, and is given by

$$(dX_i)^2 = d\sigma_{had}^2 + (\sigma_{had}^{theor.}(\sqrt{s} + \Delta E) - \sigma_{had}^{theor.}(\sqrt{s} - \Delta E))^2$$

The second term is the covariance of the cross section at any two energy points. The covariance σ_{xy} [1] of two variables x,y is in general defined by

$$\sigma_{xy} = \Sigma_k (x_k - \overline{x})(y_k - \overline{y}) \tag{7.3}$$

where $\overline{x}, \overline{y}$ are the expectation values for these variables and x_k, y_k are the k^{th} sampling of these variables. This general definition relates to a situation where x and y are sampled many times and the covariance is estimated from these samplings. Applying this to the hadronic cross section data, x and y are cross sections at different energies, and we only have a single sample of them, but from independent sources we have an estimate of an overall normalization error. We expect that our data might depart from the true value by the overall normalization error, and that this will be by the same fraction and sign in x and y. Re-writing equation 7.3 we obtain

$$\sigma_{xy} = \overline{x}\,\overline{y}\Sigma_k(\frac{x_k}{\overline{x}} - 1)(\frac{y_k}{\overline{y}} - 1) \tag{7.4}$$

and then our best estimate of the terms in the above equation using measured quantities is

$$\overline{x} \;=\; x_{meas}$$

[1] Note that this σ is different to the σ for the hadronic cross section. This confusion is hard to avoid without defying all convention - one can only assume cross sections were allocated their standard symbol before anyone started using statistics very seriously on them.

$$\overline{y} = y_{meas}$$
$$\Sigma_i(\frac{x_i}{\overline{x}} - 1)(\frac{y_i}{\overline{y}} - 1) = dN \times dN$$

which, when substituted into equation 7.4, give the second term in equation 7.2.

To determine parameters of the Z° lineshape, a particular theoretical calculation is chosen, with the required parameters left free. An initial estimate of these parameters is given as input to the calculation, and theoretical cross sections calculated for each energy point. χ^2, from equation 7.1, is then minimized with respect to these parameters to give the fitted values. The MINUIT [34] program is used to carry out the minimization procedure.

7.2.2 Results from the Model Independent Fit

The s-dependant Breit-Wigner convoluted with initial state radiation (see section 2.2.3) was fitted to the data with M_z, Γ_z and σ_{had}^{pole} as free parameters (σ_{had}^{pole} being the cross section at $s = M_z^2$ without initial state radiation corrections). The calculation of initial state radiation includes a full 1st order calculation with exponentiation of soft photons to all orders [35].

The parameter values obtained are;

$$M_z = 91.145 \pm 0.022 \text{ (exp)} \pm 0.030 \text{ (LEP) GeV}$$
$$\Gamma_z = 2.526 \pm 0.047 \text{ GeV}$$
$$\sigma_{had}^{pole} = 41.2 \pm 1.1 \text{ nb}$$

The value of χ^2 obtained for this fit is 4.5 for 8 degrees of freedom. The errors for each parameter are calculated by stepping the parameter away from the value which minimizes χ^2, at each step minimizing χ^2 with respect to the other parameters, and determining the value of that parameter for which χ^2 increases by one.

To obtain the invisible width we take the measured width and subtract the theoretically calculated visible widths (using the method and numerical values from section 2.2.3), giving

$$\Gamma_{inv.} = 541.8 \pm 47(exp.)^{-47}_{+21}(theor.)$$

is obtained, giving the number of neutrino generations as

$$N_\nu = 3.26 \pm 0.28(exp.)^{-0.28}_{+0.13}(theor.)$$

using the calculated value of the width for neutrino pair production (section 2.2.3). The result is consistent with three generations, although it does not strongly exclude the possibility of a fourth generation. The measured value of the σ^{pole}_{had} is consistent with the standard model prediction. The mass of the Z° is a free parameter in the standard model, and this measurement, together with that of the other LEP experiments, represents the most accurate determination to date. The error arises largely from the absolute calibration of the LEP energy scale and is common to and correlated in all LEP experiments.

7.2.3 Results from the "Free Neutrino" Fit

In this fit, the theoretical model used to calculate the lineshape assumes a full standard model, but in which the number of neutrinos is a free parameter (see section 2.2.4), so the only other free parameter is M_z.

The results from this fit are;

$$M_z = 91.141 \pm 0.022 \text{ (exp)} \pm 0.030 \text{ (LEP) GeV}$$
$$N_\nu = 3.09 \pm 0.19(\text{exp})^{+0.06}_{-0.12}(\text{theor.})$$

and a value of χ^2 of 5.5 for 9 degrees of freedom is obtained. This result excludes a fourth standard model generation of light neutrinos at the 95% confidence level. The free neutrino fit exploits the large difference in the peak cross section of a lineshape with 3 neutrinos and 4 neutrinos, the experimental data being statistically the most precise in the region of the peak. To further demonstrate that a fourth generation of light neutrinos is excluded, the fit can be performed assuming 3.0 and assuming 4.0 generations. The probability of obtaining the measured data under the assumption of three generations is 54%, whereas the assumption of four generations results in a probability of the measured data of 0.05%. The hadronic cross section data with the standard model predictions for

the lineshape superimposed assuming 3 and 4 neutrino generations is shown in fig 7.1.

7.3 Dependance of Results on the Different Sources of Experimental Error

It is interesting to compare the influence of the various sources of experimental error on the final results, especially those arising from the luminosity determination which formed a significant part of the authors own work. The point to point errors and the overall normalisation errors have quite different effects and will be considered separately.

7.3.1 Point to Point Errors

The different contributions to the point to point error are summarised in table 7.2. The point to point error on any one data point is in general dominated by the statistical error in the number of hadronic events The last column of the table gives the error (in nb) on the cross section if the point to point systematic error in the luminosity is set to zero. Only at the peak of the Z° resonance does this point to point luminosity error make a significant contribution to the total error, and even then the point to point error, when added in quadrature to the combined statistical error, increases the overall error by only 20%. The χ^2 of the fits is small so there is no suggestion that systematic errors have been underestimated, and as the dominant contribution to the point to point error is statistical, any effect of any overestimation of systematic error is small. As an illustration, the model independent fit is repeated, but with the systematic point to point error on the luminosity set to zero. In practice this puts a slightly greater weight on the data points at the peak of the resonance. The results obtained are:-

$$M_z = 91.141 \pm 0.021 \text{ (exp)} \pm 0.030 \text{ (LEP) GeV}$$
$$\Gamma_z = 2.528 \pm 0.040 \text{ GeV}$$
$$\sigma_{had}^{pole} = 41.1 \pm 0.9 \text{ nb}$$

Different Contributions to the Error on Hadronic Cross Sections					
σ_{had}(nb)	Error contribution (in %) from different sources				$\Delta\sigma_{had}$(nb)
	Total	ΔN_{had}^{STAT}	$\Delta\mathcal{L}^{STAT.}$	$\Delta\mathcal{L}^{pt.topt.}$	(no pt. to pt.)
5.04±0.23	4.56	4.2	1.4	1.0	0.226
9.68±0.40	4.04	3.6	1.73	1.0	0.38
19.56±0.56	2.86	2.24	1.54	1.0	0.52
29.94±0.58	1.94	1.27	1.04	1.0	0.50
30.86±0.62	2.01	1.33	1.12	1.0	0.54
29.21±0.55	1.84	1.23	1.04	1.0	0.45
21.24±0.66	3.11	2.37	1.75	1.0	0.63
16.66±1.62	9.7	8.16	5.43	1.0	1.61
11.77±0.39	3.3	2.79	1.53	1.0	0.37
7.59±0.32	4.22	3.75	1.68	1.0	0.31
6.44±0.66	10.2	9.45	3.95	1.0	0.65

Table 7.2: Table showing the relative contributions of the statistical errors on the luminosity measurement and hadronic event selection and the point to point luminosity systematic error.

The value of χ^2 obtained for this fit is 5.1 for 8 degrees of freedom, indicating the goodness of fit is not compromised. The best fit values of the parameters are not significantly changed and the errors are only slightly reduced. The point to point luminosity error is assumed to be random in the above analysis. Although there is no evidence for a systematic variation with energy of the luminosity measurement, it cannot be ruled out below the 1% level. To check the effect this might have on the results, a 1% systematic slope was imposed on the 11 data points by decreasing the lowest energy point by 1.0%, the second lowest by 0.8%, and similarly for all points in order of energy, therefore increasing the highest energy point by 1.0%. The model independent fit was repeated, this increased the measured mass of the Z° by 10 MeV and had a negligible effect on the other parameters.

One concludes that the data are consistent with zero point to point systematic error in the luminosity, but that the systematic error assigned of 1.0% has little effect on the results or their significance with the present level of statistical accuracy. Even the rather unlikely case of a strong energy dependance of the point to point error does not significantly change results

7.3.2 Overall Normalization Error

From table 7.2 it can be seen that the error on each of the three data points in the region of the Z° peak is approximately 2%, and as these are uncorrelated point to point errors, the peak would be defined to a precision of about 1% if only the point to point errors were considered. The overall normalization error of 2.3% is therefore the limitation on the accuracy with which the peak cross section is determined. The strong dependance of the peak cross section on the number of neutrino families is exploited in the free neutrino fit, and so the size of the overall normalization error directly affects the precision of the final result on the number of families.

If the overall normalization error is set to zero, then the data give a value for the number of families, N_ν, of

$$N_\nu = 2.95 \pm 0.025(\text{exp})^{+0.06}_{-0.12}(\text{theor.})$$

thus in this scenario the measurement is dominated by theoretical errors. The χ^2 for the fit of 6.2 for 8 degrees of freedom is still good.

To demonstrate the importance of a low systematic error on the overall normalization, the systematic error on the absolute luminosity determination was set to 5%. This accuracy was obtained for the first OPAL publication [24] on the Z° mass and width, for which the forward calorimeter alone was used for the luminosity determination. If the free neutrino fit is now repeated, then the results obtained are;

$$M_z = 91.141 \pm 0.022\ (\text{exp}) \pm 0.030\ (\text{LEP})\ \text{GeV}$$
$$N_\nu = 3.23 \pm 0.30(\text{exp})^{+0.06}_{-0.12}(\text{theor.})$$

Within the context of the standard model, the error on the number of neutrino generations is less important than the confidence level with which extra generations can be excluded. With a 5% overall normalization error, then if the number of neutrino generations is set to 4, a χ^2 of 12 for 9 degrees of freedom is obtained, which corresponds to a probability of 20% of obtaining the data. A fourth generation could therefore not have been ruled out with a normalization error of this magnitude.

7.4 Conclusions

These results show the possibility of a further generation of light neutrinos within the standard model to be extremely remote. Similar analyses by the other LEP experiments [36] support this conclusion. The principle source of uncertainty in the measurement was the overall normalization of the Z° lineshape, but interpreting the results strictly within the context of the standard model, further precision would not change the final conclusion. No departure of the data from the standard model is observed. Under the assumption that nature is composed

of complete families of two quarks, a charged lepton, and a light neutrino, the only fermion not yet observed[2] is the top quark.

The OPAL collaboration has performed a combined fit to all visible decay channels of the Z° [37] and derived from this a value for the number of neutrino generations of

$$N_\nu = 2.73 \pm 0.\ 26(\mathrm{exp})^{+0.02}_{-0.04}(\mathrm{theor.})$$

The method was similar to that described in section 7.2.2, but rather than using partial widths calculated in the standard model, partial widths derived from the data were used. The discrepancy between this value and the one in section 7.2.2 is due to the difference between the hadronic width measured by OPAL and the standard model expectation. The OPAL value is the higher, increasing the visible width, and hence decreasing the visible width and number of neutrino generations. The combined fit has the advantage of greater model independence, as only the width for $\nu\overline{\nu}$ has to be calculated, but requires an understanding of the systematic uncertainties in detecting all decay channels.

Whilst the accuracy of the data is sufficient to rule out a further light neutrino generation, no strong limit can be placed on other unseen final states with coupling strengths less than those for neutrinos (ie. which might cause a measurement of the number of neutrino generations to be 3.5, for instance). The dominant source of error is the overall normalization error, as was shown by the fit setting the normalization error to zero, so reducing the statistical error (by accumulating more data) will only achieve a result of greater significance if the overall normalization error can be reduced.

[2]Arguably the τ neutrino has not been "observed"; however it's production can be inferred from momentum imbalance on an events by event basis.

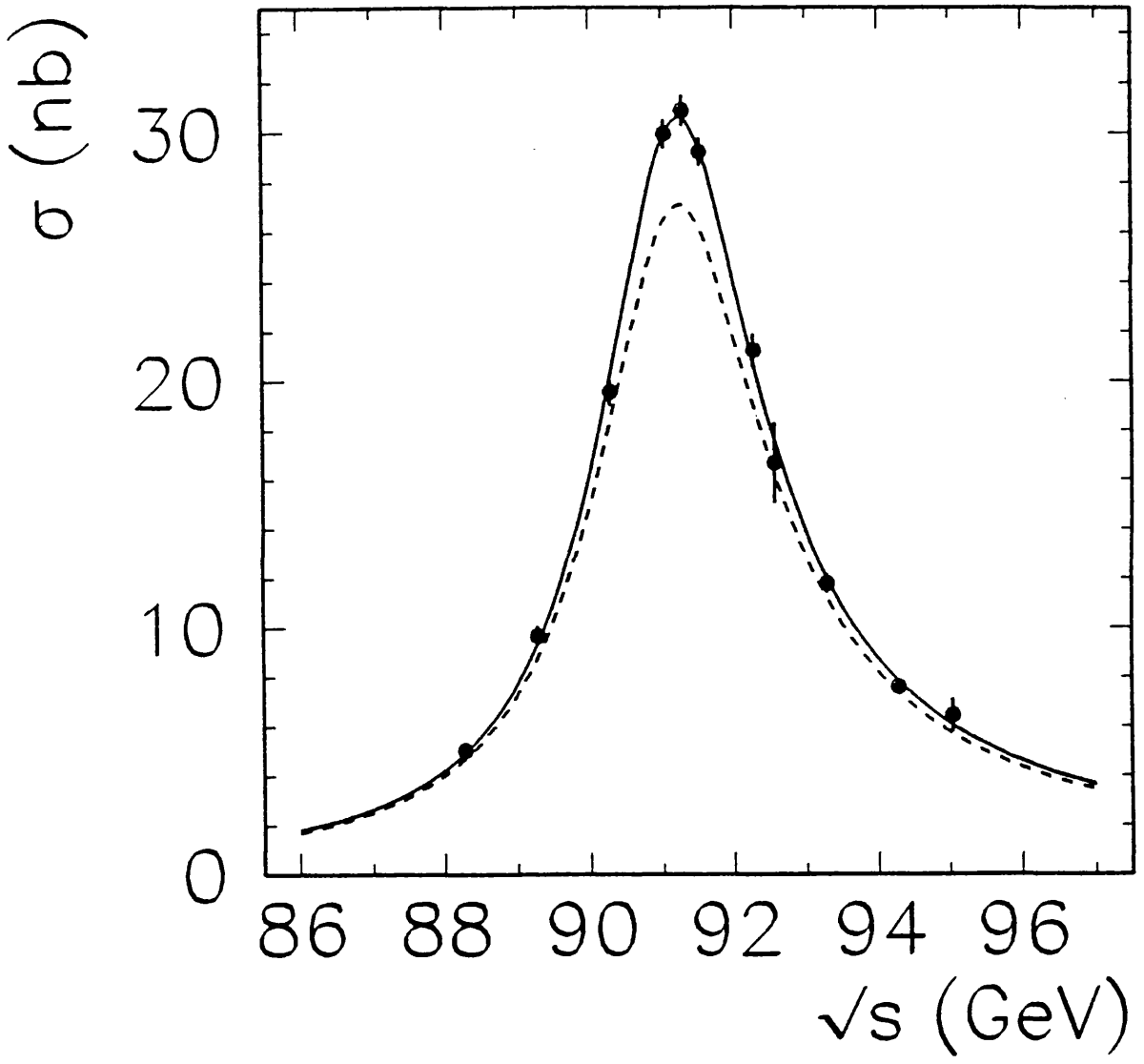

Figure 7.1: Hadronic cross sections plotted as a function of energy across the Z° resonance. The standard model prediction for 3 (solid line) and 4 (dashed line) neutrino generations is superimposed.

Appendix A

Tube Chamber Multiplexed Readout

A.1 Introduction

The tube chamber multiplexed readout electronics are based around hybrid integrator and summer circuits developed by the Rutherford Laboratory for the ALEPH experiment [22]. The tube chamber electronics was originally designed by Stephen Hall (University College London), who based his design on a similar system developed by Pedja Jovanovic (University of Birmingham) for the OPAL muon endcaps. The author first took responsibility for the electronics for the beam test of summer 1988, when a prototype version was being used. Due to the subsequent departure of Stephen Hall from UCL, the author then took full responsibility for the construction of the production system, including substantial modification to the original design, and the installation and commissioning of the electronics in OPAL.

A.2 Overview of System

A.2.1 Design Constraints

The principal constraints on the design of the tube chamber readout were as follows

- At each end of OPAL, there are 384 channels (approximately one for each tube), and it was considered necessary to have the value of charge collected on each channel available offline to allow a thorough study of the detector response. The space for cables running to the forward detector is extremely limited, leading to a need for multiplexing of the tube chamber signals using electronics mounted on the detector.

- LEP bunch crossings (BX) occur every 22 μs and OPAL makes a trigger decision 16 μs after each BX. In the case that there is no trigger for a particular BX, the tube chamber readout must be able to clear the front end electronics and be ready for the next BX within 6 μs after the trigger decision. The tube chambers do not provide a trigger as the calorimeter acceptance completely contains the tube chamber acceptance, and it was considered the calorimeter trigger would be sufficient.

- In the case of a trigger, while data is still stored on the detector based electronics, no further data can be taken. It is therefore highly desirable to minimize the time taken to readout the data, to minimize dead time. At the time of design of the tube chamber electronics, a (somewhat arbitrary) target deadtime of 1.5 ms was specified for OPAL, and the design conforms to this specification.

A.2.2 Operation Sequence

A block diagram of the tube chamber readout is shown in fig. A.1. The system has two main components; the "mothercards" which are mounted on the detector, and the "Eurocrate" which is in an electronics rack in the gondola. The mothercards are circuit boards which each contain four 8-channel integrator hybrids and a single summer hybrid. The operation of the the hybrids is controlled by timing signals originating in the Eurocrate. The functions of digitization of the data and interfacing to the VME processor of the data aquisition system are also performed by the Eurocrate. At each end a single Eurocrate controls 12 mothercards. In a data taking cycle the following sequence of operations is

carried out:-

1. 4 μs before BX a "pre-pulse" NIM signal is given to the Eurocrate. This acts as a general system clear (i.e. resets flip flops etc) and starts the timed sequence of operations. The timing is based on an internal 10 MHz clock

2. The Eurocrate opens an integration gate on each integrator hybrid channel. This is timed so that the integration gate is open in coincidence with BX. A one to one correspondence exists between hybrid integrator channels and detector output channels. The pulse from each detector channel is integrated, the integral corresponding to the total charge collected on that channel.

3. The integration gate is closed and the value of the integrated charge of each channel is stored on the hybrid. The readout remains in this state until a trigger decision is made. OPAL then issues a RESET or a TRIGGER.

   - If a RESET is issued the integrators are cleared of any charge stored, the clock is inhibited and the system waits for operation 1.
   - If a TRIGGER is generated, then the sequence continues as follows:-

4. The 12 mothercards are divided into 4 groups of 3 cards, and the 3 cards in each group are labelled 1,2,3. Channel 1 on mothercard 1 of each group is selected by means of Eurocrate control signals.

5. The charge on this channel is transferred to the summer hybrid, which converts this charge to a voltage level. This voltage appears on a differentially driven output connected to a 40m cable, the other end of which is connected to an ADC card of the Eurocrate.

6. Each Eurocrate contains 4 ADC cards, and thus each ADC card reads out 96 channels (the 3 mothercards in one group). The ADC cards digitize the input voltage value. This operation is carried out in parallel on the four ADC cards. The digitization is the longest part of the cycle (5μs)

and therefore this parallelism is necessary for reasons of speed. After conversion, the four ADC values are written into the local memory of the Eurocrate.

7. The next channel in sequence is selected and parts 5 and 6 of the cycle are carried out.

8. When all 32 channels on the four '1' mothercards have been digitized, the '2' mothercards are selected, and the 32 channels from these cards are digitized in sequence, followed by those on the '3' mothercards.

9. Once all 96 channels in all 4 groups have been digitized, and the 384 channels stored in the Eurocrate internal memory, an end of readout flag readable by the VME processor is set, and the clock inhibited. The VME processor takes control of the Eurocrate and copies the data in the internal memory to VME memory. The Eurocrate is then released and waits for operation 1.

A.2.3 Hardware Overview

The Eurocrate is composed of several circuit boards which are connected by means of a 96 way backplane. The backplane serves as simple connection between boards and any board can be put into any slot of the backplane; no arbitration is performed in passing signals along the backplane. The interface to the VME crate is by an 8-bit data bus and an 8 bit control bus. These are connected to the crate through connectors on the front of circuit boards. The connection to the mothercards is by means of 20 way screened twisted pair cable. There are two such cables at each end, and each cable carries both control signals to the mothercards, and the data signals from 6 mothercards. The Eurocrate uses TTL logic (HCT series) and the mothercard digital circuitry is CMOS 4000 series, to be compatible with the hybrids.

A.2.4 Brief Description of Individual Circuit Boards

Mothercard Contains the front end integrators which store the charge on each channel of the detector, and circuitry to decode the control signals from the Eurocrate and deliver the individual channel data sequentially on the output.

Timing Card Generates the sequence of timing signals to control the read out sequence. The sequence is fixed by the hardware, but the duration of each part of the cycle is programmable.

ADC Card Receives analogue voltages from the mothercards and digitizes them. There are four such cards in each Eurocrate.

Memory Card The internal Eurocrate memory is located on this card. During read out the addresses for writing data into the memory are generated on this card.

Control I/O Card Connected to 8 bit bus from VME, through which the operation of the Eurocrate is controlled. This bus is uni-directional; VME signals are received by the crate and interpreted.

Data I/O Card Connected to the VME by a 8-bit bi-directional bus. This transfers data between the VME and Eurocrate; the direction and route of the data transfer is controlled by signals from the control I/O card.

Trigger Card Receives NIM TRIGGER and RESET pulses from OPAL trigger and converts these to TTL levels used in Eurocrate logic.

Mothercard Driver Card Receives TTL level mothercard control signals from timing card and converts them to drive 40m cable.

Display Card Displays backplane voltage levels by means of front panel LED's.

A.3 Technical Description of Circuits

A.3.1 General Remarks

The communication in between boards in the Eurocrate is by means of a 96-way backplane, arranged in a 3×32 layout. Backplane assignments are shown in fig A.2; the three columns are labelled a-c and the 32 rows 1-32. On circuit diagrams, connections to the backplane are indicated by labels such as c4, with the letter lower case. Functional labels (such as EN1 for enable 1) have upper case letters. Two useful diagrams for an overview of the system, which should be referred to in conjunction with individual board circuits, are the timing diagram(fig. A.10), showing the sequence of control signals, and the signal/data flow diagram(fig A.4), showing where these signals are distributed amongst the different boards of the system. When data of more than one digital bit is referred to the convention used is that bit 0 is the lowest. "Read out" refers to the action of passing data from one place to another, whereas "readout" refers to the software/electronics that performs this function !

A.3.2 Mothercards

Mothercard Gate Sequence

A schematic diagram of the integrator/summer circuits is shown in fig A.5. Four FET switches control the propagation of signals through the system, labelled A-D. Switches A and B reside on the integrator hybrids, and there is one for every channel. The 32 switch A's are all operated simultaneously, whereas the switch B's can be operated either individually or together. If the simultaneous operation of all switch B's is being referred to the label SWB will be used, and the operation of an individual switch B will be denoted by SWB(n). The outputs of all the individual integrator channels from all four hybrids are connected to the input of the summer hybrid. Switches C and D reside on the summer hybrid, and there is only one of each per summer hybrid (and therefore one per mothercard). There are two phases of operation; the primary integration (before trigger/reset decision) and the readout (after OPAL trigger is set).

The primary integration sequence proceeds as follows:-

1. When the pre-pulse is received, SWA,SWB,SWC are closed and SWD is open.

2. Before BX, SWA and SWC are opened. Pulses on the inputs of the integrator are integrated and the charge collected on capacitor C1. As point X is a virtual earth, with SWB closed the identical charge is collected on capacitor C2. Capacitor C3 collects the sum of the charges on all of the integrators and places this on the output. [1]

3. 2μs after BX, when the pulse has been full integrated, the SWB is opened, isolating the charge on capacitor C2.

4. 500 ns later SWA and SWB are closed, discharging capacitor C1 and C3. Capacitor C2 maintains the individual channel charges

The primary integration sequence is now over, and the readout waits for the TRIGGER/RESET decision. In the case of a RESET, then the system returns to state 1 of the above list, and the C2 capacitors are discharged in the time interval between state 1 and state 2. In the case of a TRIGGER the readout sequence is initiated.

1. SWC opens.

2. SWB(1) is closed for 2μs. SWA is always closed during the readout phase, so closing SWB(1) references the input side of capacitor to virtual earth. The charge on C2 is thus fed onto capacitor C3, and appears at the output as a voltage level.

3. This voltage is placed on the output cable, and read in by the Eurocrate.

4. SWC is closed to discharge capacitor C3, ready to read out the next channel

5. The next SWB(n) is operated, and the above sequence is repeated, until all channels are read in to the Eurocrate.

[1]The sum facility is to allow the possibility of a fast trigger, although this is not used in the tube chamber readout. It is implemented in the muon endcap system.

Differential Receivers

The pre-amplifiers mounted on the tube chamber detector box differentially drive flat cables leading to the mothercards. The mothercard is divided into four identical input sections each containing 8 receivers and an integrator hybrid, as shown in fig A.6. The connection of the input cables to the mothercard is by means of 4 16 way IDC connectors. Fig A.6 also contains a diagram of the receiver circuit, which converts the differential input signal into the single ended signal required by the hybrid.

Hybrids

The hybrids are small ($\sim 5 \times 2$ cm) circuit boards containing miniaturised components, although the integrated circuits and semiconductors are otherwise standard types. The operational amplifier used in the integrator is an LF353, and the logic is 4000 series CMOS. The hybrids are both packaged in 20 pin S.I.L. form.

The integrator hybrid circuit is shown in fig A.7. The input lines SWA and SWB directly control the operation of these switches, a high logic level corresponding to the switch being closed. An individual SWB(n) is selected using the lines A0-A2; the 4099B decodes the three bit binary code into setting one of the Q outputs low. The DATA line acts as a chip inhibit on the 4099B so in practice the switch is selected by the A0-2 lines, but the actual switch opening and closing is controlled by DATA. The hybrid selection is also controlled by DATA; the A0-2 lines are common to all four hybrids. whereas each hybrid has an individual DATA line. The W/D and RESET lines are not used.

The summer hybrid circuit is shown in fig A.8. The operation of the switches in this circuit is straightforwardly controlled by the input lines, logic high corresponding to the switch being closed. SWT is a test facility (not used). SWD is used to perform an offset cancelling function; the operation of the switches itself causes a certain charge to be induced on the capacitors.

Mothercard Control Logic

The mothercard control logic circuit diagram is shown in fig A.9. SWA, SWB, SWC, SWD are directly controlled by the Eurocrate. The operation of the individual SWB(n) is controlled by the START A/D and DATA lines. IC12 is a binary counter which is reset to zero (by a logic low level on pin 2) during primary integration by the operation of SWB. The lowest bits of the counter (0-2) drive the integrator address lines (A0-2) and bits 3,4 select the hybrids via IC11. Thus initially lines A0,A1, and A2 are zero, selecting SWB(1) on the hybrids. IC11 is a binary decoder, and receives the higher order bits of the output of the binary counter IC12, and these are also zero. The output H1 (DATA on hybrid 1) remains off, however, as the chip is inhibited by a low level on the input DATA line (from the Eurocrate). The SWB(1) is actually operated (causing the value of charge collected on channel 1 to appear on the summer output) by DATA going high. Once the Eurocrate has read in this channel (on to a sample and hold chip) DATA returns low. The Eurocrate begins digitization, and the same logic signal (START A/D) is used to increment the binary counter(IC12), selecting SWB(2). This cycle is repeated until all channels on hybrid 1 are read out. The next hybrid is then selected by the bit 3 of the counter going high, selecting DATA for hybrid 2. All 32 channels are read out by this continuation of this cycle.

The mothercards are read out in groups of three cards, the three cards in a group being read out sequentially. The selection of a particular mothercard in sequence is controlled by IC10. This is reset during primary integration by SWB, setting the output on pin 3 high. The falling edge of bit 4 of the counter causes the next output in sequence to go high. One of these outputs is connected to IC8 via a wire link, and only when the connected output is high can DATA be passed through and cause readout. Thus the mothercard address is set by means of the which output of IC10 is connected to IC8 via the wire link.

A.3.3 Timing Card

The circuit diagram for the timing card is shown in fig A.10, and the IC types shown on the layout diagram (fig A.11). The duration of each operation in the read out cycle is programmable via timing values downloaded into the timing RAM (IC23) during an initialization phase. However once this has been performed, and a pre-pulse received, the read out is independent of external software until the data is stored in the Eurocrate internal memory.

The timing card is driven by a 10 Mhz clock (IC11). This drives an 8 bit counter (IC's 2 and 12, suitably coupled). The counting can be effectively inhibited by the state of the $\overline{Q}$ output of the latch (IC29A). When the readout is waiting for the pre-pulse, the counting is inhibited. The pre-pulse sends the $\overline{Q}$ output of the latch low, which performs the following functions:-

1. The counter (IC2/12) is reset.

2. The address generator (IC7) is reset (by means of a pulse generated by IC's 30,20,31)

3. The digital comparator (IC15) is enabled.

The address generator (IC7) sets the address of the timing RAM, and also the input 4-bit word to the 4-bit binary to 16 sequencers (IC's 6,16). The address is initially 00000, selecting word 0 on the RAM, and enabling output 1 of IC6. Only one of IC6 and 16 is enabled at a time as the chip enable lines are connected to complementary outputs of a latch (IC29B). For primary integration, IC6 is enabled, IC16 being enabled for the readout sequence.

The digital comparator(IC15) has the first timing data byte on it's Q input, and the counter(IC2/12) byte output on it's P input. When Q is less than P, the output is high. When the counter byte equals the timing byte, then the output of the comparator goes low. As a result the address generator is incremented by one, selecting the next timing value and the enabling the next output of the sequencer, and the counter reset. This is the mechanism by which the timing values stored on the RAM are converted to actions lasting a set number of clock pulses.

Each timing value therefore corresponds to a set time for a particular output of IC6/16 to be low. The conversion of this sequence to the operation of the various control signals (SWA,DATA etc) is performed by gates and latches (IC's 8,9,19,25,26,27). The first 16 timing values in the RAM are those used to set the times for IC6 sequence and the second 16 are those used to set the times for the IC16 sequence.

A full readout is carried out unless the Eurocrate receives a RESET pulse; i.e. TRIGGER is the absence of RESET. In the case of a RESET, the address generator(IC7) is reset, and the latch(IC29A) reset, inhibiting the clock. The readout is then effectively stopped until the receipt of the next pre-pulse. The sequence is timed so a RESET arrives during step 9. If no RESET arrives, then upon reaching step 10, latch(IC29B) is flipped, which has the following effects:-

1. The address generator is reset to zero.

2. The second sequencer(IC16) is selected, and the first sequencer(IC6) disabled

3. Bit 4 of the memory address is set high, so the address generator now accesses RAM locations in the range 17-32.

4. A pulse is generated on the TRIGGER RECEIVED line by IC's 20,30,31 (this is used by the memory card).

Now the operation cycle is similar to that described above, except that now outputs of IC16 go low in sequence, for times as stored in the RAM from address 17 onwards. The readout phase, however, requires the repetition of a control signal cycle 96 times. Thus when step 7 of IC16 is reached, the address generator is reset, via gates(IC5) which delay this reset until the ADC's have all set end of conversion flags (on the circuit diagram, EOC1-4 logic high). The pulse that resets the address generator also increments a counter (IC's 27,17,26,28) wired to count 96 cycles. The highest 2 bits of the counter are sent to the ADC card to select different mothercards. When this counter reaches 96, the output inhibits step 7 reseting the address generator (via IC5) and the sequence progresses onto 8. When the sequence reaches step 11, the latch IC29B is reset, disabling output

11 of IC16 and enabling output 11 of IC6, which performs the same function as a RESET from LEP.

A.3.4 ADC Card

The ADC card performs the function of receiving the differential signal from the detector, acquiring the data in a sample/hold, and digitizing it. The circuit diagram for the ADC card is shown in fig A.12. Each of the four ADC cards reads in the data from three mothercards. The three mothercards in a group have separate output lines to the ADC card, so the three inputs on the ADC card reading the different mothercards are selected in turn by the DG508 demultiplexing chip(IC3). The other three inputs on the card are not used. The selection of different mothercards is controlled by the highest two bits of the 1-96 counter on the timing card, so a new input channel is selected every 32 cycles as required. After demultiplexing, the signal is fed into the AD585 sample/hold(IC4), and once data is "held", the digitization is started by the AD7572 12 bit ADC chip(IC5). The control signals for these steps are the SAMPLE/HOLD and START A/D respectively, and these signals originate on the timing card. The ADC chip has an "end of conversion" (EOC) output which goes low when digitization is started, and high when it is complete. IC7/8 form a 16 bit latch; 12 bits are connected to the ADC outputs, and 2 bits have as input the ADC card address, a (binary encoded) number from 1 to 4 set by wire links. The latch acquires data while EOC is low, and holds data when EOC is high. At this point the sample/hold can begin acquiring the next data, minimizing read out time. In parallel, the memory card reads data from the latches and writes it into the data RAM, initiated by the EOC flag. The latches of the 4 ADC cards are output enabled in turn (all ADC card use the same internal data bus); to achieve this each card must have the latch enable linked to a separate ENn line. The convention adopted is that the ADC card address 1 is linked to EN1, address 2 to EN 2, etc. Similarly, each ADC card delivers an individual EOC to the timing card, and the same convention is used; ADC card address 1 is linked to EOC 1. EOC and EN connections are made by means of wire links on the

boards.

A.3.5 Memory Card

The memory card operates in two basic modes; read out mode, where it acquires data from the ADC cards and writes into into the data RAM, and external mode where the RAM is accessed via the interface to allow the data be read by the VME. The memory card circuit diagram is shown in fig. A.13. The mode of the card is determined by the EXT MEMORY CONTROL line, which controls the direction the bi-directional buffers (IC's 4,5,3,11) operate in, and hence the source of the memory address lines and also the memory write enable.

During the primary integration phase, the memory card logic is "locked" in the following state; pin 11 of the binary decoder (IC12)is low which effectively inhibits the propagation of the 10 Mhz clock pulses through the divide-by-8 counter (IC13). Once a read out phase is started, a TRIGGER RECEIVED pulse is sent by the timing card, which resets the address generator counters (IC1,2). Some time later the END OF CONVERSION line goes low, when the first digitization is finished. This resets the counter IC9, which in turn sets pin 15 (EN1) of the decoder(IC12) low and pin 11 high. This releases the counter/divider IC13, and causes the data from ADC 1 to appear on the data bus. The divider/counter/decoder IC's (13,9,12) act to step through the enable lines EN1-4, also entering each 12-bit data into the memory by strobing the write enable with the output of IC13. The 4 12-bit data are entered into different memory addresses as the highest address bits are set by the ADC card address; thus ADC 1 writes into locations 0, ADC 2 into 128, etc. Once all four enables have been set low in turn, pin 11 of IC12 returns low and the system is locked until the next END OF CONVERSION. The falling edge of the pin 11 output increments the address generator, so the next 4 data from ADC's 1-4 write into locations 1, 129, 257, 385 respectively. This cycle is carried out 96 times, at which point all data is in memory, and read out is finished.

In external mode, the memory is addressed from and the data read by the VME via the control I/O and data cards. The procedure will be described in

section A.4.

A.3.6 Trigger Card, Mothercard Driver Card, Display Card.

These cards are quite simple and require little explanation. Circuit diagrams are given in figs. A.14, A.15, A.16. At LEP the trigger performs the function of converting the NIM levels of the OPAL trigger signals to TTL levels. The trigger input and associated logic was developed for test beam use but is not used at LEP.

The mothercard driver converts the TTL level mothercard control signals generated on the timing card into signals capable of driving a 40m cable.

The display card uses LED's on the front panel to show the state of the various control lines on the backplane. In addition, certain backplanes are tied high on this card via 10 kohm resistors, to avoid error by lines being left undefined.

A.3.7 Control I/O Card

The Control I/O card (fig. A.17) is connected to the VME by an 8-bit bus, and on the basis of the levels on the various lines of the bus, the interface to the readout is controlled. The lowest 3 bits of the control bus set the readout "mode" and the highest 5 are control lines that are routed according to the mode selected. There are 6 modes:-

- Mode 0 — load timing RAM address
- Mode 2 — autonomous data taking (i.e controlled only by PRE-PULSE and RESET)
- Mode 3 — Load data RAM address
- Mode 4 — Read/write lowest 8 bits from data RAM
- Mode 5 — Read/write highest 4 bits from data RAM
- Mode 7 — Read/write timing RAM data

The mode number is the (binary) value that the lowest 3 control bits must take to select that mode. These three bits are input to the 3-to-8 decoder(IC11) via the input buffer(IC10), and one of the decoder outputs marked *0-*7 is set low according to the mode number (*0 low for mode 0 etc). This enables the outputs of one of the buffers/strobes (IC's 1-8). The other 5 bits and bit 0 are connected to the inputs of these buffers/strobes, so external levels on the control bus are routed onto various internal control lines, according to the mode. The use of the control modes will be explained after the data I/O card has been described, as control of the readout uses both in parallel.

A.3.8 Data I/O

The principle of operation of the data I/O card is similar to the control I/O card, the main difference being that data passes in both directions through the data I/O card. The circuit diagram is shown in fig. A.18. The 8-bit external data bus is connected to buffers and latches (IC's 1-8) and one of these is enabled by the lowest 3 bits of the control bus, determining the route of the data flow.

A.4 External Control of the Readout from VME

The readout is controlled by a VME computer (FIC) based on the Motorola 68020 microprocessor, via an MVME340A interface. Programs written in 68000 assembler are used to place the necessary data bytes on the control and data buses. To carry out the full data cycle three key steps are taken; Initialisation, data-taking, and accessing the data.

A.4.1 Initialization

Before data taking can begin, a suitable set of timing values must be down loaded. To an enter a timing value in the timing RAM, the following sequence is carried out:-

1. Mode 0 is selected, with the other 5 control bits containing the address required.

2. By selecting mode 0, bit 1 of the data bus controls the latch strobe of IC4 of the control I/O card. By setting this to 0 and back to 1, the address is latched into IC4.

3. Mode 7 is selected. Bit 3 (CONTROL WRITE ENABLE) is high, meaning the timing RAM is not write enabled, and bit 7 (DIRection) is high setting the direction of buffers on the data bus to write data.

4. The (8-bit) timing value is put on the data bus, and it is routed to the timing RAM data port.

5. Bit 3 (CON. WRITE ENABLE) is strobed, so the timing memory reads the value.

In practice, care must be taken to avoid data being corrupted by simultaneous switching of data and write enable lines. Many of the problems with the initial design were of this nature.

The timing data are read back immediately after being written during the initialization phase, to check that the data has been correctly written. The read cycle is similar to that above, except that bit 7 (DIR) is set low to route data in the opposite direction, and the CON. WRITE ENABLE is not strobed.

A.4.2 Data Taking

Once all timing values are down loaded, mode 2 is selected. This puts the readout into data taking mode, where it responds directly to the NIM trigger inputs, and is independent of VME control. When the read out cycle is finished, then an END OF READOUT flag is put on bit 2 of the data bus; this is registered by the VME and the data transfer cycle can start.

A.4.3 Data Transfer

The reading of a 12-bit data in the data RAM is carried out by the following sequence of operations.

1. Mode 3 is selected. The two most significant bits of the address are placed on bits 6 and 7 of the control bus

2. The lowest 8 address bits are placed on the data bus.

3. Bit 3 of the control bus is strobed to latch the address bits into IC's 12(control I/O) and 2(Data I/O).

4. Mode 4 is selected, with control bits 3,4,5 high. The lowest 8 bits of the data RAM appear on the VME data bus.

5. Mode 5 is selected, with control bits 3,4,5 high. The highest 4 bits of the data RAM appear on the VME data bus.

A.5 Trouble Shooting

This is a difficult subject to write about; the system is fairly complex, and not all possible problems can be discussed, firstly because there isn't space, and secondly because not all possible error conditions have occurred. Nevertheless, there are a number of debugging techniques and aids developed by the author which can help to pin down problems.

A.5.1 Test Software

The following test programs are stored on the OS9 system on /nfd2/ncw/tube with the executable modules in /nfd2/ncw/cmds. Queries can be addressed to the author, or in his absence, Gordon Crone. All these programs are stand alone and do not require the general data aquisition to be running. However, these programs call as subroutines the actual assembler code used in the full data aquisition, and if these test programs behave correctly, then it is unlikely that there are faults in the interfacing.

TESTIME_NEW This writes the timing data to the timing RAM and reads it back, in a continuous loop (to allow a search for intermittent errors). If there are no errors, then a success message is written to the screen with a

loop count, and if errors occur, then the written and read timing data are printed, and the program stops.

TESTWRT_NEW This writes data to the data RAM, and reads it back. Prompts are offered for the range of memory to be written to, and the data to write. Only the top 4 or lower 8 bits of memory can be written in a single pass of the program, as the memory board is not designed for 12 bit external input. The values read back are displayed on the screen.

TESTRUN Downloads timing data and puts system in data taking mode. The system can now be triggered with a pulse generator attached to the pre-pulse input (repetition rate should allow for a complete hardware readout between pulses i.e. 2 ms) . No data is read into the online system, but it is easiest to look at signal traces with an oscilloscope this way, as patterns repeat at regular intervals.

TESTGO Operates a complete data taking cycle 20 times. A pulse generator must be used to drive the pre-pulse input (use a rate of $\sim$10 Hz). The full 384 data are printed on the screen for each cycle.

A.5.2 Tracking Down Faults

The type of fault is the biggest clue as to what has gone wrong. There are basically two classes of fault; ones where the ONLINE complains that something is wrong, and ones where there is no ONLINE complaint, but the data is suspect.

ONLINE faults

There are two complaints that the ONLINE might issue:-

Error Loading Timing Data This means that at initialization the timing data read back were not the same as those written. Some errors may not be disastrous, but on the whole this is a fatal error. To track this down, run TESTIME_NEW in debug mode stepping through the assembler instructions, and see if the digital signals are reaching the timing RAM correctly.

It is probably worth running TESTWRT_NEW also, as this tests some of the same chips in the control and Data I/O cards used in the read/write timing data sequence, and in any case tests the VME side of the interface.

No END-OF-READOUT This means that the ONLINE has failed to see an END-OF-READOUT flag after some reasonable time. Check Pre-pulse is being sent to Eurocrate correcly. Run TESTRUN, and use an oscilloscope to see if the signals are as shown in the timing diagram, ending with an END-OF-READOUT. If the pre-pulse is correctly reaching the timing card, it is almost certainly a timing card problem.

Data Faults

No Clusters Found in Part of Plane/One Whole Plane If only one plane is affected the following could be the cause

- High Voltage Failure
- Mothercard Low Voltage Failure
- Mothercard Circuit Failure

If it is the last of these, then nothing can be done until OPAL opens. By sending a test pulse in time with the gate, one can whether the mothercard works. The only way to test High/Low Voltage is to measure the voltage at the supply crates, and follow it to the detector until we can no longer access the cables.

No Clusters found in Three Planes of a Quadrant In this case the suspicion falls heavily on the ADC card. Check that the jumper cables from the ADC card to the M/C driver card are all in place (there are lots of meddling fingers about !). Otherwise, use the test voltage facility and TESTGO to check the ADC card is working correctly.

No Clusters Found in detector from $0< \phi <180$ or $180< \phi <360$ Suggests that the control signals for this section are not reaching mothercards (though

simultaneous failure of two ADC cards cannot be ruled out - it has happened before). Check control signals at output of M/C driver card, and if these OK, then follow signals down to detector.

No Clusters Found in detector from 90< ϕ <270 or 270< ϕ <90 Suggest Low Voltage to detector pre-amplifiers has failed. This is supplied through the Calorimeter Low Voltage. Go and see Dick Kellogg!

No Clusters Found At All At One End This suggest that there is a fault in one of the "core" boards - i.e. Control/Data I/O, Timing Card, Memory Card, Trigger Card. Run TESTGO and look at data in detail - is it pedestal data or total garbage (i.e all channels show a few hundred counts or counts vary wildly over whole range). Pedestal suggests the failure of one or more of the timing signals to the mothercards. Complete garbage suggests failure of one of the digital control signals. Run TESTWRT_NEW and check that the interface to the data RAM is OK. If not, then run TESTWRT_NEW in debug mode, and check each instruction has the desired effect If TESTWRT_NEW runs OK, then run TESTRUN, and look with an oscilloscope if the analogue data entering the ADC card is pedestal. If the analogue data is OK check to see that the SAMPLE/HOLD and START A/D signals are reaching the ADC card and Memory Card, and that the sequence of signals on the memory card is correct.

No Clusters At Either End The only link between the ends is that they share a single High Voltage Crate. HT problems SHOULD be picked up by the FD HT monitor, which has so far proved reliable, but the HT must be manually checked if no clusters are seen. Again check data to see if it is garbage or pedestal

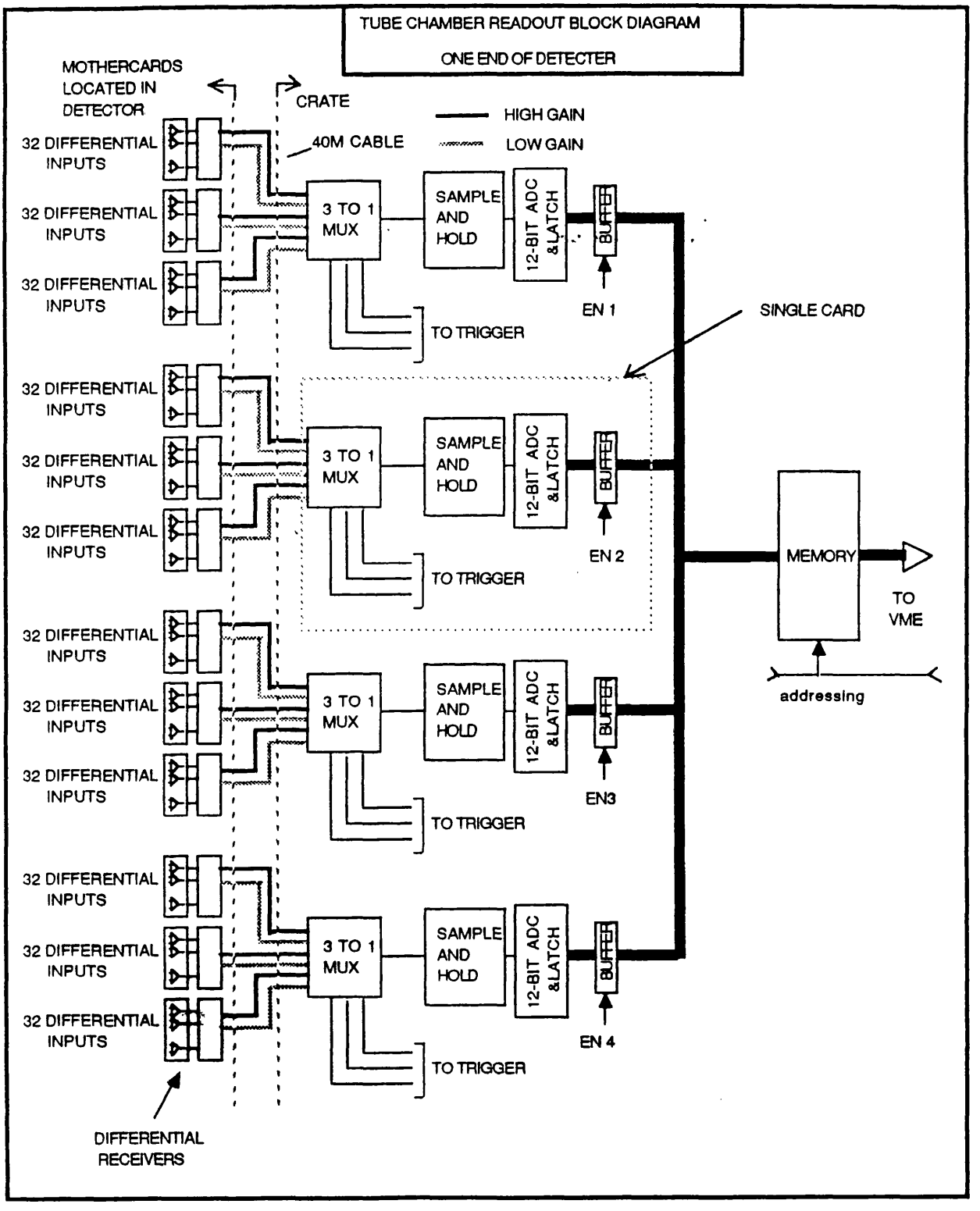

Figure A.1: Schematic Diagram of Tube Chamber Readout showing layers of multiplexing

BACKPLANE CONNECTIONS

a			b		c		
1	0V		1	0V (ANALOGUE)	1	0V	
2	5 V		2	5 V	2	5V	
3	D0		3	READY	3	CD0	
4	D1	ADC DATA	4	DIRECTION	4	CD1	
5	D2	BUS, TO AND	5	CONTROL WE	5	CD2	
6	D3	FROM	6	TRIGGER	6	CD3	CONTROL
7	D4	MEMORY	7	CONTROL DATA EN	7	CD4	DATA
8	D5		8	ENABLE DIRECT CONTROL CARD	8	CD5	
9	D6		9	ENABLE TIMING CARD	9	CD6	
10	D7		10	LEP RESET	10	CD7	
11	D8		11	EN 1	11	CMA0	
12	D9		12	EN 2	12	CMA1	
13	D10		13	EN 3	13	CMA3	CONTROL MEMORY
14	D11		14	EN 4	14	CMA4	ADDRESS
15	CN 0		15	PRE-PULSE	15	CMA5	
16	CN 1	CARD NO.	16	SWA	16	EOC 1	
17	CN2		17	SWB	17	EOC 2	
18	ADCA0		18	SWC	18	EOC 3	
19	ADCA1	EXTERNAL	19	SWD	19	EOC 4	
20	ADCA2	ADC MEMORY	20		20	ic 6 pin 9, end prim int.	
21	ADCA3	CONTROL	21	DATA	21	CS0	CHANNEL
22	ADCA4		22	EXT MEMORY ADDRESS	22	CS1	SELECT
23	ADCA5		23	START A/D	23	HIGH/LOW GAIN	
24	ADCA6		24	END OF CONVERSION	24	10 MHZ	
25	ADCA7		25	SOFTWARE TRIG IN	25	SAMPLE/HOLD	
26	ADCA8		26	END OF READOUT	26	TRIGGER RECEIVED	
27	ADCA9		27	MEMORY RESET	27	C0	CONTROL BUS
28	7V		28	RESET	28	C1	CONTROL
29	TEST V		29	0V	29	C2	CODE
30	-12V		30	-12V	30	ADDRESS STROBE	
31	12V		31	12V	31	12V	
32	0V		32	0V (DIGITAL)	32	0V	

Figure A.2: Listing of backplane assignment of control lines

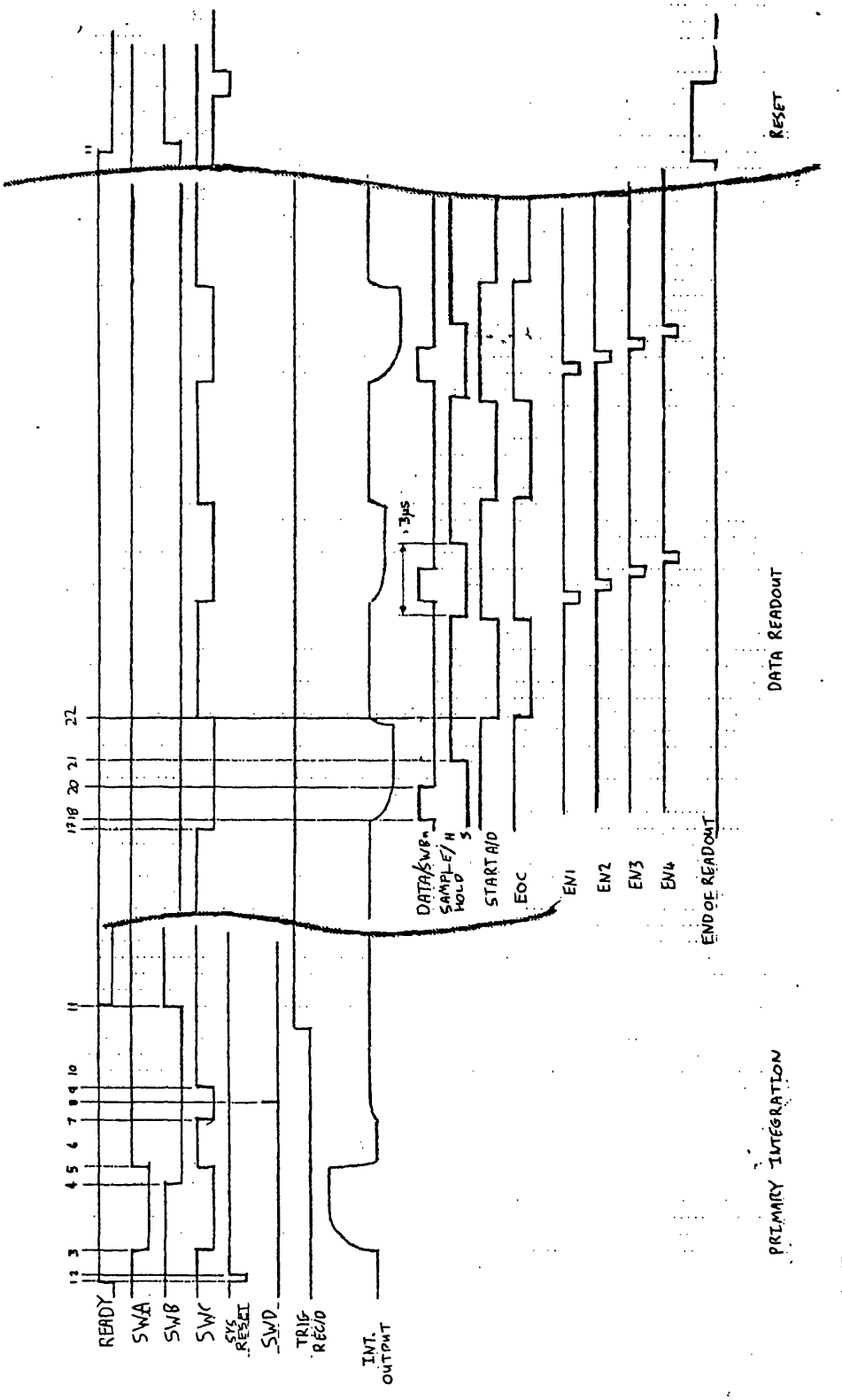

Figure A.3: Timing diagram for principle control signals

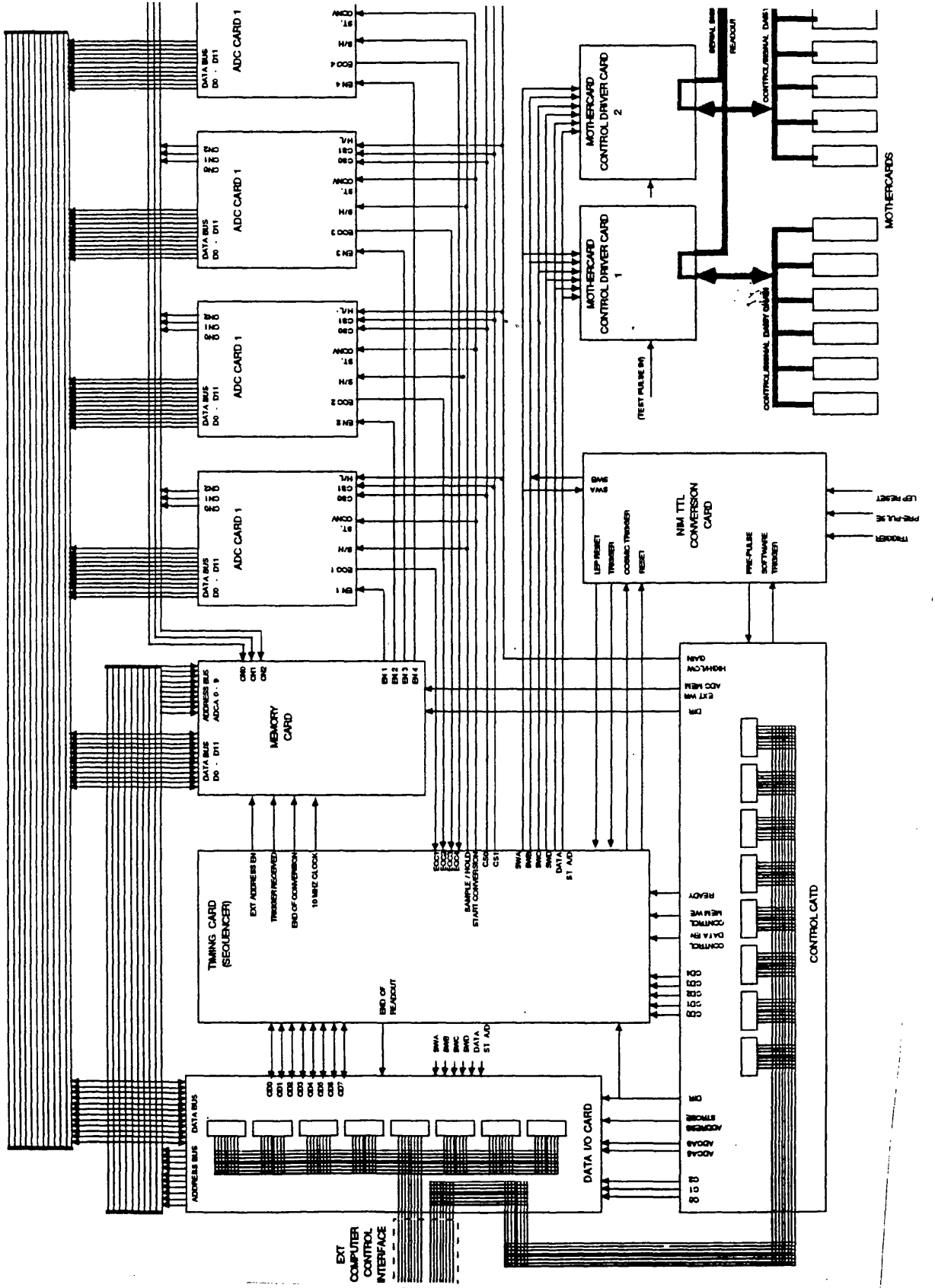

Figure A.4: Diagram showing routing of principal control signals to different circuit boards

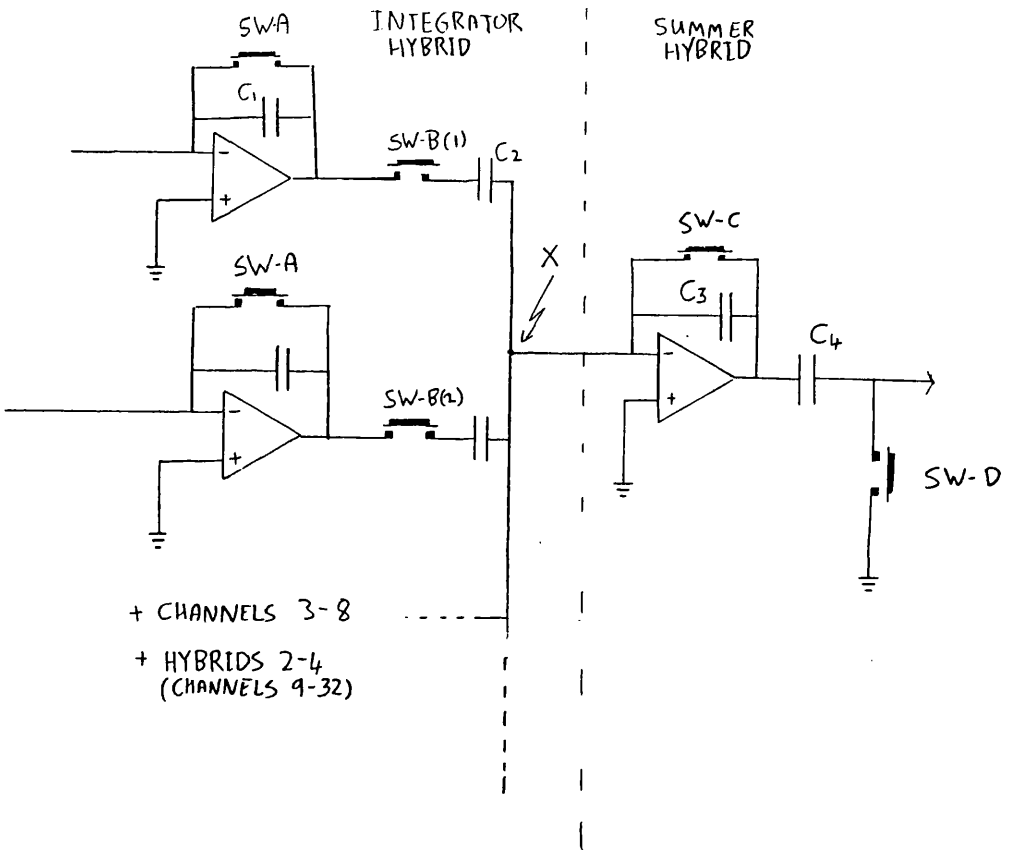

Figure A.5: Schematic diagram of integrator/summer operation

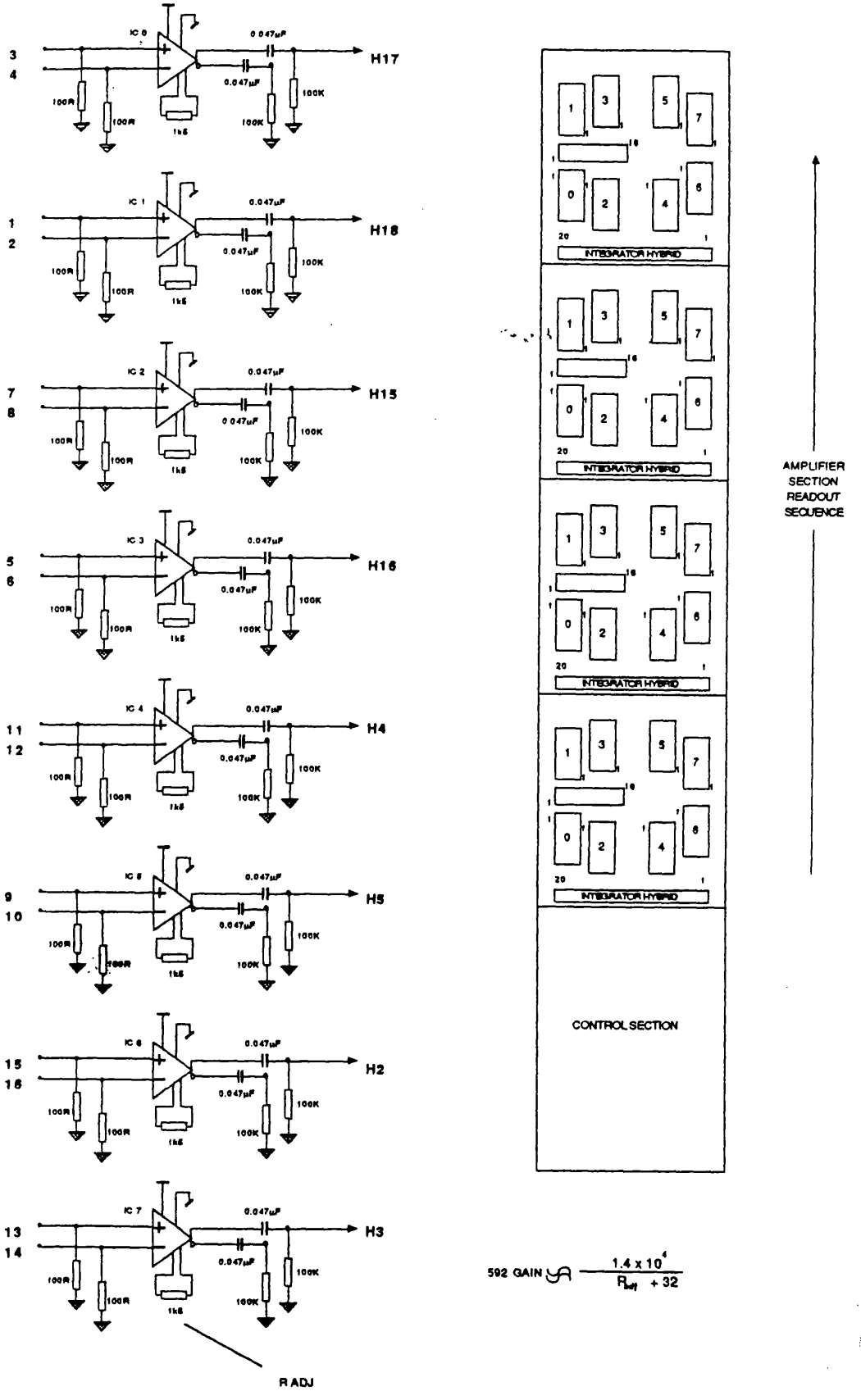

Figure A.6: Circuit diagram and layout of mothercard receivers

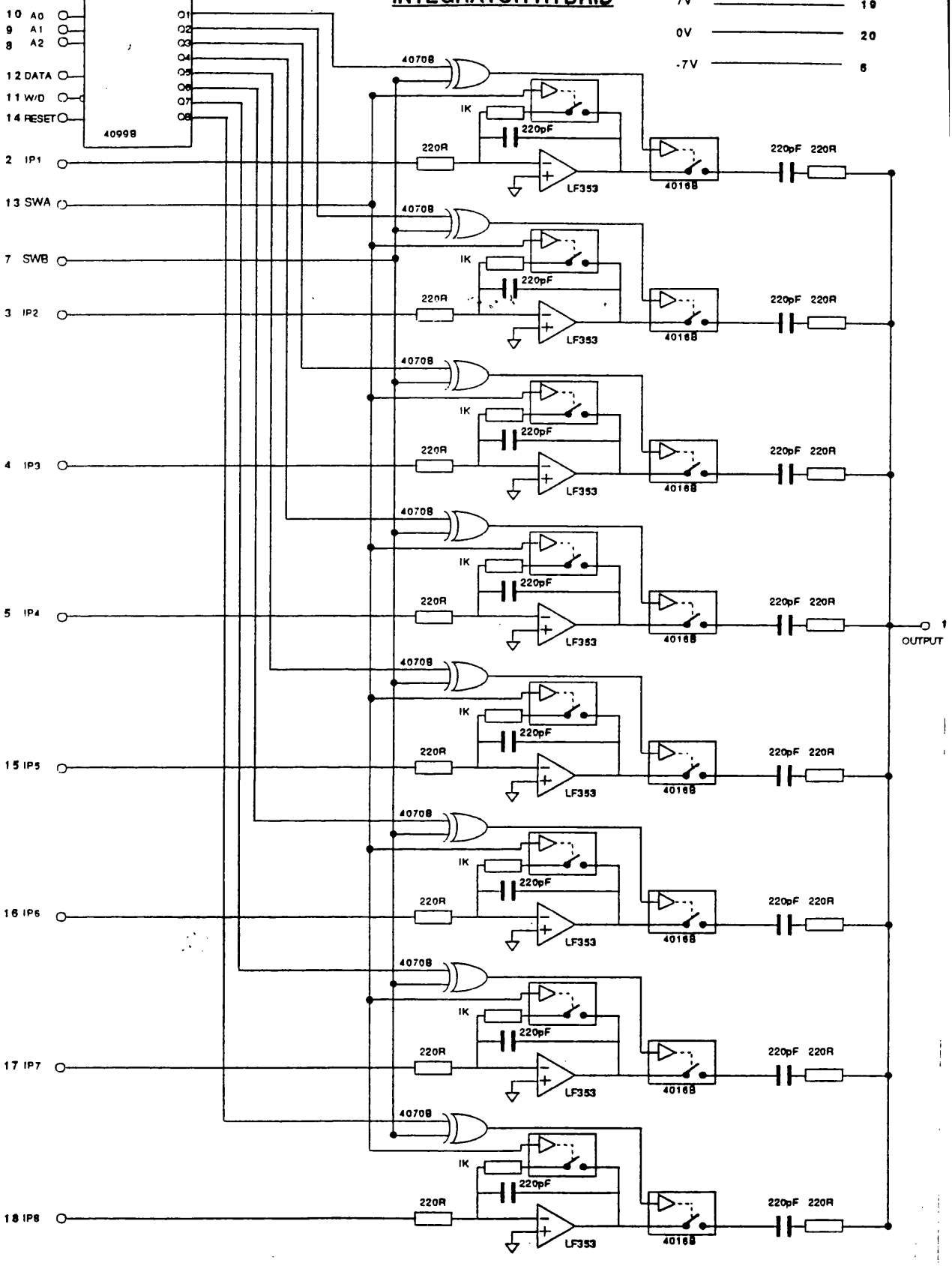

Figure A.7: Circuit diagram of integrator hybrid

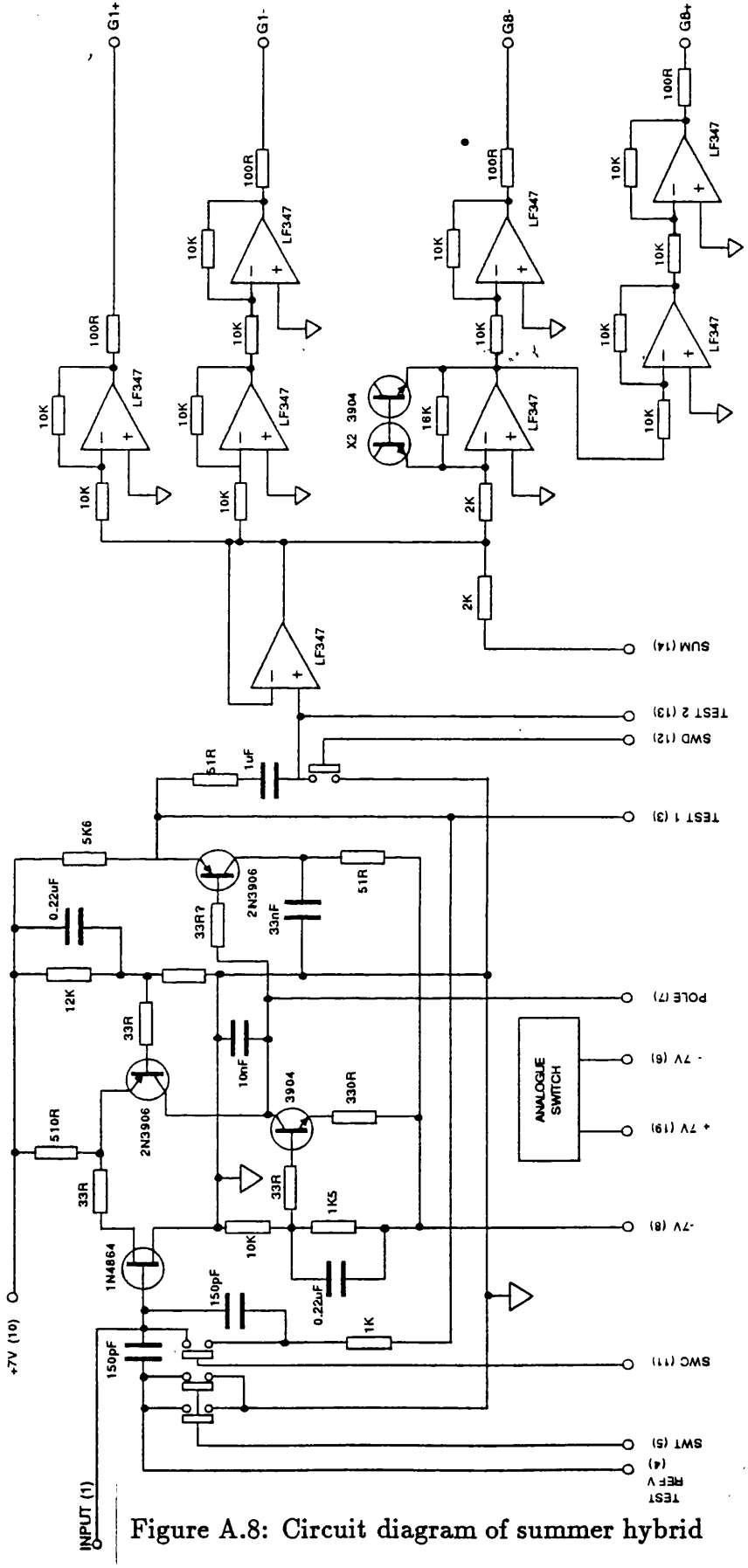

Figure A.8: Circuit diagram of summer hybrid

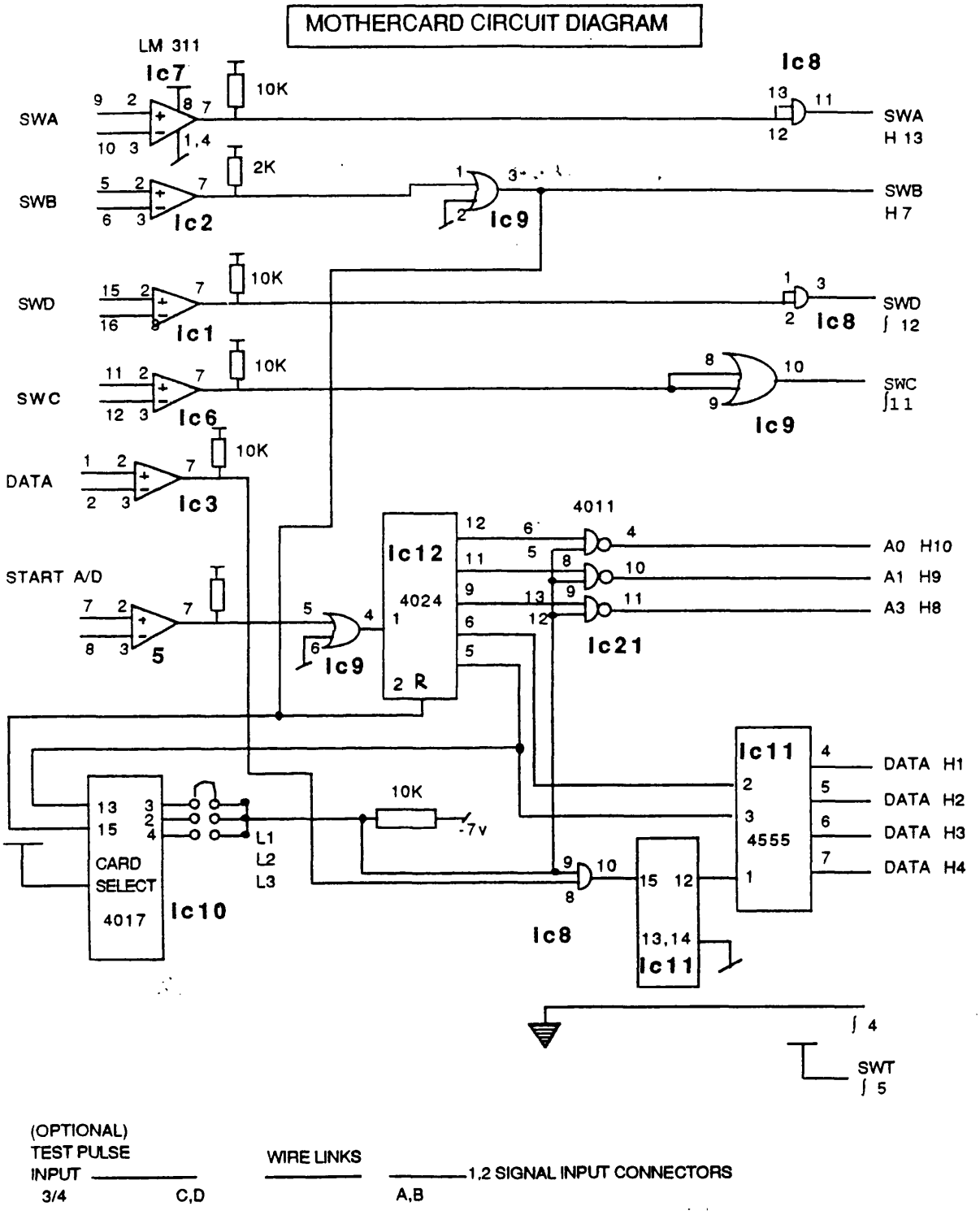

Figure A.9: Circuit diagram of mothercard control logic

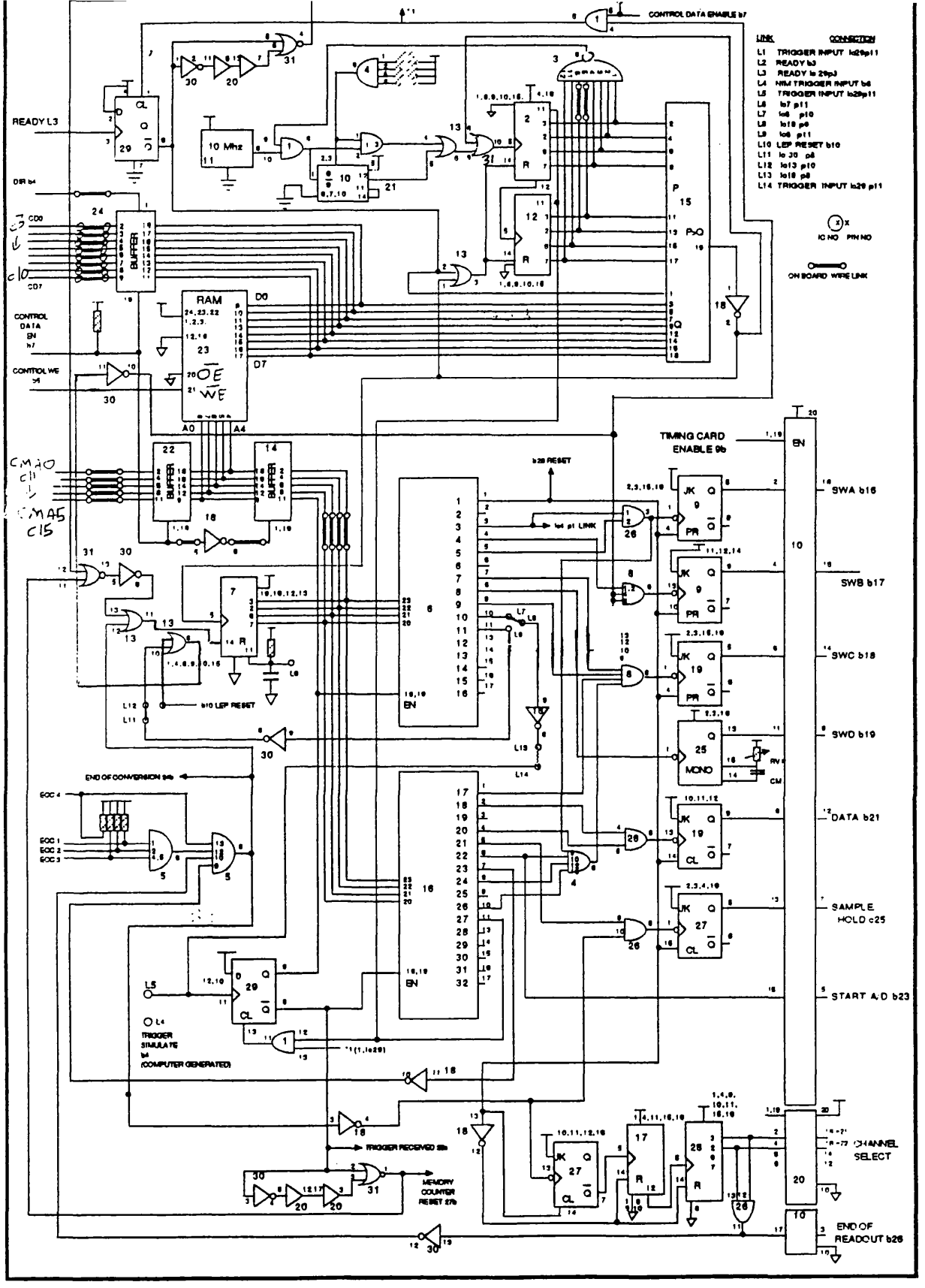

Figure A.10: Circuit diagram of timing card

Timing Card Component Layout

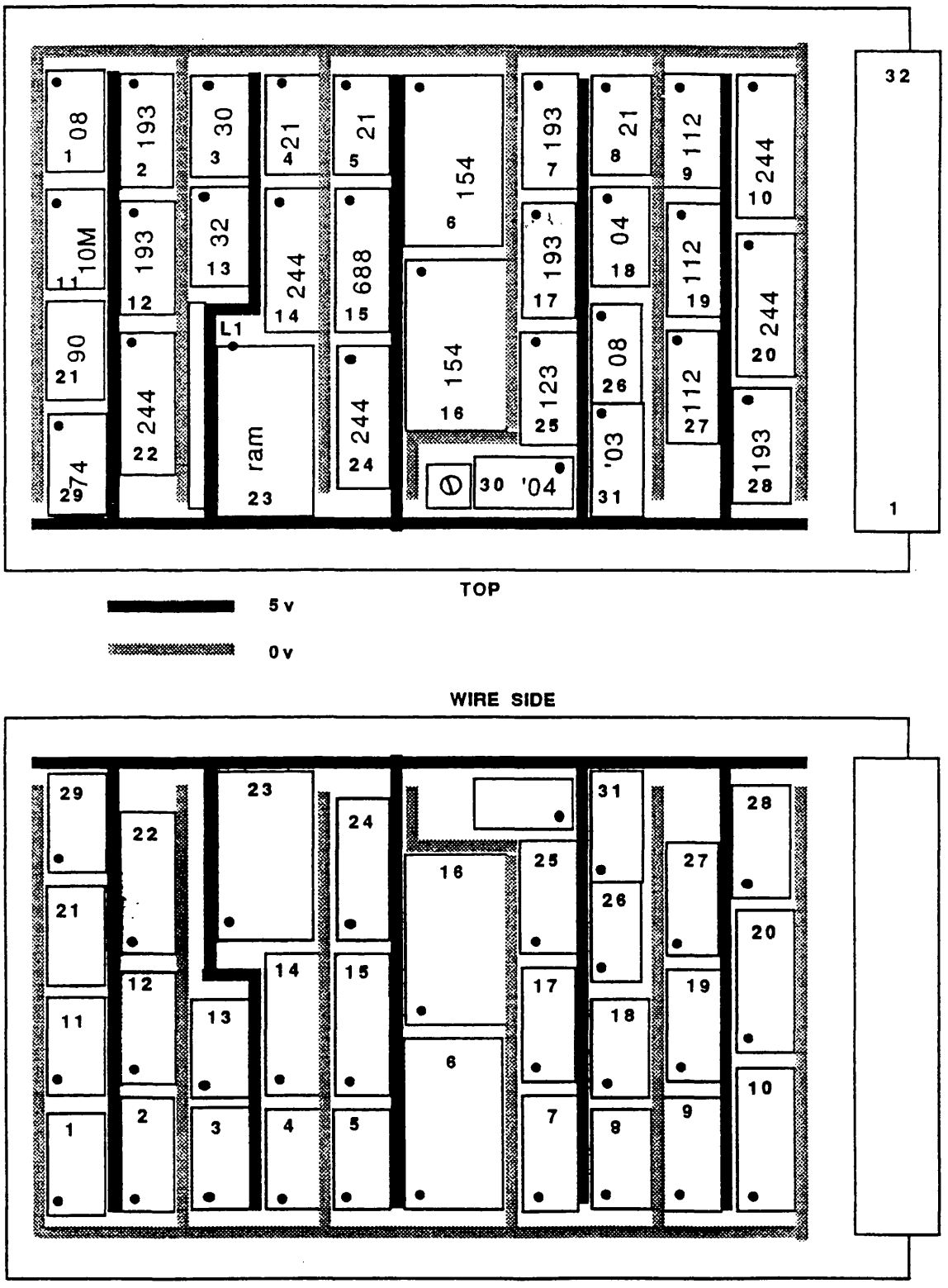

Figure A.11: Diagram of timing card layout, showing IC type

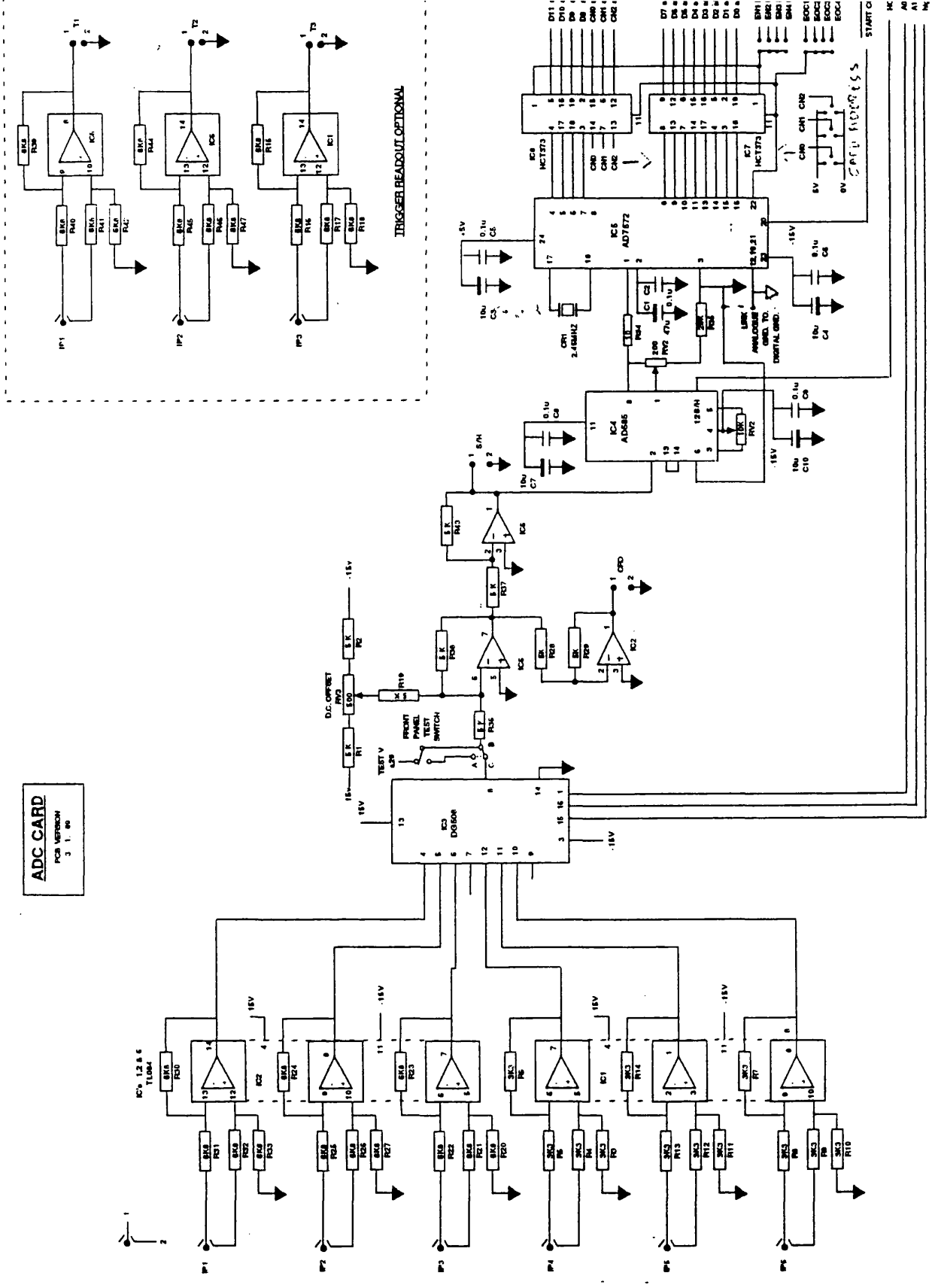

Figure A.12: Circuit diagram of ADC card

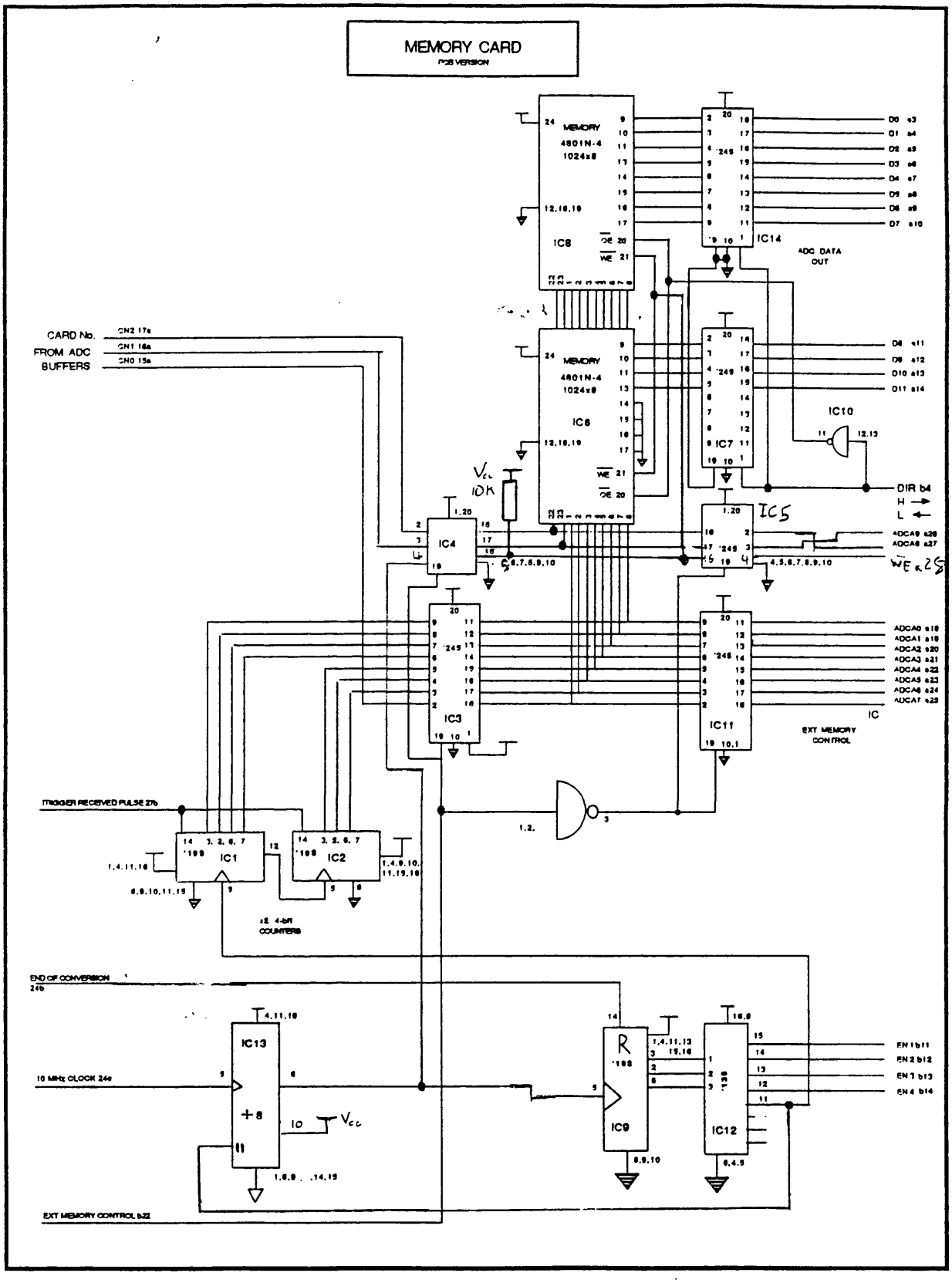

Figure A.13: Circuit diagram of memory card

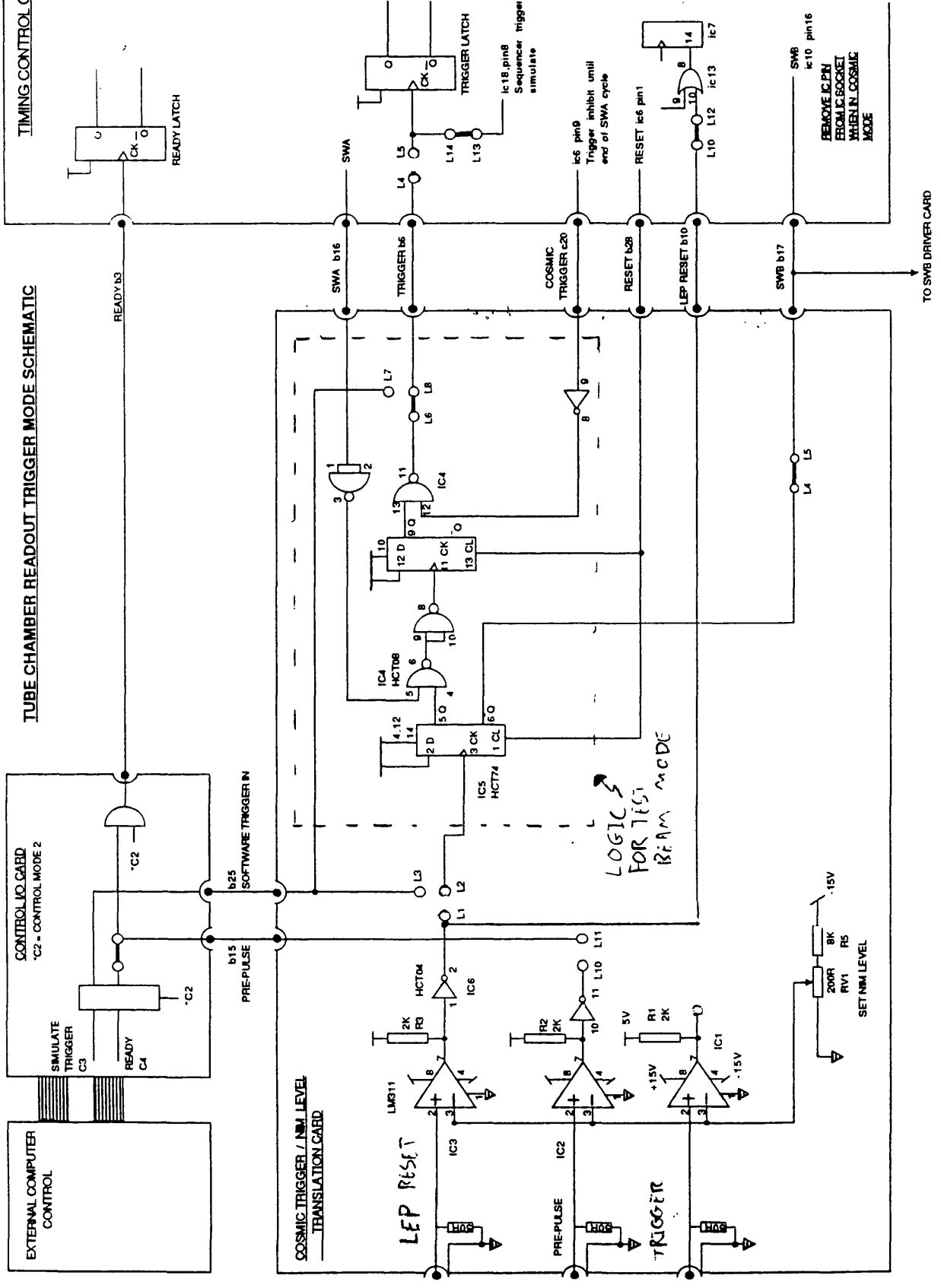

Figure A.14: Circuit diagram of trigger card

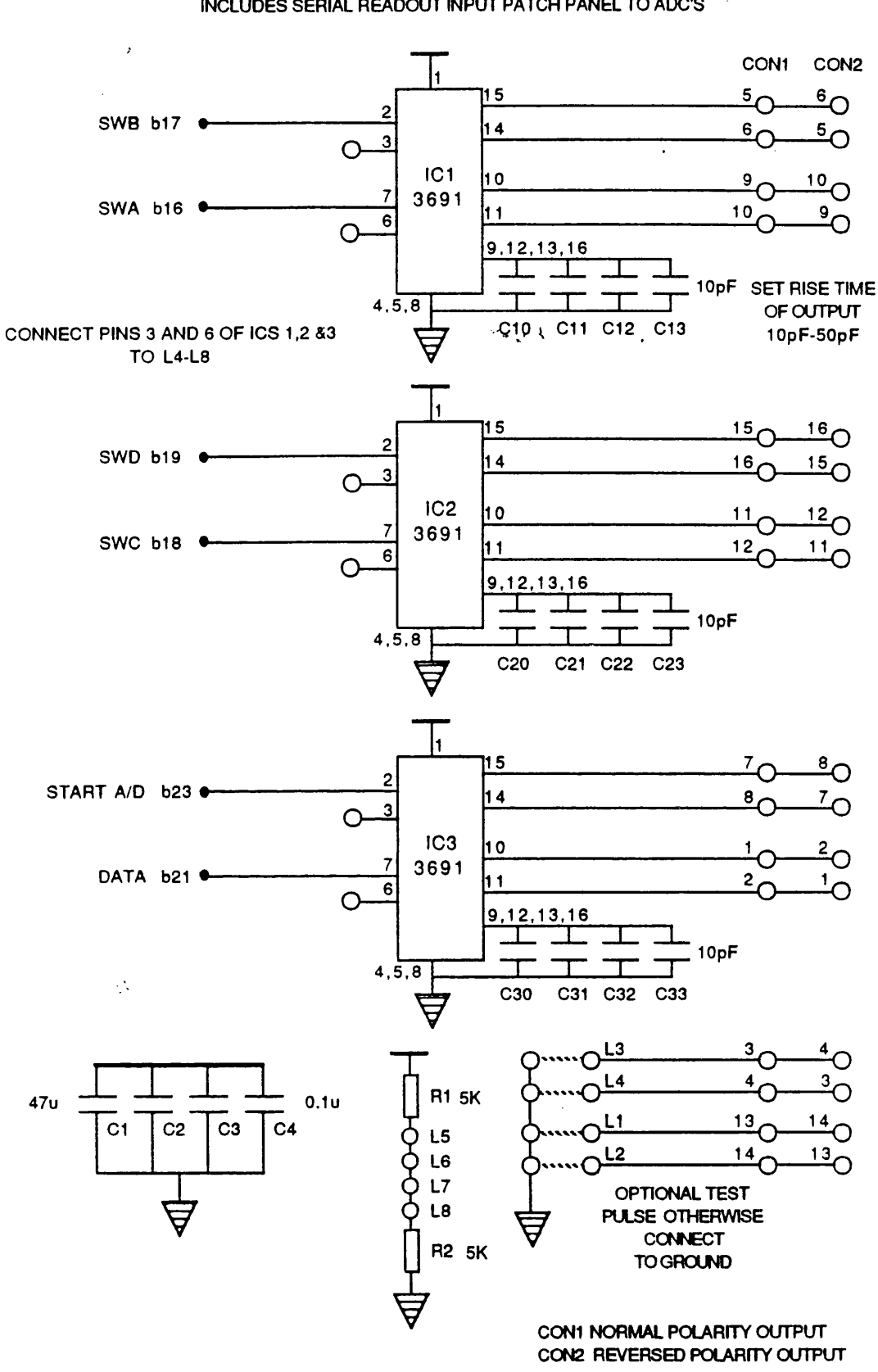

Figure A.15: Circuit diagram of mothercard driver card

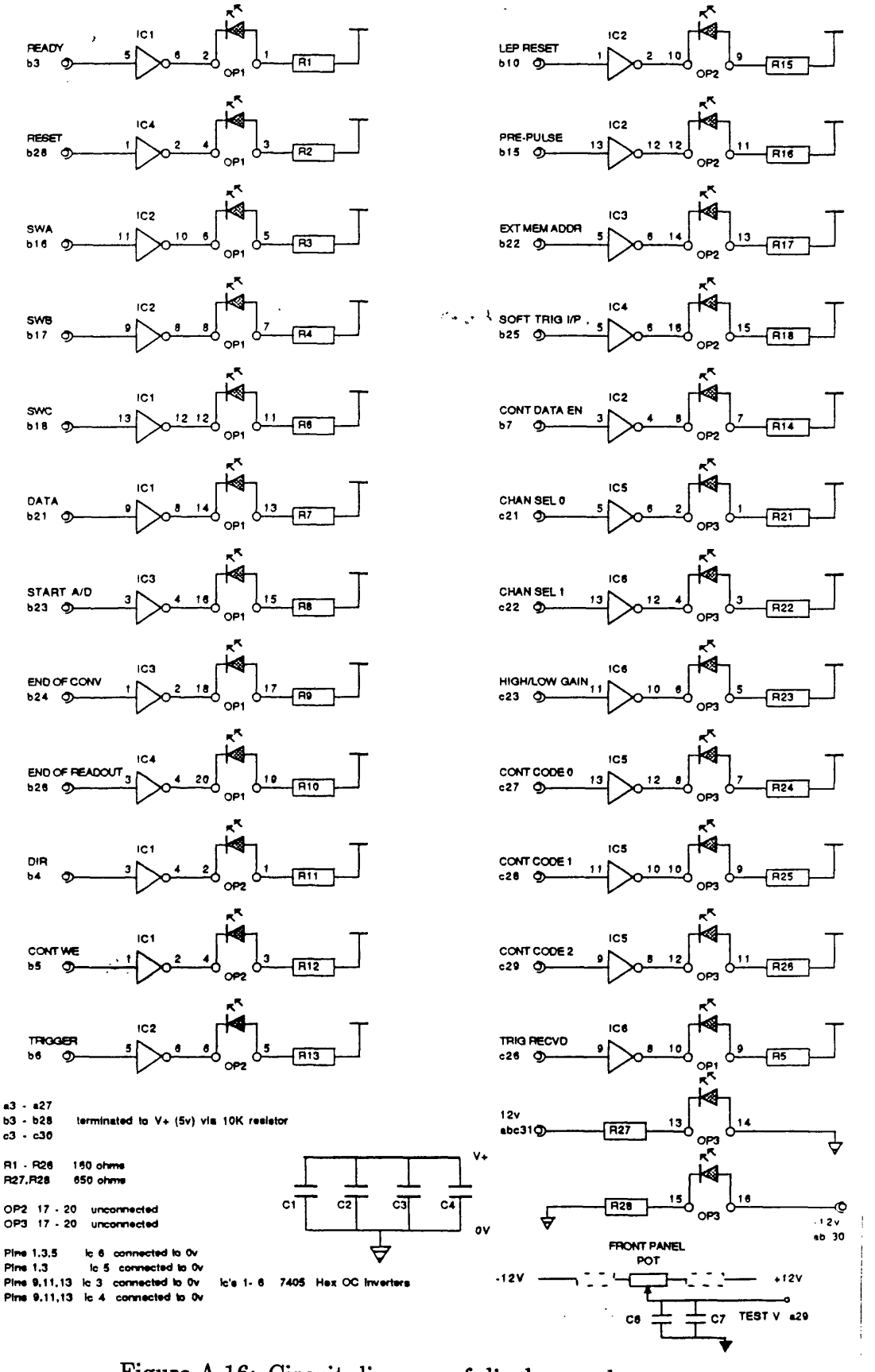

Figure A.16: Circuit diagram of display card

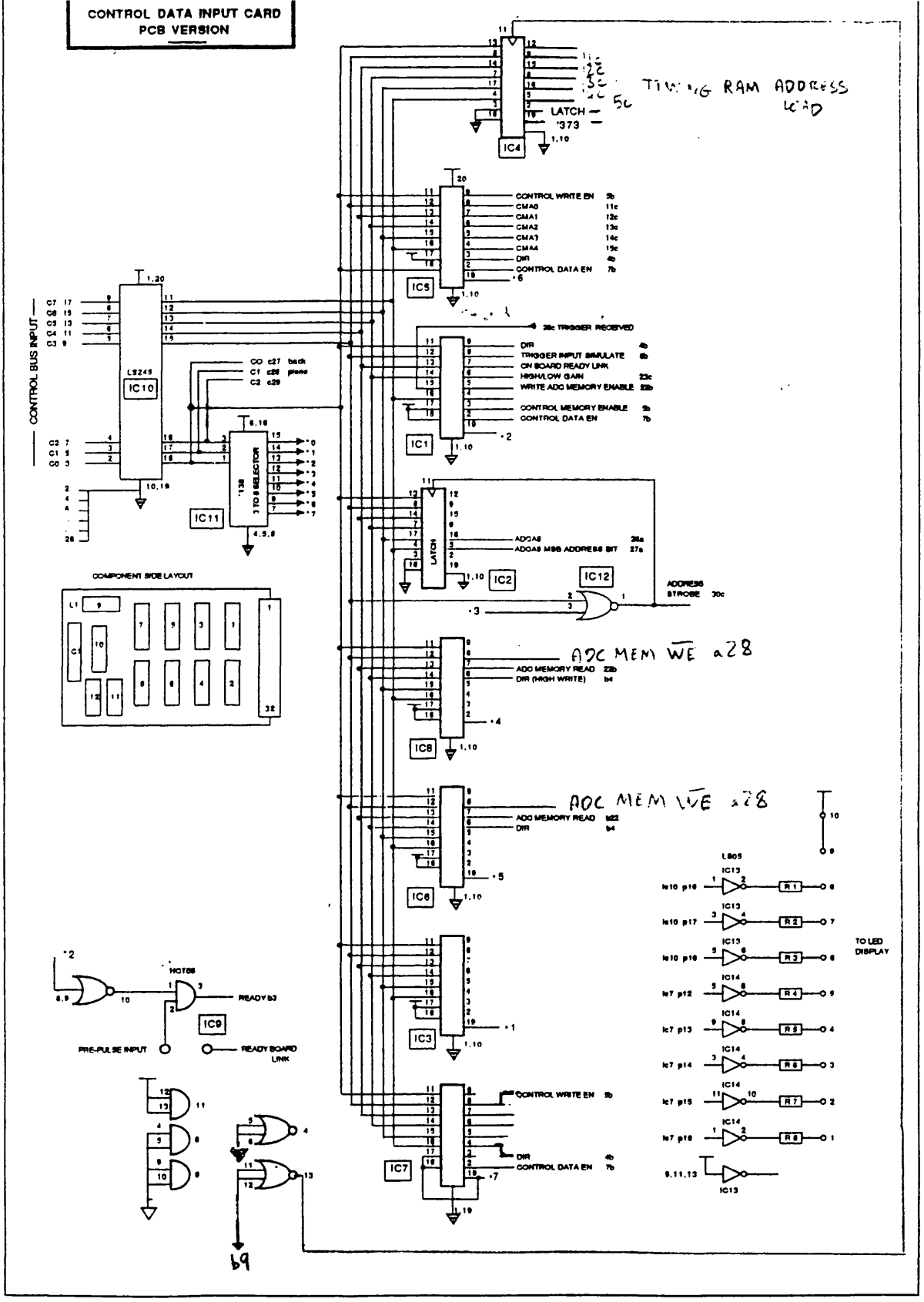

Figure A.17: Circuit diagram of control I/O card

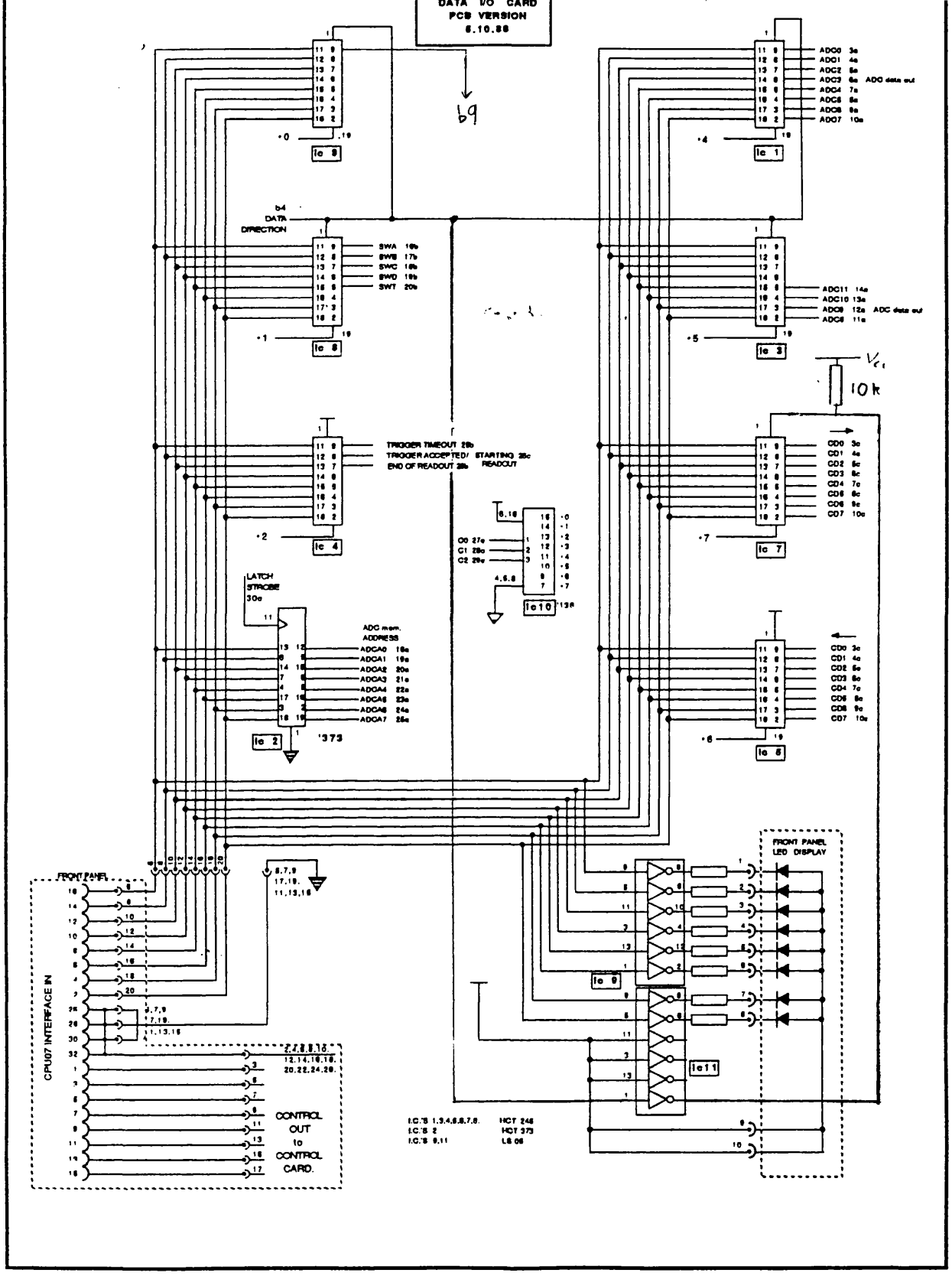

Figure A.18: Circuit diagram of Data I/O card

Appendix B

Compact Drift Chambers for the OPAL Forward Detectors

This appendix is a copy of a paper submitted to the Vienna Wire-chamber conference of 1989 (and subsequently published in N.I.M. A238 (1989)) by the following authors:-

B.E.Anderson, D.J.Attree, A.Charalambous, R.Cranfield
M.Cresswell, G.Crone, G.M.Dallavalle, M.Dryburgh
B.W.Kennedy, D.Hayes, L.Marradi, D.J.Miller,
P.Sherwood, E.Spreadbury, N.C.Wood, K.K.Young.

B.1 Introduction.

The OPAL Forward Detectors (fig. B.1) will measure luminosity by detecting Bhabha scattering at between 47 and 120 milliradians from the circulating beam direction. They will also tag electrons from gamma-gamma events. The two planes of drift chambers at each end are 200 mm apart. Requirements on the drift-chamber design include:

i) good angular coverage of the "clean" acceptance of the Forward Detector

ii) no losses due to Lorentz angle in the OPAL magnetic field

iii) good radial resolution, reasonable azimuthal resolution and good multi-track separation

iv) for the front plane of chambers, low density to reduce the showering of electrons and gammas.

B.2 Construction.

The chambers are lozenge-shaped, with two gas-gaps 11 mm deep, each gap having two sense wires and a field wire stretched across its 400 mm. longest diagonal. The faces of the rear chambers, and of those tested, are printed circuit boards 1.6 mm thick, with a pattern of copper strips and cathode pads on both surfaces of the board. (Foam-faced chambers have been made for the front plane on OPAL.) Over most of the area the uniform drift field is maintained by strips 0.4 mm wide at a pitch of 1.8 mm (fig. B.2). Machined GRP (glass-reinforced epoxy) frames form the outer walls of both gaps, with copper strips or foils stuck on the inside and connected to the strips on the faces. The stagger of 2 mm between wires in adjacent gaps is sufficient to resolve the ambiguity between tracks above the sense wires (further from beampipe) or below the sense wires.

	Field wires	Sense wires
Number per chamber	2	4
Number per gas gap	1	2
Material	Cu-Be	Nichrome
Diameter	120 μm	25 μm
Located to	50 μm	20 μm
Tension	150 grammes wt.	35 grammes wt.

Each gap is electrically separate from the other gap in the same chamber. Drift-fields are defined by chains of 4.7 MΩ 1/4-Watt resistors, mounted obliquely between successive strips in the gap between the faces just outside the frame (fig. B.2), with wire links connecting corresponding strips on opposite sides of the gap. Each chain is potted in epoxy resin. The chain on the long (inner) side

of a gap has a total resistance of 360 MΩ for 130 mm drift distance. The short (outer) side has 220 MΩ for 83 mm drift. Field and sense wires are 400 mm long.

During final wrapping the flat faces are covered with an insulating layer of clear kapton sheet, stuck with epoxy resin. Layers of specially prepared polypropylene film [38] are heat-shrunk over the outer and inner curved edges, overlapping the kapton by some tens of millimetres. A second layer of clear kapton is stuck over the flat face, with an external ground-layer of copper-coated kapton over the whole outer surface. Close to the beam pipe the -12 kV electrode on the inner GRP wall of the drift-space comes within 1.5 mm of the outer ground-layer.

The copper strips on both surfaces of each face are at the same electrical potential. This ensures that sharp discontinuities in the field are concentrated in the insulating layers outside the faces, under the copper ground-layer. Further field-smoothing is achieved by coating the inner face of each board with a thin layer of "Breox" (polyalkalene glycol) which has a finite conductivity in chamber conditions. Its leakage current is small enough not to cause distortion of the drift field.

Both ends of a sense wire are read out separately to give coarse position measurement by current division. More precise information comes from the induced pulses on sets of cathode pads on the inside faces of the chamber boards, close to the sense wires. The pads have an intersecting diamond pattern with a repeat distance of 40 mm (fig. B.3), each set displaced by 10 mm from the set on the next face. The two outer pads of each set are connected together to the return side of a differential preamplifier and the inner pad is connected to the signal side. Pulses from cathode pads may be either positive or negative going, depending to the position of the hit.

The wire and pad preamplifiers both use LM733 differential amplifiers, with appropriate shaping and gain networks. Signals are digitised by DL300 Flash-ADC modules [39] running at 50 MHz, each with a 256-word 6-bit memory. Events are written to tape by the OPAL VME/microVAX data-acquisition system. FADC modules for the wire signals have the standard nonlinear response,

corrected offline using the manufacturer's nominal parameters (will be calibrated in OPAL). Pad readout modules are converted to linear response, with the pedestal in the middle of the dynamic range to accept bipolar signals.

B.3 Test Beam Operation.

Two prototype drift-chambers were exposed to electrons in the X5 test beam at CERN in the summer of 1988. They were mounted as a front and a rear chamber on a calorimeter module, as they will be in OPAL. The prototypes differed marginally from the production models for the rear plane. The largest difference was a cathode pad diamond pattern 45 mm. wide, compared with 63 mm. in the final version. The gas was argon with 10% ethane, bubbled through isopropyl alcohol at 5 degrees C. The gas-gain was approximately 10^5.

By combining translations and rotations of the computer-controlled support stage it was possible to ensure that the beam through any part of the detector had the same direction as scattered particles from the LEP intersection point in OPAL. Trigger counters defined a spot 10 mm. square in a parallel beam and provided the start time for the FADCs. More precise information on the position of each beam particle was given by a 100 mm square multiwire beam-chamber with delay-line readout. A data-taking run consisted of a series of scan-points, each having between 200 and 1000 beam-triggers with the stage at a particular position.

B.4 Analysis and Results.

Pedestal values were determined by histogramming the FADC signals over several hundred events. A hit has at least two consecutive timeslots more than 10 counts above pedestal, with the previous bin below this threshold, and a sum over six timeslots of more than 40 counts above pedestal. The time of arrival is estimated from a weighted mean of the five timeslots nearest the peak. Other techniques such as "difference of samples" [40] are also being tested. For reconstruction studies clean events have been selected with at least 6 out of 8 possible wire hits

in a chamber, only one track and no delta rays.

The time resolution is ±7ns, calculated from the r.m.s. deviation between the ends of the same wire. From fits to four wire-hits in a chamber on clean tracks , the spatial resolution is found to be ±200 μm at short drift distances, rising to 400 μm at long drifts. Single-wire efficiencies are better than 98% for all drift distances.

A reference point within the beam spot was defined to ~2mm, using beam-chamber data. The mean drift times corresponding to this reference at a series of scan points are plotted in fig. B.4 against the stage position. The drift speed at 0.92 kV/cm was (37.8 ± 0.7) mm/μs, with linearity better than 0.5mm over the whole range. Charge-division gives the position of a track along a wire to ±5mm (with nonlinearity uncalibrated, as yet). This is sufficient to define the expected phase of the hit within the periodic repeat-pattern of the diamond pads. A pad signal is integrated within a 160 ns window around the hit time on the corresponding sense-wire, and normalised by dividing it by the sum of the signals from the two ends of the wire. Normalised pad signals from the opposite faces of a single gap are plotted on fig. B.5, where a large number of scan-points (stage positions) have been taken together. One cycle around the approximately square locus represents a movement of 40 mm along the wire. Algorithms are being developed to derive the best position for a hit. The resolution for clean hits is ~ ±1mm.

Acknowledgements

Our thanks to the University College London workshop; also to D.Plane, R.G.Kellogg, W.Miller, D.Naples and P.R.Hobson. The University of Chicago very generously lent their moveable stage.

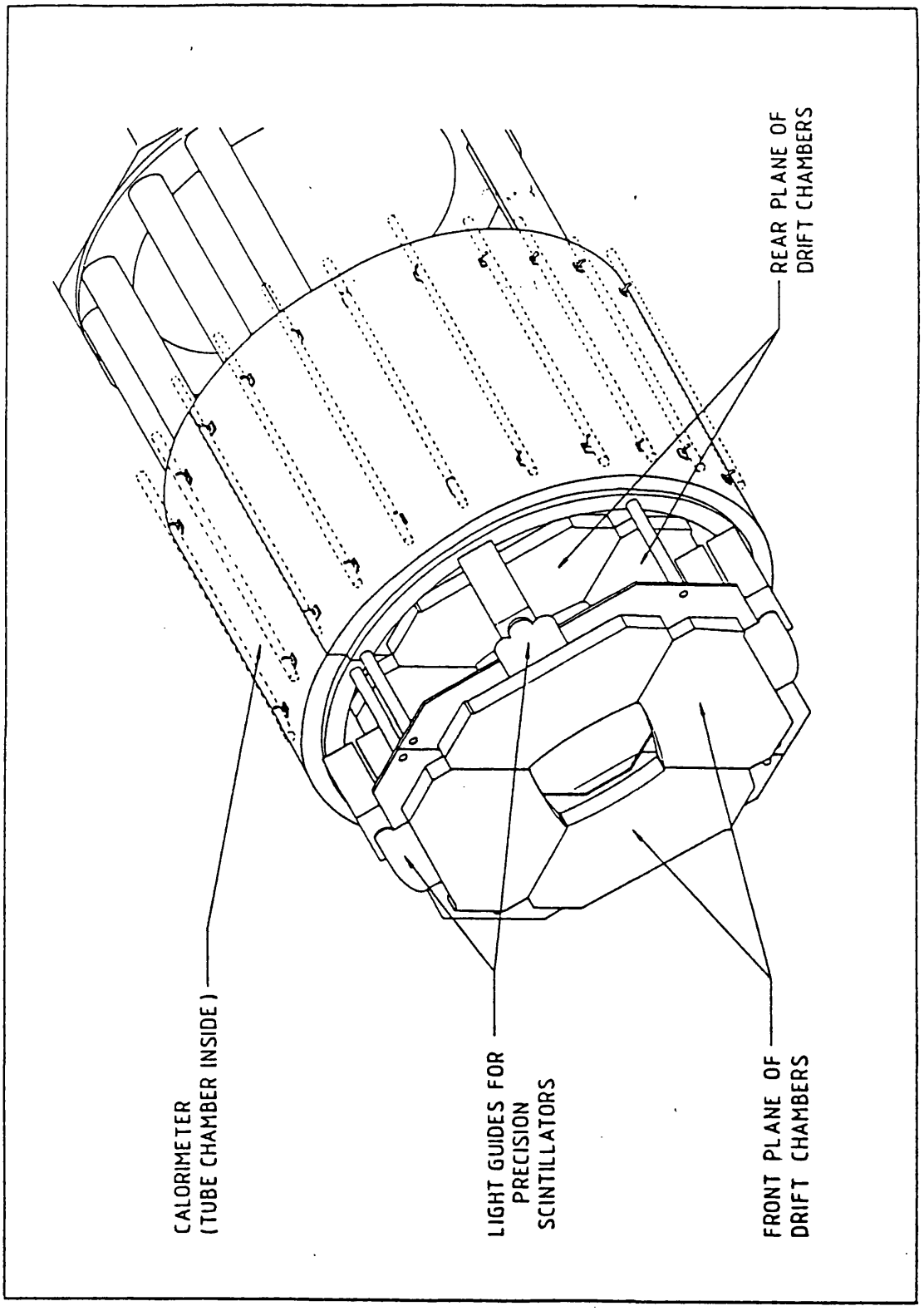

Figure B.1: The OPAL Forward Detector

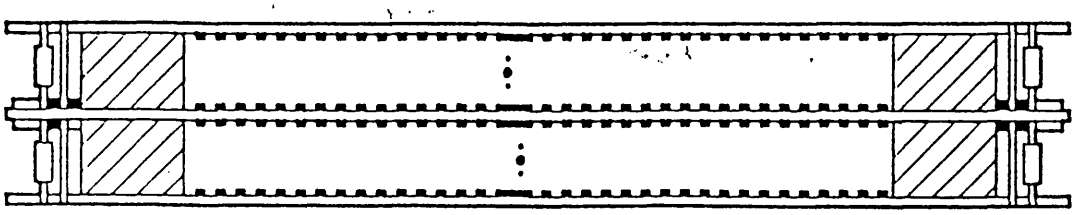

Figure B.2: Cross Section through a Drift Chamber, showing the two gas gaps, displaced sense and field wire, and field shaping strips

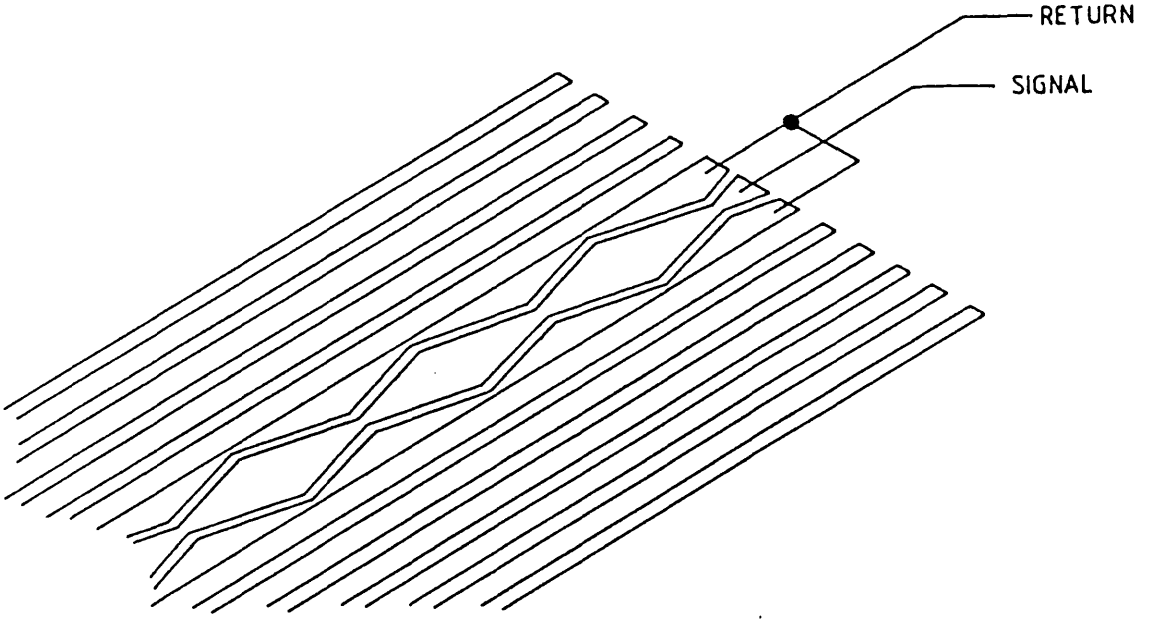

Figure B.3: Sketch of interlocking diamond pad pattern

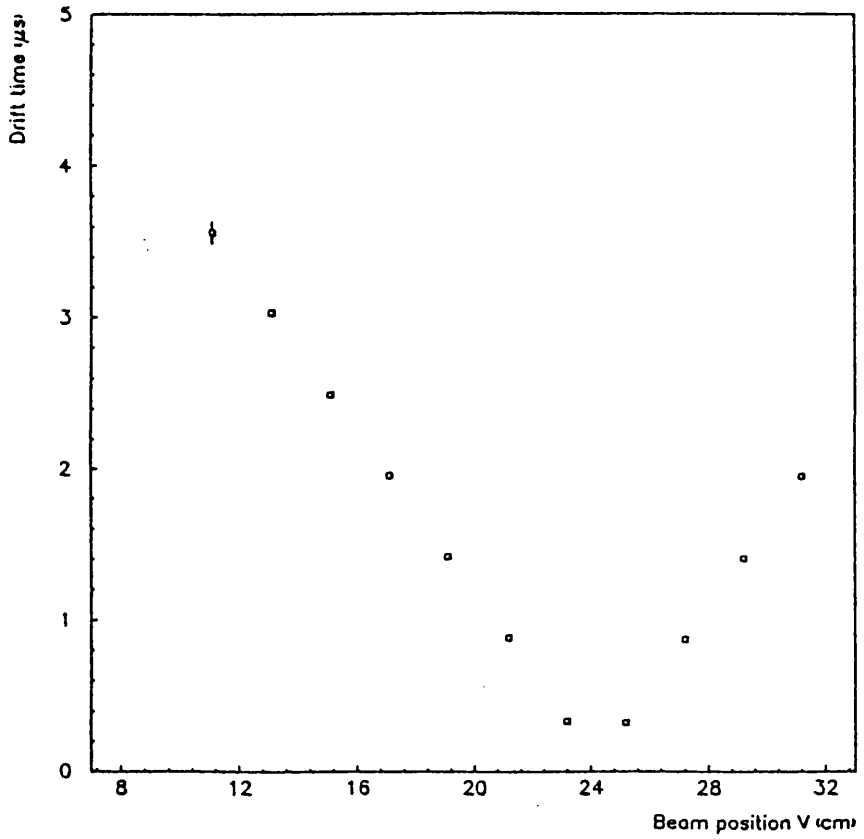

Figure B.4: Mean drift time vs. stage position

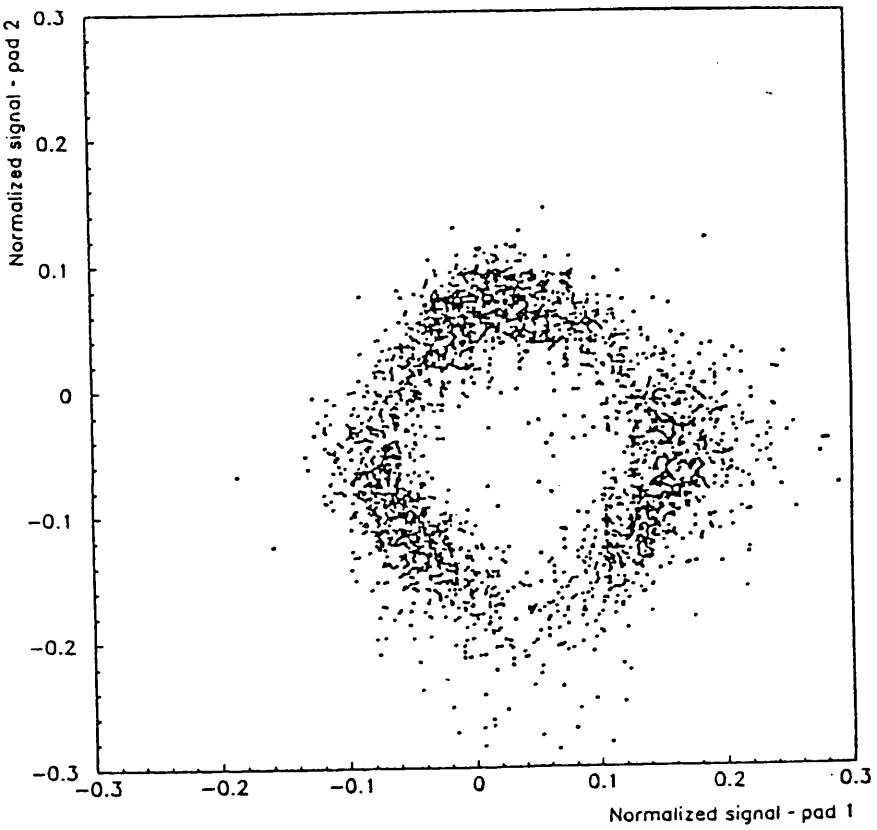

Figure B.5: Scatterplot of normalised pad signals from opposite faces of the same gas gap

Bibliography

[1] F.Halzen D.Martin 'Quarks and Leptons' John Wiley and Sons New York 1984.
D.Perkins 'Introduction to High Energy Physics' Addison-Wesley Reading,Massachusetts.

[2] A.D.Dolgov B.Zeldovich Rev. Mod. Phys. 53 (1981) 1.

[3] D.V.Schramm R.V.Wagoner Ann. Rev. Nucl. Sci.27 (1977) 37.

[4] G.Steigman,D.N.Scramm,J.E.Gunn Phys. Lett. B66 (1977) 202.
J Yang et. al. Ap. J. 227 (1979), 697.
K.A. Olive et. al. Ap. J. 246 (1981), 557.
J.Yang et. al. Ap. J. 281 (1984), 493.
J.Ellis et. al. Phys. Lett. 176B (1986), 457.
G.Steigman et. al. Phys. Lett. 176B (1986), 33.

[5] R.M.Bionta et. al. Phys. Rev. Lett. 58(1987),1494.

[6] K.Hirata et. al. Phys. Rev. Lett. 58(1987),1490.

[7] J.Ellis K.Olive CERN.TH.4701/87

[8] Cello Colaboration Phys. Lett. B176 (1986) 247.

[9] G.Bartha et al Phys. Rev Lett. 56 No.7 (1986) 685.

[10] C.Hearty et al Phys. Rev Lett. 56 No.17 (1986) 1711.

[11] Th. Muller CERN-EP/88-175, Invited Talk 7th Topical Workshop on $p\bar{p}$ Collider Physics,Fermilab

[12] C.Albajar et. al. (UA1 Collab.) Phys. Lett. 198B,(1987) 271.

[13] R.Ansari et. al. (UA2 Collab.) Phys. Lett. 186B,(1987) 440.

[14] CERN yellow report 89-08 Vol. 1.

[15] G. Altarelli G.Martellini CERN yellow report 86-02 (1886) 47.

[16] F.A.Behrends et. al. Nucl. Phys. B297 (1988) 429, Nucl. Phys. B304 (1988)

[17] Behrends et al CERN-TH.4865/87 Radiative Corrections to the process e+e- $\rightarrow \nu\bar{\nu}\gamma$

[18] D.Karlen Nuc. Phys. B 289 (1987) 23

[19] Martinez and Miquel Univ. of Barcelona preprint UAB-LFAE 87-01 Radiative corrections to e+e- $\rightarrow$ e+e-γ (submitted to Nuc. Phys. B)

[20] F.A. Behrends, R. Kleiss and W. Hollik, Nucl. Phys. B304 (1987) p712.

[21] K.Ahmet et. al. OPAL Collaboration. The OPAL detector (to be submitted to N.I.M.)
OPAL collaboration CERN/LEPC/83-4 OPAL technical proposal.

[22] R.L.Chase I.F.Corbett IEEE Trans. Nucl. Sci. NS-32 No.1 (1985) 645.

[23] D.C.Imrie, et al N.I.M. A283 (1989) 515.

[24] M.Z.Akrawy et al, Phys. Lett. B231 (1989) 530.

[25] M.Z.Akrawy et al, Phys. Lett. B235 (1990) 379.

[26] F.A.Berends,R.Kleiss,W.Hollik, Nucl. Phys. B304 (1989) 712.

[27] S.Jadach et. al. Z. Physics at LEP1, CERN 89-08 Vol 1 (1989); KORALZ, version 37.

[28] J.Allison et. al. Comp. Phys. Comm. 47 (1987)55;

[29] R.Brun et. al. GEANT3, Report DD/EE/84-1 CERN (1989)

[30] T.Sjostrand Comp. Phys. Comm. 39(1986) 347; JETSET, Version 7.1

[31] OPAL Collaboration Phys. Lett. B236 (1990) 364.
OPAL Collaboration CERN/EP 90-48 (1990) Submitted to Z. fur Physik C

[32] G.Marchesini B.R.Webber Nucl. Phys. B310 (1988) 461; HERWIG Version 3.2

[33] R.Barlow Statistics - A Guide to the Use of Statistical Methods in the Physical Sciences Manchester Physics Series John Wiley and Sons

[34] CERN Program Library Long Write Up D506 (1989)

[35] G.Burgers Nucl. Phys. B297 (1988) 429.

[36] D.Decamp et. al. ALEPH Collaboration Phys. Lett. B235(1990) 399.
P. Arnio et. al. DELPHI Collaboration CERN EP/90-19 submitted to Phys. Lett.
B.Adeva et. al. L3 Collaboration Phys. Lett. B237(1990) 136.

[37] M.Z.Akrawy et. al. OPAL Collaboration Phys. Lett. B240 (1990) 497.

[38] Made by Solarfilm, Chorley, Lancashire, England.

[39] Manufactured by Dr B Struck to University of Heidelberg design.

[40] D Schaile, O Schaile, and J Schwarz, Nucl Instr Meth A242, 247-253, (1986).